DISSERTATION

MOLECULAR DESIGN OF A FATIGUE-RESISTANT AND ENERGY-DISSIPATIVE HYDROGEL

Submitted by

Allee Shiryce Klug

Department of Chemistry

In partial fulfillment of the requirements

For the Degree of Doctor of Philosophy

Colorado State University

Fort Collins, Colorado

Summer 2022

Doctoral Committee:

Advisor: Travis Bailey

Melissa Reynolds
Eugene Chen
Chris Weinberger

ABSTRACT

MOLECULAR DESIGN OF A FATIGUE-RESISTANT AND ENERGY-DISSIPATIVE HYDROGEL

Hydrogels at the most basic iteration are cross-linked polymer networks swollen in water. They show promise in biomedical applications due to their high water content and flexibility. However, intentional design of new hydrogel networks by modification of the choice of polymer, the fabrication of the polymer network, and the choice of cross-link have resulted in hydrogels which have useful properties ranging from fatigue resistance to elasticity to bulk toughness. Of particular interest is a hydrogel which can dissipate energy as a way to resist failure of the polymer network. Unfortunately, many of the design strategies previously used to insert an mechanism for energy dissipation into the hydrogel result in hydrogels which are not elastic or their mechanical properties fatigue throughout multiple cycles of use. Therefore, our goal was to design a hydrogel network that is able to both dissipate energy and be resistant to fatigue of mechanical properties.

This design strategy is based on the self-assembly of blends of ABC and ABCBA block polymers, specifically polystyrene-*b*-polyisoprene-*b*-poly(ethylene oxide) (PS-PI-PEO, SIO) and polystyrene-*b*-polyisoprene-*b*-poly(ethylene oxide)-*b*-polyisoprene-*b*-polystyrene (PS-PI-PEO-PI-PS, SIOIS) into a sphere morphology where the A block is spheres of glassy, hydrophobic polystyrene surrounded by the B block of rubbery, hydrophobic polyisoprene as the surface of the sphere. These AB spherical domains sit in a matrix of the C block, poly(ethylene oxide). The spherical domains are tethered together by the SIOIS polymer so that the glassy spheres are evenly-spaced physical crosslinks in the polymer network. The tethered spheres provide the network with elasticity and fatigue resistance while the hydrophobic PI block is accessible to forcibly mix with water as a way to dissipate energy when the hydrogel is strained.

This dissertation describes the design, testing, and optimization of a hydrogel where an energy dissipation mechanism was placed directly onto every crosslink of a known elastic and fatigue-resistant

network. The possibility of even designing such a network was tested by studying the self-assembly of the SIO polymers into the ABC block polymer sphere morphology. Once, the formation of the sphere morphology in the tethered micelle network was confirmed, the effectiveness of the design strategy of a fatigue-resistant network with an intrinsic energy dissipation mechanism was studied by comparison of the mechanical properties of the SIOIS hydrogel to a similar hydrogel that is fatigue-resistant but does not contain an energy dissipation mechanism. Finally, the design of the SIOIS hydrogel is optimized by studying the effect of changes to the hydrogel processing method and changes to the PS molecular weight on the self-assembly of the energy dissipation PI block and the formation of the tethered micelle network.

ACKNOWLEDGEMENTS

I truly feel so grateful for those who have supported me through my time at CSU and in this program. Most importantly, I would like to thank my advisor, Travis Bailey. From the moment I heard him talk about science and then baseball, I knew he would be a great person to work with, and I was not disappointed. Thank you for the chances you took to be honest and helpful, the time you took to teach, and the opportunites you pushed me toward. I would also like to thank the past and present members of the Bailey group for their guidance and for their friendship. I would specifically like to thank Nabila Huq, Jackson Lewis, Alyssa Winter, Zack Umstead, Boston Morris, and Justin Gangwish. Many thanks to my committee members for their input and guidance in my career. Thank you to my campus ministry group and the members at Abiding Love whose friendship and support I greatly appreciated. Thank you to my friends who let me vent and made me laugh even though we were so far apart. Thank you to my professors at WLC who always had an ear to listen and gave me the best advice that I mostly took. Most importantly, thank you to my parents and to Kyle for pushing me to be my best even when you didn't understand it, for teaching me where my true worth lies, and for always being there for me.

The entire contents of this dissertation were written by Allee Klug with editing by Travis Bailey. Chapter 2 will be submitted for publication in the future. The experiments were designed by Allee Klug and Travis Bailey and the experiments were completed by Allee Klug. Synchrotron SAXS data were collected at Sector 12 in the X-ray Science Division of the Advanced Photon Source. This research used resources of the Advanced Photon Source, a U.S. Department of Energy (DOE) Office of Science User Facility operated for the DOE Office of Science by Argonne National Laboratory under Contract No. DE-AC02-06CH11357.

The contents of chapter 3 will be submitted for publication in the future. The experiments were designed by Allee Klug and Travis Bailey. Justin Gangwish assisted with the statistical analysis. All other experiments were performed by Allee Klug.

The experiments conducted in chapter 4 were designed by Allee Klug and Travis Bailey. The experiments were performed by Allee Klug. Guidance in the understanding of soft material mechanical testing was provided during consultations with Dr. Rong Long of CU Boulder.

Financial support for this research was supported by the National Science Foundation (DMR-1808824). The authors wish to thank the Analytical Resources Core (RRID: SCR_021758) at Colorado State University for SAXS, NMR, and DSC instrument access and training, especially Brian Newell.

DEDICATION

To all my teachers throughout the years who nurtured my love of learning

TABLE OF CONTENTS

LIST OF COMMON SYMBOLS AND CHEMICAL STRUCTURES

Symbol	Full Name	Structure or Drawing
χ (chi)	Flory interaction parameter	
BCC Spheres	Body-Centered Cubic Spheres	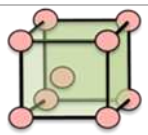
CSS	Core-Shell Sphere	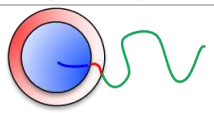
DBX	di-bromoxylene	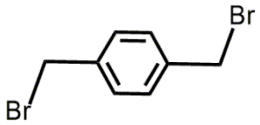
DMS	Dynamic Mechanical Spectroscopy	
DSC	Differential Scanning Calorimetry	
G’	Storage/Elastic Modulus	
G”	Loss/Viscous Modulus	
GPC	Gel Permeation Chromatography	
HEX	Hexagonally-Packed Cylinders	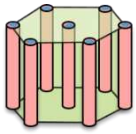
^{1}H-NMR	Proton Nuclear Magnetic Resonance Spectroscopy	
LLP Cylinders	Liquid-Like Packing of Cylinders	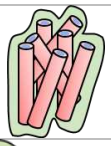
LLP Sphere	Liquid-Like Packing of Spheres	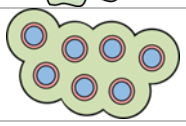
PB, B	Polybutadiene	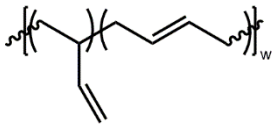
PEO, O	Poly(ethylene oxide)	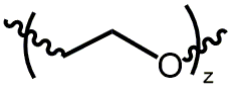

PI, I	Polyisoprene	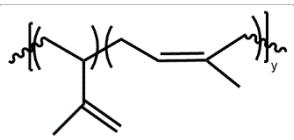
PS, S	Polystyrene	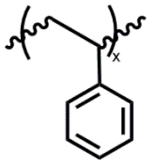
Q	Swelling ratio (g H_2O/g polymer)	
q*	Principal scattering peak from SAXS	
SAXS	Small angle X-ray scattering	
SI	Polystyrene-*b*-Polyisoprene	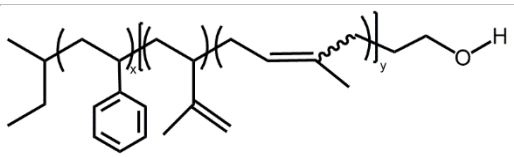
SIO	Polystyrene-*b*-Polyisoprene-*b*-Poly(ethylene oxide)	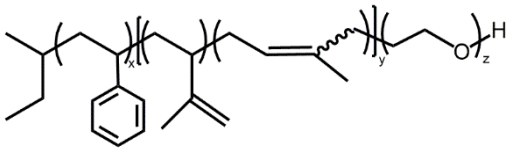
SIOIS	Polystyrene-*b*-Polyisoprene-*b*-Poly(ethylene oxide)-*b*-Polyisoprene-*b*-Polystyrene	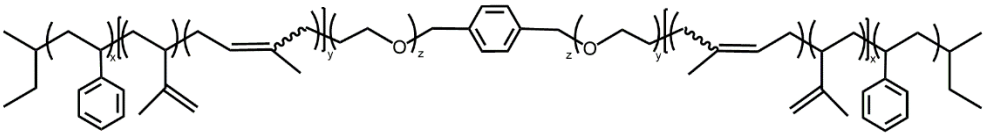
SO	Polystyrene-*b*-Poly(ethylene oxide)	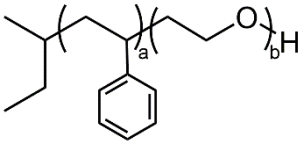
SOS	Polystyrene-*b*-Poly(ethylene oxide)-*b*-Polystyrene	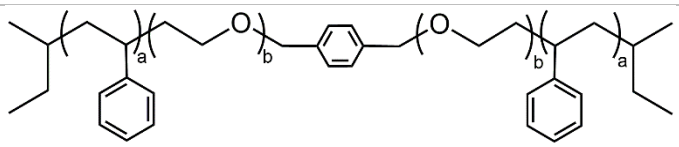
T_g	Polymer glass transition temperature	

CHAPTER 1: INTRODUCTION AND MOTIVATION OF DISSERTATION

1.1 Overview of the Dissertation

The purpose of this chapter is to provide the motivation and context of the research that became this dissertation. The goal of this project was to design a fatigue-resistant hydrogel that could also dissipate energy by inserting an energy dissipation mechanism directly into a well-known fatigue-resistant polymer network previously studied by our group formed from a blend of polystyrene-*b*-poly(ethylene oxide) (PS-PEO, SO) and polystyrene-*b*-poly(ethylene oxide)-*b*-polystyrene (PS-PEO-PS, SOS) polymers. The polymer system discussed here to make this new hydrogel network is a range of polystyrene-*b*-polyisoprene-*b*-poly(ethylene oxide) (PS-PI-PEO, SIO) triblock polymers and polystyrene-*b*-polyisoprene-*b*-poly(ethylene oxide)-*b*-polyisoprene-*b*-polystyrene (PS-PI-PEO-PI-PS, SIOIS) pentablock polymers which microphase separate into a sphere morphology to form a network of tethered micelles.

Chapter 2 details the synthetic strategies associated with synthesizing the SIO polymers at mechanically-relevant molecular weights and the volume fractions necessary for the SIO polymers to form an ABC sphere morphology. This chapter adds to the study of the ABC block polymer phase diagram by including the morphological characterization of 10 SIO polymers to establish the phase boundary between ABC cylinder-forming morphologies and ABC sphere-forming morphologies. Additionally, this chapter addresses the challenges associated with characterizing the morphologies of high molecular weight polymers in the melt. This chapter was adapted and submitted for publication.

Once the synthetic parameters of a sphere-forming SIO polymer were determined, SIO/SIOIS hydrogels were formed to study the hypothesis that adding the PI block to our previously studied SOS hydrogel system would result in a hydrogel that could dissipate more energy than the SOS hydrogel but also maintain the original resistance to the decay of mechanical properties provided by the tethered

micelle network. Chapter 3 details the comparison of the SIOIS and SOS hydrogel systems through morphological and mechanical characterization tests to test the hypothesize that the insertion of the PI block at each junction of the tethered micelle network is a way to design a fatigue-resistant and energy-dissipative network.

Finally, chapter 4 explores the structure property relationships between the formation of spheres in the SIOIS hydrogel and the energy-dissipative and fatigue-resistant properties of the hydrogel. This chapter studies first how the processing method of the SIOIS polymer before swelling affects the microphase separation within the sphere and therefore the accessibility of the PI block as an energy dissipation mechanism. Secondly, this chapter studies how the size of the PS block can affect the crosslink density within the polymer network resulting in a change in the fatigue resistance in the hydrogel mechanical response.

The remaining sections of this chapter provide the motivation and design strategy for this SIOIS fatigue-resistant and energy-dissipative hydrogel. Additionally, while a literature review is provided in the introduction to each chapter, the following discussion provides the context and motivations behind the construction of the ABC phase diagram as a part of this work and the morphological and mechanical characterization methods used in this dissertation.

1.2 Motivation and Design Strategy

1.2.1 Fatigue-Resistant Hydrogels and Energy-Dissipative Hydrogels

A hydrogel at the most basic level is a crosslinked polymer network characterized by a large water volume uptake, flexibility, and low friction.[1] Due to these advantageous properties and many similarities to natural live tissue,[2–4] the biomedical field has shown interest in hydrogels for applications ranging from tissue engineering[5–8] to drug delivery[9,10] to flexible sensors.[10–12] Between the choice of polymer used,[13,14] the construction of the polymer network,[15–17] and the types of crosslinks used in the network,[18–20] hydrogels can be tuned to have a variety of properties and applications. However, the large water content and large space between crosslinks has made hydrogels susceptible to mechanical fatigue

over multiple cycles of use.[21,22] Additionally, hydrogels are often brittle, similar to other elastomers, which has limited their widespread use in these more mechanically intensive roles such as tissue engineering.[23–25] Currently, the hydrogel field has input a great deal of study into designing hydrogels that overcome these problems. While resistance to fatigue[7] and toughness[26–28] have both been implemented into hydrogel networks individually, current hydrogel science has struggled to produce a material that exhibits both properties in any significant capacity.[16]

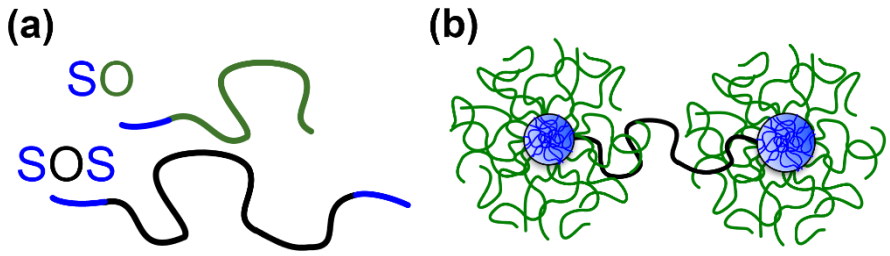

Figure 1.1: (a)AB block polymer and ABA block polymer. Blue represents the Polystyrene (PS,S), green represents poly(ethylene oxide) (PEO, O) and black represents PEO chains which are coupled together to make ABA block copolymers. (b) The blend of AB and ABA block copolymers self-assemble to form a sphere morphology where PS forms glassy spheres surrounded by a matrix of PEO chains to form micelles. SOS chains tether the spheres together to form the tethered micelle network.

A hydrogel with fatigue resistance (a resistance to decay in mechanical performance) has been created and characterized by the Bailey group with the additional advantages of exhibiting a high modulus at low strains and elastic recovery following compression on the order of one second or less.[29] Hydrogels which show fatigue typically suffer from a network having a wide distribution of strand lengths (segments of chains adjoining crosslinks).[30,31] When the strands are stretched or compressed, the stress is concentrated in the shorter strands promoting chain scission through covalent bond breakage. As these strands break, the number of crosslinks providing the material's stiffness or modulus is decreased. Recently, our group has created a hydrogel from polystyrene-*b*-polyethylene oxide (PS-PEO, SO), a thermoplastic elastomer, with exceptional fatigue resistance and fast recovery over a large number of cycles.[32] This blend of AB and ABA block copolymers forms a sphere morphology (Figure 1.1) with amphiphilic character, in which the spherical cores are hydrophobic PS, while the matrix in which the spheres sit is comprised of hydrophilic PEO. The strands that tether spherical domains have a very narrow

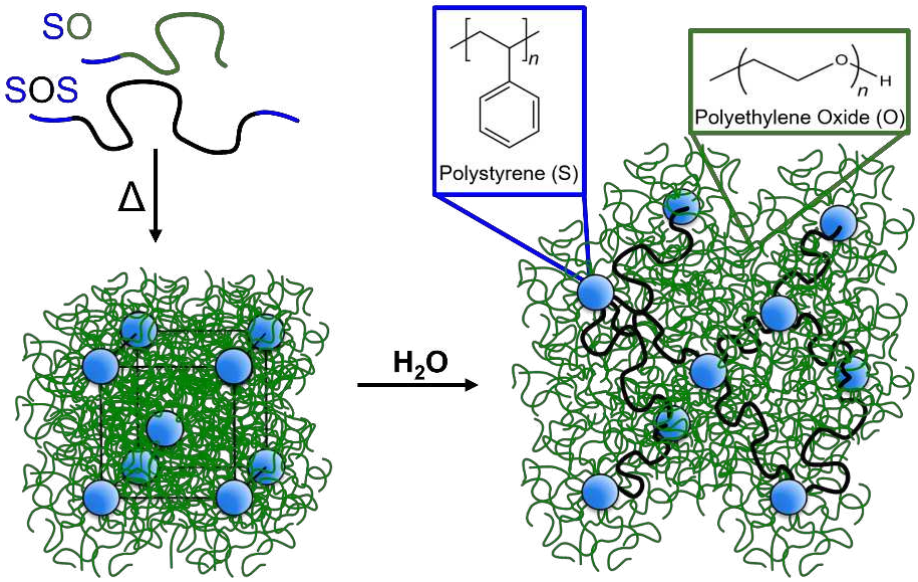

Figure 1.2: When heated, the polymers phase separate into glassy PS spheres sitting in a PEO matrix while the spheres are tethered together by SOS. When swollen, the spheres act as physical crosslinks provided structure to the polymer network.

distribution of molecular weights, causing nearly identical chain lengths (Figure 1.2). The spherical cores are ordered in a body-centered cubic lattice, ensuring a spatially even distribution of crosslinks in the network. The high density of entanglements among the tethers act as additional mobile crosslinks which can move in order to rapidly redistribute stress when the network is under strain. Figure 1.3 shows an example stress-strain curve for an SOS hydrogel that can be characterized as highly elastic, possessing a high modulus at low strains, and exhibits rapid recovery of upon removal of the load. The data shown

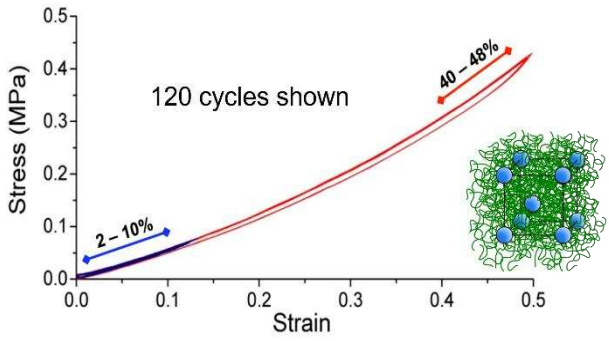

Figure 1.3: Compressive stress-strain curve of and SOS sample for 120 cycles at 1 Hz and 12% peak strain with an increase to ~40% peak strain every 11th cycle.

include 120 successive compressions cycles performed at 1 Hz (overlaid), giving a sense of the resistance of the material to mechanical property fatigue with time.

Despite this excellent collection of properties, the SOS hydrogels have also proven to be quite susceptible to fracture and brittleness. In highly elastic materials, like a nitrile glove, formation of a small crack leads to rapid crack propagation, ultimately causing catastrophic failure in the material. The main problem with these materials and many elastomers is a lack of any mechanism that allows for energy dissipation within regions of high stress concentration. A crack in a strained material results in the stress from mechanical loading to be concentrated at the crack tip. This manifests in bond fracture within the polymer chains making up the network strands. In swollen hydrogels, the reduced areal chain density further exacerbates the localized concentrations of stress, in comparison, with solid elastomers.

Many groups have worked to incorporate energy dissipation into hydrogel networks. Gong's well known double network hydrogel dissipates energy by having one tightly crosslinked network and one loosely crosslinked network (Figure 1.4a).[28,33,34] Under strain, the tightly crosslinked network produces high moduli, but also easily fractures, with sacrificial covalent bond breaking providing a means of dissipating very large amounts of energy while the loose network remains relaxed preventing catastrophic failure of the hydrogel. However, this mechanism of dissipation creates permanent damage (fatigue), leaving the network vulnerable to future fracture and a low modulus for all future cycles (Figure 1.4b). Recoverable, non-damaging energy dissipation mechanisms such as mechanical de-aggregation of

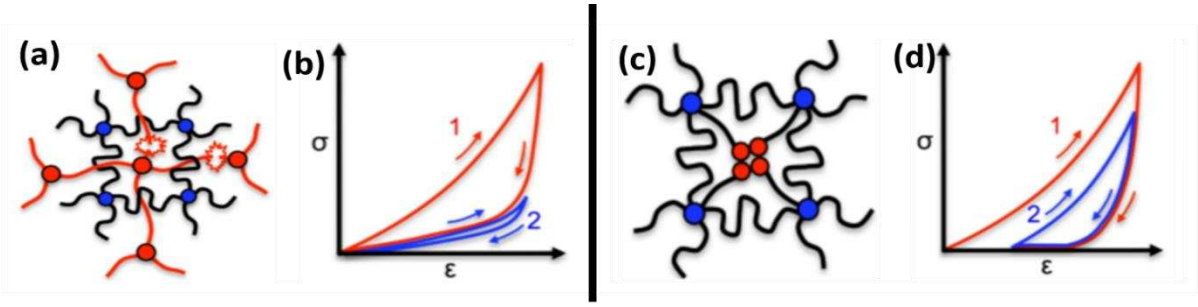

Figure 1.4: (a) Double network hydrogel with tightly crosslinked network (red) designed to fracture under strain and a loosely cross-linked network (black) which provides shape to the gel (b)A stress-strain curve of the double network hydrogel. The first loading cycle shows energy dissipation but the second loading shows a permanent loss of modulus. (c)Hydrogel with recoverable energy dissipation mechanisms. (d) Energy dissipation is seen in both loading cycles, but the recovery is slow causing temporary plastic deformation of the material.

hydrophobic aggregates or bonds, or mechanical dissociation of charged species have also been explored (Figure 1.4c).[27,35,36] While these toughening mechanisms do not produce permanent damage, their recovery is time-limited by re-association time-constants. This re-association can be long in the case of reassembly of hydrophobic aggregates, or so rapid (in the case of electrostatic interaction) that reformation while the network is still under strain inhibits the materials time to recovery. The recovery of most of these materials can take anywhere from minutes to days. Immediate reloading cycles exhibit evidence of residual plastic deformation (Figure 1.4d). So far, even the most advanced networks built to dissipate energy have also actively countered any fatigue resistance the network could provide when evaluated under reasonable loading rates (second or sub-second time-scales).

1.2.2 Design Strategy for a Fatigue-Resistant and Energy-Dissipative Hydrogel:

To build a fatigue-resistant and tough hydrogel, we hypothesized that the hydrogel network must be designed to intrinsically include both properties. The hydrogel network must have energy dissipation at every molecular strand to create a homogeneous network and minimize areas of stress concentration. The energy dissipation mechanism cannot be permanent in order to allow additional energy dissipation to occur in future loading cycles or mechanical events. Also, there needs to be an energy dissipation mechanism that is compatible with rapid recovery, rather than working against it, to prevent temporary plastic deformation.

Our strategy to design a fatigue-resistant and energy-dissipative hydrogel has been to introduce an elastic, hydrophobic polymer B block between the hydrophobic polystyrene cores and the hydrophilic polyethylene oxide corona to create a blend of ABC and ABCBA block copolymers. The volume fractions of each block were chosen so the polymers self-assemble into a sphere morphology (Figure 1.5a). In this morphology, the rubbery B block forms a collapsed shell around the glassy PS core. The PEO is solvated with water, forming a matrix surrounding each core and shell domain which are situated on a BCC lattice. Pentablock (ABCBA) copolymer formed by the coupling of two PEO (C block) chain termini in an ABC triblock copolymer creates the tethered micelle network shown to have good fatigue

resistance previously by our group. Ultimately, the increased toughness of the hydrogel lies with the energy dissipation capabilities of the inserted B block.

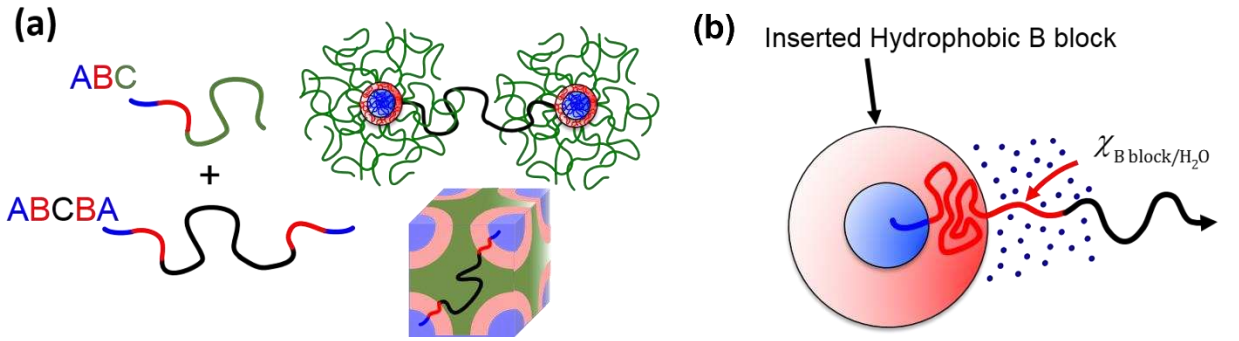

Figure 1.5: (a) ABC and ABCBA block copolymers are blended to form a core-shell sphere morphology again formed by tethered micelles. The A block (blue) forms cores surrounded by the B block (red). The AB spheres sit in the matrix of the C block (green). The spheres are tethered together by ABCBA polymers (black). (b) Under strain, the hydrophobic B block is extended into the water matrix in order to dissipate energy from the system.. The energy dissipated is measured by the forced interaction between the B block and H_2O.

The potential for energy dissipation in this system is based on the hypothesis that strain transferred to this new B block will result in forced contact between its hydrophobic backbone and the hydrophilic solvent, water. A large part of the energy required to create such contacts is energy that will be dissipated. The magnitude can be approximated by considering the free energy of mixing of a polymer-solvent solution between the B block and the aqueous phase (Equation 1.1).

$$\Delta G_m = \Delta H_m - T\Delta S_m \qquad \textbf{Equation 1.1}$$

When strain is placed on the hydrogel, mechanical energy will cause the solvated PEO chains to stretch, an entropically unfavorable configuration. At some point when the strain in the PEO chains becomes high enough, we hypothesize some of the mechanical energy being placed on the system will be used to stretch the B block into the hydrogel matrix rather than breaking the C-O bonds in PEO (Figure 1.5b). This will mechanically raise the enthalpy associated with introducing the hydrophobic B block into the aqueous region of the hydrogel matrix. The change in enthalpy in the strained hydrogel comes from the forced mixing of two unlike blocks. Equation 2 shows the terms that determine ΔH_m where k is Boltzmann's constant, T is temperature, χ is the polymer-solvent interaction parameter, and n_p and θ_s are

the volume fractions of polymer and water respectively.[37] Therefore, one of the ways to change the amount of energy dissipated by the hydrogel network is to change the value of χ.

$$\Delta H_m = \mathrm{kT}\chi n_p \theta_s \qquad \textbf{Equation 1.2}$$

By choosing a B block with sufficiently high hydrophobicity, the increase in enthalpy will exceed the entropic advantage associated with mixing the dissimilar species; thus, the net change in free energy of mixing the B block and water will overall be positive. This means the formation of the polymer solution requires the input of mechanical energy much like shaking a bottle of oil and water. The fraction of the mechanical energy that contributes to the creation of such an unfavorable solution is energy that will be dissipated. When the strain is released, the B block and PEO chains will elastically return to their original conformational states because of the entropically-driven restoring force intrinsic to stretched polymer chains.

Polyisoprene (PI) has been chosen for this middle block because it is sufficiently hydrophobic and can be inserted into the current anionic polymerization procedure used in our group for PS-PEO. Polyisoprene also is liquid/rubbery at room temperature with a T_g around -70ºC.[38]

While a "tough" hydrogel is part of the ultimate goal for hydrogel materials, this work will focus on the effectiveness of the design strategy to produce a hydrogel that dissipates more energy than a hydrogel without the PI block energy-dissipative mechanism while maintaining the fatigue-resistant properties of the tethered micelle network. As part of the network design, the dissipation of energy within the network should lead to a tougher hydrogel, but toughness is not the primary measure of success for the hydrogel design at this time.

1.3 Background for Morphological and Mechanical Characterization

1.3.1 ABC Block Polymer Sphere Morphology Formation

The design strategy of this fatigue-resistant and energy-dissipative hydrogel relies on the polymer chains self-assembling into a sphere morphology. This morphology is comprised of spheres composed of polymer blocks A and B arranged on a body-cubic centered lattice (BCC) in a matrix of polymer block C. Once C chains are coupled to each other, the spheres act as physical crosslinks when the hydrogel is strained, distributing stress across the network, and providing fatigue resistance to the hydrogel. In ABC block polymers, the spheres are further phase separated into an A block core and a B block shell. This configuration makes the B block accessible to be pulled into the water as the energy dissipation mechanism. The synthesis of ABC polymers which form the sphere morphology therefore is a crucial objective to designing a fatigue-resistant and energy-dissipative hydrogel.

Morphology, or periodic structure, in block copolymers occurs because of microphase separation of the blocks as a means to decrease the free energy of the system.[39–41] The enthalpic penalty of mixing two unlike polymer segments is measured by the Flory-Huggins interaction parameter, χ. This parameter represents the contact energy between the two blocks. High values of χ correspond to large enthalpic penalties of contact between the polymer molecules. Segregation of the blocks reduces contact between the unlike molecules which decreases the enthalpy, and therefore, produces the lowest free energy state. χ is inversely related to temperature ($\chi \propto 1/T$) so the energetic drive for polymers to separate can be lowered by raising the temperature. The enthalpic desire to separate blocks is countered by the loss of entropy associated with the reduction of mixing and the stretching of the polymer chains required to accommodate the separation. For most multipolymer systems, χ is large enough to overcome the entropic penalty of separation. Chain length can further lower the entropic penalty. As the number of polymer molecules(N) in a chain increases, there are fewer possible unique mixing configurations, therefore $\Delta S \propto 1/N$. The ratio of these entropic and enthalpic components (a measure of their distribution within the free energy) governing phase separation is represented by the product χN. If χ or N are sufficiently

lowered, the entropy will dominate forcing the system to mix into a disordered state. However, as χ or N are raised, the enthalpy begins to dominate forcing the structure to order by separating the phases.

When the value of χN is high enough for the polymer to phase separate, the free energy of the system is further lowered by separating into an ordered structure, or morphology. The morphology formed during phase separation is influenced by the volume of space each block occupies called the volume fraction (f). The structure formed again balances minimizing interfacial contact between unlike blocks with minimizing chain stretching. At asymmetric volume fractions, this results in curvature of the interfaces between the blocks as each tries to fill volume while also minimizing contact with the other block.[42] When the asymmetry of the blocks is large enough, this tendency towards curvature leads to the formation of isolated spheres of the smaller volume fraction block.

Phase diagrams provide information about volume fractions and χ values where morphologies can be expected and targeted synthetically. While AB diblock copolymer morphology is well understood and has been studied,[40,43] ABC triblock copolymer morphologies are considerably more complex with few comprehensive, experimental ABC phase diagrams yet to be established. This complexity manifests from the presence of five parameters governing the formation of an ABC morphology: the volume fraction of the A blocks (f_A) and B blocks(f_B) and the immiscibility between each block (χ_{AB}, χ_{BC}, χ_{AC}) compared to just two parameters (f_A, χ_{AB}) for AB block copolymers. In the AB phase diagram, the sphere morphology is formed when there is an asymmetrically large volume fraction of either block. Similarly, all computational ABC phase diagrams place the phase region for sphere formation at asymmetrically large regions of one of the three blocks.[42,44–50] One such ideal ABC phase diagram was constructed using self-consistent field theory (SCFT) by Morse and coworkers (Figure 1.6).[42] This computational phase diagram was chosen to use this as a guide for targeting the CSS morphology. The core-shell sphere morphology, shown by S on the phase diagram, is the morphology expected from the melt self-assembly of three blocks with relative χ values $\chi_{AB} < \chi_{BC} < \chi_{AC}$ and large volume fractions of one of the end blocks. Our system is more accurately described by relative χ values $\chi_{AB} < \chi_{AC} < \chi_{BC}$. This should not change whether the morphology forms but may change the volume fraction phase boundaries or temperature phase

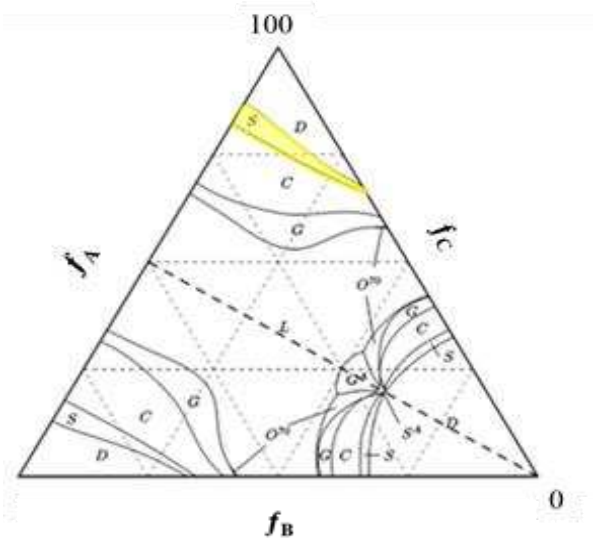

Figure 1.6 : Ideal ABC polymer phase diagram from SCFT calculations used as a guide for synthetic targeting of morphology from Morse et.al. The highlighted region represents the core-shell-sphere phase region (S). Each axis represents a block volume fraction with numbers shown corresponding to the C block.

boundaries where core-shell spheres form in our material compared to other ABC systems. Experimentally, literature in this region of the phase diagram for any ABC polymer systems is sparse which further complicates the immediate targeting of the CSS morphology. The few sphere morphologies that have been observed experimentally[51–54] also roughly fall into this asymmetrical region. Unfortunately, many of these morphologies are formed using solvent-casting and solvent vapor annealing methods rather than in the melt. While solvent processing can be useful, solvent selectivity to a one or more of the blocks can result in mesophases which, while intriguing, do not represent the equilibrium morphology of the ABC polymer. Additionally, solvent-casting requires processing times on the scale of days to weeks which is not ideal for eventual scaling of the processing method to form hydrogels. The most studied sphere-forming system has been of ABC polymers with asymmetrically large B blocks[53,55] which can have very different phase boundaries than with large sections the A or C block as seen in Figure 6. The specific morphological behavior of PS-PI-PEO has been studied but with nearly equal volume fractions of all three blocks.[56] A comprehensive phase diagram[57] was constructed for PI-PS-PEO polymers, but did not extend into the volume fraction range where spheres are expected to form according

to Morse. Therefore, the computationally predicted phase diagram by Morse will still be useful for choosing specific volume fractions as a way to target the core-shell sphere morphology.[42]

The synthesis and characterization of multiple polymers in this largely unexplored phase region accomplishes the additional goal of filling in the gap in the literature in this asymmetrically large C block region of the phase diagram. The characterization of the polymer morphologies is carried out using small-angle X-ray scattering and rheology. The specifics and polymer properties of ABC polymers in relation to those characterization methods is described in Appendix D.

1.3.1 Mechanical Characterization of the Hydrogel

While mechanical tests do not provide direct and specific insight into the molecular design of a network, they are able to give a broad understanding of a network design especially in polymer systems where the relationship between molecular structures such as chain entanglements and mechanical properties such as modulus and elasticity has been well-studied.[58] Additionally, the properties studied during mechanical testing are macroscopic traits which carry relevance to the use of materials in real-world applications. Therefore, mechanical testing of the hydrogels is used to test the accuracy of our hypothesis of the design of a fatigue-resistant and energy-dissipative hydrogel. The hydrogels were subjected to cyclic compression tests, tensile to break test, and cyclic tensile tests which produce stress-strain curves for the hydrogel. A description of a stress-strain curve can be found in Appendix D.

To measure the energy dissipation of the SIOIS hydrogel, we will be measuring the hysteresis between the loading and unloading curves in both cyclic compression and cyclic tensile testing where a sample is loaded and unloaded under a specified strain rate (Figure 1.7a).[16] During loading in the SOS hydrogel, the stress on the polymer chain is derived from the energy it takes to rotate the bonds in the PEO backbone to strain the PEO polymer to a new length. Then, during unloading, the polymer is experiencing the entropic restoring force of the polymer chain. Therefore, all of the energy that went into stretching the polymer chain is stored in the chain as potential energy for when the strain on the polymer is removed to force the polymer back into its original conformation. The polymer is experiencing the

same stress on the polymer chain during loading and unloading but in opposite directions. Therefore, we will expect the SOS hydrogel to exhibit stress-strain curves where the loading and unloading curves are nearly overlapping. It is likely that there will some small amount of hysteresis between the curves due to the loading compression pushing water out of the hydrogel that does not return as quickly upon unloading as the polymer is returning to its conformation (Figure 1.7b).

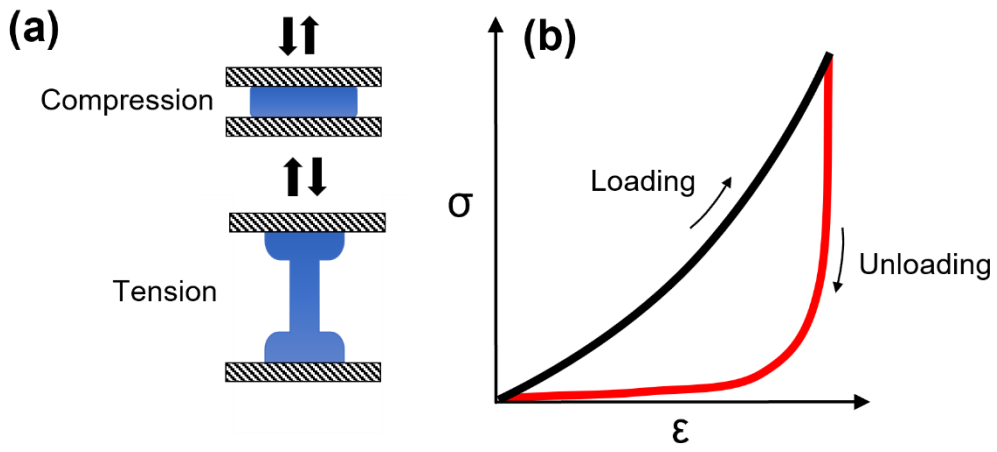

Figure 1.7: (a) Schematic depictions of compression testing and uniaxial tensile testing. (b) Hypothetical stress-strain curve for the SIOIS gel. Energy dissipation is shown as the hysteresis area between the loading and unloading curves.

In contrast, when the SIOIS hydrogel is strained, the energy of stretching the polymer chain is combined with the forced mixing of the PI block with the PEO/water matrix. When the strain is released, the energy of mixing with the water is dissipated as heat rather than stored in the chain resulting in the polymer chain experiencing less energetic force during unloading as compared to the energy put into the system during loading. This lower energetic load is observed as the polymer experiencing less stress at each strain during unloading than it did during loading. The difference between the loading and the unloading curves is therefore the energy that was dissipated during the PI block entering the PEO/water matrix. Energy dissipation is measured in units of energy, kJ/m^3.

The elasticity, modulus, and recovery times of the hydrogels will also be measured in accordance to previous tests completed on SOS hydrogels.[7] The elasticity of the gel is provided by the evenly-spaced PS physical crosslinks which are able to move instead of breaking during loading before returning back to their original positions upon unloading due to entropic restoring forces of the polymer chains resulting in

no change in the start and end cycle strain. The modulus is a measure of the crosslinking density of the network and is closely related to the swelling ratio in the SOS hydrogels. Finally, the recovery time of the hydrogel back to its original size after unloading is inherent to the entropic restoring forces of the hydrogel polymer chains and is measured by consecutive compression cycles with less than one second recovery time between cycles. These are all properties that are inherent to the tethered micelle network of the SOS hydrogel and therefore we also expect to observe in the SIOIS because it is designed to have the same network of tethered PS spheres.

Whether the amount of energy dissipation, elasticity, modulus, and recovery times change over the course of multiple compression cycles will measure the fatigue-resistant properties of the SIOIS hydrogel. In a fatigue-resistant hydrogel, we would expect to see no change in these properties over multiple cycles.

Uniaxial tensile tests until sample failure will also be used to provide a measure of the bulk toughness or deformation energy of the material. This is a measure of the energy per unit volume a material can absorb before failure and is therefore measured with units kJ/m^3. The tensile test strains the polymer chains causing rotation of the chains until they reach a point of failure. Due to the much larger strains capable in a tensile apparatus compared to compression, the tensile tests in these hydrogels can result in a large concentration of stress which result in microcracks especially at defect sites within the network. This test will inform us whether the energy dissipation mechanism is sufficient to have an effect on the formation and propagation of these cracks at a macroscopic level by observing any change in the overall bulk toughness of the hydrogel.

The total area under the stress-strain curve provides the bulk toughness for the sample. While an unloading curve is not observed in tensile-to-break tests, the tests can tell us if there are differences in the tensile strain at break, tensile stress at break, and tensile modulus throughout the test between the SIOIS and SOS hydrogels as a way to understand the molecular structure of the SIOIS hydrogel.

1.4 Final Remarks

At the end of this dissertation, appendices (A, B, and C) for Chapters 2-4 can be found with supporting information from each respective chapter. Appendix D provides technical explanations of the polymer synthesis and molecular, morphological, and mechanical characterization techniques used in these chapters. Chapter 5 provides a summary of the conclusions from the chapters as well as a look at future directions for research based on the conclusions on this dissertation.

1.5 References

1. Creton, C. 50th Anniversary Perspective: Networks and Gels: Soft but Dynamic and Tough. *Macromolecules* **50**, 8297–8316 (2017).

2. Cascone, S. & Lamberti, G. Hydrogel-based commercial products for biomedical applications: A review. *Int. J. Pharm.* **573**, (2020).

3. Jacob, S. *et al.* Emerging role of hydrogels in drug delivery systems, tissue engineering and wound management. *Pharmaceutics* **13**, 1–36 (2021).

4. Campea, M. A., Majcher, M. J., Lofts, A. & Hoare, T. A Review of Design and Fabrication Methods for Nanoparticle Network Hydrogels for Biomedical, Environmental, and Industrial Applications. *Adv. Funct. Mater.* **31**, (2021).

5. Wei, W. *et al.* Advanced hydrogels for the repair of cartilage defects and regeneration. *Bioact. Mater.* **6**, 998–1011 (2021).

6. Lee, K. Y. & Mooney, D. J. Hydrogels for Tissue Engineering. *Chem. Rev.* **101**, 1869–1879 (2001).

7. Lewis, J. T., Fischenich, K. M., Haut Donahue, T. L. & Bailey, T. S. Nanostructure-Driven Replication of Soft Tissue Biomechanics in a Thermoplastic Elastomer Hydrogel. *ACS Biomater. Sci. Eng.* **4**, 3854–3863 (2018).

8. Fischenich, K. M., Lewis, J. T., Bailey, T. S. & Donahue, T. L. H. Mechanical viability of a thermoplastic elastomer hydrogel as a soft tissue replacement material. (2018) doi:10.1016/j.jmbbm.2018.01.010.

9. Li, G., Wang, Y., Wang, S. & Jiang, J. A Tough Composite Hydrogel can Controllably Deliver Hydrophobic Drugs under Ultrasound. *Macromol. Mater. Eng.* **303**, 1–6 (2018).

10. Li, Z. & Loh, X. J. Recent advances of using polyhydroxyalkanoate-based nanovehicles as therapeutic delivery carriers. *Wiley Interdiscip. Rev. Nanomedicine Nanobiotechnology* **9**, e1429 (2017).

11. Ge, G. *et al.* Muscle-Inspired Self-Healing Hydrogels for Strain and Temperature Sensor. *ACS Nano* **14**, 218–228 (2020).

12. Deng, Z. *et al.* Stimuli-Responsive Conductive Nanocomposite Hydrogels with High Stretchability, Self-Healing, Adhesiveness, and 3D Printability for Human Motion Sensing. (2019) doi:10.1021/acsami.8b20178.

13. Spicer, C. D. Hydrogel scaffolds for tissue engineering: the importance of polymer choice. *Polym. Chem.* **11**, 184 (2019).

14. Desai, M. S. *et al.* Elastin-Based Rubber-Like Hydrogels. *Biomacromolecules* **17**, 2409–2416 (2016).

15. King, D. R., Okumura, T., Takahashi, R., Kurokawa, T. & Gong, J. P. Macroscale Double Networks: Design Criteria for Optimizing Strength and Toughness. *ACS Appl. Mater. Interfaces* **11**, 35343–35353 (2019).

16. Zhao, X. Multi-scale multi-mechanism design of tough hydrogels: Building dissipation into stretchy networks. *Soft Matter* vol. 10 672–687 (2014).

17. Dhand, A. P., Galarraga, J. H. & Burdick, J. A. Enhancing Biopolymer Hydrogel Functionality through Interpenetrating Networks. *Trends Biotechnol.* **39**, 519–538 (2021).

18. Wang, H. & Heilshorn, S. C. Adaptable Hydrogel Networks with Reversible Linkages for Tissue Engineering. *Adv. Mater.* **27**, 3717–3736 (2015).

19. Li, L., Scheiger, J. M. & Levkin, P. A. Design and Applications of Photoresponsive Hydrogels. *Adv. Mater.* **31**, (2019).

20. Klouda, L. Thermoresponsive hydrogels in biomedical applications A seven-year update. *European Journal of Pharmaceutics and Biopharmaceutics* (2015) doi:10.1016/j.ejpb.2015.05.017.

21. Bai, R., Yang, J. & Suo, Z. Fatigue of hydrogels. *Eur. J. Mech. A/Solids* **74**, 337–370 (2019).

22. Zhang, E., Bai, R., Morelle, X. P. & Suo, Z. Fatigue fracture of nearly elastic hydrogels. *Soft Matter* **14**, 3563 (2018).

23. Rivlin, R. S. & Thomas, A. G. Rupture of rubber. I. Characteristic energy for tearing. *J. Polym. Sci.* **10**, 291–318 (1953).

24. Long, R. & Hui, C.-Y. Fracture toughness of hydrogels: measurement and interpretation. *Soft Matter* **12**, 8069–8086 (2016).

25. Mao, Y. & Anand, L. A theory for fracture of polymeric gels. *J. Mech. Phys. Solids* **115**, 30–53 (2018).

26. Luo, F. *et al.* Oppositely charged polyelectrolytes form tough, self-healing, and rebuildable hydrogels. *Adv. Mater.* **27**, 2722–2727 (2015).

27. Su, E. & Okay, O. Polyampholyte hydrogels formed via electrostatic and hydrophobic interactions. *Eur. Polym. J.* **88**, 191–204 (2017).

28. Gong, J. P., Katsuyama, Y., Kurokawa, T. & Osada, Y. Double-network hydrogels with extremely high mechanical strength. *Adv. Mater.* **15**, 1155–1158 (2003).

29. Lewis, J. T. & Bailey, T. S. No Title. *To be Submitt.*

30. Sakai, T. *et al.* Highly elastic and deformable hydrogel formed from tetra-arm polymers. *Macromol. Rapid Commun.* **31**, 1954–1959 (2010).

31. Okumura, Y. & Ito, K. The polyrotaxane gel: A topological gel by figure-of-eight cross-links. *Adv. Mater.* **13**, 485–487 (2001).

32. Guo, C. & Bailey, T. S. Highly distensible nanostructured elastic hydrogels from AB diblock and ABA triblock copolymer melt blends. *Soft Matter* **6**, 4807 (2010).

33. Gong, J. P. Why are double network hydrogels so tough? *Soft Matter* **6**, 2583 (2010).

34. Sun, T. L. *et al.* Bulk Energy Dissipation Mechanism for the Fracture of Tough and Self-Healing Hydrogels. *Macromolecules* **50**, 2923–2931 (2017).

35. Sun, T. L. *et al.* Physical hydrogels composed of polyampholytes demonstrate high toughness and viscoelasticity. *Nat. Mater.* **12**, (2013).

36. Luo, F. *et al.* Strong and Tough Polyion-Complex Hydrogels from Oppositely Charged Polyelectrolytes: A Comparative Study with Polyampholyte Hydrogels. *Macromolecules* **49**, 2750–2760 (2016).

37. Hiemenz, P. C. & Lodge, T. P. *Polymer Chemistry*. (2007).

38. Widmaier, J. M. & Meyer, G. C. Glass Transition Temperature of Anionic Polyisoprene. *Rubber Chem. Technol.* **54**, 940–943 (1981).

39. Bates, F. S. Polymer-Polymer Phase Behaviour. *Science (80-.).* **251Miscell**, 898–905 (1991).

40. Bates, F. Block Copolymer Thermodynamics: Theory And Experiment. *Annu. Rev. Phys. Chem.* **41**, 525–557 (1990).

41. Fredrickson, G. H. & Bates, F. S. Dynamics of Block Copolymers: Theory and Experiment. *Annu. Rev. Mater. Sci.* (1996) doi:10.1146/annurev.ms.26.080196.002441.

42. Tyler, C. A., Qin, J., Bates, F. S. & Morse, D. C. SCFT study of nonfrustrated ABC triblock copolymer melts. *Macromolecules* **40**, 4654–4668 (2007).

43. Matsen, M. W. & Schick, M. *Stable and Unstable Phases of a Diblock Copolymer Melt*. vol. 72 (1994).

44. Löbling, T. I. *et al.* Bulk morphologies of polystyrene-block-polybutadiene-block-poly(tert-butyl methacrylate) triblock terpolymers. *Polymer (Guildf).* **72**, 479–489 (2015).

45. Zhou, Y., Long, X., Xue, X., Qian, W. & Zhang, C. Morphologies and dynamics of linear ABC triblock copolymers with different block sequences. *RSC Adv.* **5**, 7661–7664 (2015).

46. Liu, H. H., Huang, C. I. & Shi, A. C. Self-Assembly of Linear ABCBA Pentablock Terpolymers. *Macromolecules* **48**, 6214–6223 (2015).

47. Liu, M., Li, W., Qiu, F. & Shi, A. C. Theoretical study of phase behavior of frustrated ABC linear triblock copolymers. *Macromolecules* **45**, 9522–9530 (2012).

48. Qin, J., Bates, F. S. & Morse, D. C. Phase behavior of nonfrustrated ABC triblock copolymers: Weak and intermediate segregation. *Macromolecules* **43**, 5128–5136 (2010).

49. Tang, P., Qiu, F., Zhang, H. & Yang, Y. Morphology and phase diagram of complex block copolymers: ABC linear triblock copolymers. *Phys. Rev. E - Stat. Nonlinear, Soft Matter Phys.* **69**, (2004).

50. González-Pizarro, D. A., Soto-Figueroa, C., Rodríguez-Hidalgo, M. D. R. & Vicente, L. Mesoscopic study of the ternary phase diagram of the PS-PB-P: T BMA triblock copolymer: Modification of the phase structure by the composition effect. *Soft Matter* **14**, 508–520 (2018).

51. Breiner, U., Krappe, U., Jakob, T., Abetz, V. & Stadler, R. Spheres on spheres - A novel spherical multiphase morphology in polystyrene-block-polybutadiene-block-poly(methyl methacrylate) triblock copolymers. *Polym. Bull.* **40**, 219–226 (1998).

52. Gil Haenelt, T., Meyer, A., Abetz, C. & Abetz, V. Planet-Like Nanostructures Formed by an ABC Triblock Terpolymer. *Macromol. Chem. Phys.* **220**, (2019).

53. Mogi, Y. *et al.* Preparation and Morphology of Triblock Copolymers of the ABC Type. *Macromolecules* **25**, 5408–5411 (1992).

54. Tang, C. *et al.* Square packing and structural arrangement of ABC triblock copolymer spheres in thin films. *Macromolecules* **41**, 4328–4339 (2008).

55. Mogi, Y. *et al.* Superlattice Structures in Morphologies of the ABC Triblock Copolymers. *Macromolecules* **27**, 6755–6760 (1994).

56. Bailey, T. S., Pham, H. D. & Bates, F. S. Morphological behavior bridging the symmetric AB and ABC states in the poly(styrene-b-isoprene-b-ethylene oxide) triblock copolymer system. *Macromolecules* **34**, 6994–7008 (2001).

57. Chatterjee, J., Jain, S. & Bates, F. S. Comprehensive phase behavior of poly(isoprene-b-styrene-b-ethylene oxide) triblock copolymers. *Macromolecules* **40**, 2882–2896 (2007).

58. Fetters, L. J., Lohse, D. J., Richter, D., Witten, T. A. & Zirkel, A. Connection between Polymer Molecular Weight, Density, Chain Dimensions, and Melt Viscoelastic Properties. *Macromolecules* vol. 27 4639–4647 (1994).

CHAPTER 2: MELT ASSEMBLY IN HIGHLY ASYMMETRIC ABC BLOCK POLYMERS

2.1 Summary

Ten ABC block polymers were synthesized with highly asymmetric volume fractions with majority C blocks (up to f_c=0.92) and varying A:B volume fraction ratios to examine the largely unexplored melt state self-assembly of sphere phases in ABC systems. The polymer systems studied were polystyrene-*b*-polybutadiene-*b*-poly(ethylene oxide) (PS-PB-PEO, SBO) and polystyrene-*b*-polyisoprene-*b*-poly(ethylene oxide) (PS-PI-PEO, SIO), where PEO was used as the majority C block. SAXS and rheology were used to confirm the microphase separation of the block polymers which exhibited both periodic morphologies (body-centered cubic spheres and hexagonally-packed cylinders) and non-periodic, liquid-like morphologies (liquid-like packing of spheres and liquid-like cylinders). The total molecular weight of the polymer was found to be a determining factor in the ability of the system to kinetically achieve morphologies with a high degree of periodic order. Specifically, ABC block polymers with a total molecular weight larger than 100kDa were limited to liquid-like organization in these specific systems.

2.2 Introduction

Over the past three decades, the exploration of ABC block polymer phase behavior has engendered the discovery of over 50 unique periodically organized morphologies, both thermodynamically stable and kinetically trapped.[1,2,11,12,3–10] Continued attention is rooted in the potential of nanoscale periodic morphology to provide unique mechanical, optical, and electrical properties to a polymer system.[13–17] Block polymers exhibiting such unique morphological behavior have, for example, been applied as functional components in biomedical devices[18–20] photonic crystals[21,22] and wearable electronic devices.[23,24] The unique properties created by these morphologies emerge from the individual polymer blocks' chemical and physical properties, the overall interfacial geometry inherent to the

morphological structure, and/or the juxtaposition of the individual domains comprising the morphology. Judicious choice of the individual polymers making up the ABC system, in combination with the morphology adopted, allows one to tailor the overall emergent functions of the material.

Our group has been exploiting the nanoscale structure achievable through block polymer self-assembly to impart enhanced mechanical performance and fatigue-resistance to polymer hydrogels. The improved mechanical elasticity, tunable modulus, and inherent fatigue resistance is achieved using blends of AB and ABA block polymers where the A block is hydrophobic and glassy, and the B block is hydrophilic. The blocks are synthesized to the correct volume fractions for the AB and ABA block polymer blends to microphase separate into a sphere morphology with the A block forming glassy spheres situated in a matrix of B block chains. A significant fraction of the B blocks belonging to the ABA block polymer span adjacent spherical A domains, acting as physical crosslinks in the hydrogel when the thermally processed blend is subsequently swollen in water. In this hydrogel, the sphere morphology, combined with the amphiphilic nature of the selected AB system and its intrinsic thermoplasticity as a precursor material, provides us with swollen hydrogels that are highly elastic and fatigue resistant without relying on chemical crosslinks. While the hydrophobicity and philicity of individual polymer blocks provide the required properties to form a hydrogel, the utility of the sphere morphology and the glassy behavior of the spherical domain is fundamental to the enhanced mechanical performance.[18,25]

Our group has hypothesized that advanced forms of these hydrogels can be developed by the inclusion of a third polymeric component between the two existing blocks to make ABC and ABCBA block polymers. Forming a new domain positioned between the glassy spheres and the hydrophilic matrix, for example, would allow further tailoring of the mechanical response of the hydrogel or provide a latent reservoir for chemical release by taking advantage of the chemical and physical properties of the new polymer block.

Unfortunately, the formation of the sphere morphology in ABC block polymers has been minimally studied.[2,6] This is likely, in part, because of the formidable challenges of dissecting true thermodynamic behavior with the addition of a third unique polymer block, particularly when one block

requires a disproportionate molecular weight in order to achieve the high degree of asymmetry inherent to sphere morphology formation. Such high molecular weights complicate the self-assembly process by adding exponentially increasing chain interactions and entanglements which severely diminish self-assembly kinetics. Predicting and targeting a specific ABC block polymer morphology is challenging because morphological behavior is thermodynamically governed by the volume fractions of two blocks (f_A, f_B), the interaction parameters between all three blocks (χ_{AB}, χ_{AC}, χ_{BC}), and the overall molecular weight of the block polymer(N). Thermodynamic studies of polymer morphology tend to focus on small molecular weight polymers to minimize the kinetic limitations associated with slow chain dynamics. The ABC block polymer sphere morphology is especially complex because it forms in a region of the ABC phase diagram with highly asymmetric polymer block volume fractions. Highly asymmetric systems add challenges because minimizing molecular weight while ensuring adequate phase separation in the minority components becomes impractical in polymer systems without significantly large block incompatibility. While the morphological behavior of more moderate ABC compositions is becoming better understood,[5,10,26,27] the investigations into highly asymmetric systems remained limited, perhaps due to the complex interplay between high molecular weight requirements and the kinetic impact on phase separation. For the polymer systems we are interested in, the high molecular weight component is a major factor further complicated by a minimum molecular weight requirement in the A block component, which for our hydrogel applications requires the vitreous A block to retain a glass transition well above physiological temperatures. As a result, the ABC block polymers of functional interest to our research are therefore often much larger than 100kDa. Morphology studies for most ABC polymers tend to include chains of overall molecular weights nearly half of that if not significantly smaller.[5,28,29] However, even at these smaller molecular weights, minimal increases in size (10kDa) have resulted in a decrease in the ability of the polymers to develop morphologies based on highly periodic lattices.[30]

In AB block polymers, the sphere morphology has experimentally been shown to evolve as spheres composed of the smallest volume fraction polymer block situated either on a thermodynamically favored body-centered cubic (BCC) lattice or be kinetically limited to liquid-like packing (LLP), sitting in

a matrix of the majority volume fraction polymer block. Accordingly, an additional middle block in ABC block polymers, if added as a minority component, results in spheres which are comprised of the two smallest volume fraction blocks of the ABC block polymer chain. These are multicompartment spheres comprised of both A and B domains, for example, instead of the single-compartment spheres associated with AB systems. Computational models predict the ABC spheres to form the shape of a core-shell sphere with the short end block forming spherical cores, surrounded by the middle block shell, situated in a matrix of the largest volume fraction end block.[8] However, based on the specific χ interactions between each block, the middle block can form domains of different shapes on the basic sphere surface, as a way to minimize interfacial contact between adjacent block types with large χ values. Examples of unique sphere configurations include the "spheres-on-spheres" morphology identified by Stadler and coworkers[2] or the planet-like structures reported by Abetz and coworkers.[4] Most of these unique sphere morphologies are the product of thin-film processing or elaborate solvent-casting procedures. The bulk melt assembly of any sphere morphology in ABC block polymers remains minimally investigated if at all. This paper focuses on ABC block polymers' ability to melt assemble into the general sphere morphology and identifying the composition space in the ABC block polymer phase diagram where formation of the sphere morphology can be expected, even if yet to achieve its thermodynamically favored lowest energy state.

Computational phase diagrams predict spheres to form in ABC block polymers when a block polymer has an asymmetrically large volume fraction of a single end block.[8] While an alternating A and C sphere morphology can form when the middle polymer block is largest, our principal focus in this morphological study was constrained to ABC block polymers in which one of the end blocks is the largest block. This sphere forming region the of the phase diagram is computationally predicted to be bounded by a cylindrical phase as the end-block volume fraction is decreased, and a disordered phase as the end-block volume fraction is increased. Cylinder-forming ABC block polymers have been identified and reported,[5] but the experimental determination of where the cylinder phase region ends and the sphere phase region begins remains unexplored.

As stated previously, our study of the sphere-forming region of the ABC block copolymer phase diagram is motivated by the potentially unique and impactful mechanical response associated with adding a new block to our established thermoplastic elastomer hydrogel systems[31,32] based on sphere-forming AB and ABA polymer blends. To this end, the goal was to add a mid-block to the model polystyrene-b-poly(ethylene oxide) (PS-PEO) and polystyrene-b-poly(ethylene oxide)-b-polystyrene (PS-PEO-PS)-based polymer blends previously used in our development of hydrogels capable of mimicking the properties of soft biological tissues such as the fibrocartilage found in the menisci of the knee.[18,25,33] We selected polybutadiene(PB) and polyisoprene(PI) as target middle blocks to be integrated between the PS and the PEO. Such amorphous polydienes were attractive for their intrinsic hydrophobicity and low glass transition temperatures well below room temperature. We hypothesized such properties would the improve energy dissipation capabilities in our highly elastic hydrogels based on PS and PEO.

Thus, the ABC polymers investigated for their morphological behavior in the highly asymmetric composition region of the ternary phase diagram were based on either polystyrene-*b*-polybutadiene-*b*-poly(ethylene oxide) (PS-PB-PEO, SBO) or polystyrene-*b*-polyisoprene-*b*-poly(ethylene oxide) (PS-PI-PEO, SIO). One morphological isopleth of PS-PI-PEO has been studied in the literature, but was not near the computationally predicted sphere region.[26] Chatterjee and Bates compiled known PI-PS-PEO polymers into a phase diagram with a sphere morphology being observed at high temperatures, but returning to a hexagonally-packed cylinder morphology at low temperatures.[5] However, polymers with PEO volume fractions in the range where a sphere morphology was computationally expected were not present in that experimentally investigated phase diagram.

In this study, we present the melt-state phase behavior of 10 ABC block polymers with asymmetrically-large C blocks grown from 5 different AB block polymer macroinitiators as characterized by small-angle X-ray scattering (SAXS) and rheology. The characterization of the polymer phase behavior was used to determine approximate composition boundaries in the phase diagram for the morphologies identified. The impact of polymer molecular weight on the formation and development of morphology in these systems is discussed.

2.3 Results/Discussion

2.3.1 Synthesis and Analysis of Block Polymers:

10 total PS-PI-PEO and PS-PB-PEO ABC triblock polymers were synthesized to investigate sphere morphology formation in highly asymmetric ABC systems (Table 2.1). Macroinitiators of PS-PI-OH and PS-PB-OH were synthesized by anionic polymerization. Polybutadiene was initially used, but the ease of handling liquid monomer and the elimination of special safety considerations associated with purification and use of gaseous monomers made isoprene a more attractive diene for these investigations. Consistent with the polymerization of isoprene and butadiene in cyclohexane at 40°C, 1,4-addition comprised 92% and 91% of the repeat units in the polydiene block in both SIO and SBO polymers respectively. The large presence of the 1,4 isomers in both polymers produces interaction parameters that are similar with respect to PS and PEO; therefore, we chose to include both ABC systems in this study and have included them on the same phase diagram.[28,34–36] The AB macroinitiators were terminated to form a single hydroxide end group, from which the final poly(ethylene oxide) block was added through a second anionic polymerization step. This synthetic strategy involving the initial formation of a separate macroinitiator allowed syntheses of several ABC block polymers with different PEO volume fractions from each single AB macroinitiator synthesized.

Table 2.1: Polymers synthesized by anionic polymerization. S=polystyrene, B=polybutadiene, I=polyisoprene, and O=poly(ethylene oxide). M_n determined by ^{1}H-NMR. Volume fractions calculated from reported polymer densities at 140 ℃.[37]

Polymer	S Mn (g/mol)	B/I Mn (g/mol)	O Mn (g/mol)	Total Mn (g/mol)	f_S	$f_{B/I}$	f_O	Phase
SB-1	10400	8300	0	18700	0.562	0.438	0	Weakly-ordered
SBO-1a	10400	8300	80100	98800	0.111	0.105	0.784	Cylinders
SB-2	12200	5100	0	17300	0.668	0.332	0	*No data*
SBO-2a	12200	4800	102000	119000	0.110	0.051	0.839	Cylinders
SBO-2b	12200	5600	132600	150400	0.087	0.047	0.866	Cylinders
SI-3	8500	6400	0	14900	0.532	0.468	0	*No data*
SIO-3a	8500	6100	39200	53800	0.166	0.139	0.695	HPC
SIO-3b	8500	6300	85100	99900	0.91	0.79	0.829	Cylinders
SI-4	7700	2100	0	9800	0.761	0.239	0	*No data*
SIO-4a	7700	2000	77000	86700	0.096	0.030	0.875	BCC Spheres
SIO-4b	7700	2100	43600	53400	0.153	0.053	0.794	HPC
SI-5	10200	2800	0	13000	0.760	0.241	0	Disordered
SIO-5a	10200	2800	102300	115300	0.096	0.031	0.874	LLP Spheres
SIO-5b	10200	2900	115000	128100	0.086	0.029	0.885	LLP Spheres
SIO-5c	10200	2900	183200	196300	0.057	0.019	0.924	LLP Spheres → Disorder

The monomer weight and polymer density[37] at 140°C was used to calculate and target PS to PI volume fraction ratios of 3:1, 2:1, and 1:1. These volume fractions were targeted because computational phase diagrams developed by Morse and coworkers[8] suggested the potential access to a larger sphere phase composition window with progressively smaller volume fractions of the B block.[8]

The PEO volume fractions in the SIO and SBO systems were chosen to largely mimic the volume fractions of the B block in sphere-forming AB diblock copolymers where f_B is typically 0.87-0.92. Using this volume fraction of PEO in SIO and SBO, two phase-separated morphologies, based on cylinder and sphere minority domains, and a disordered state, were identified. The morphologies of the polymers were determined using a combination of SAXS and rheology. Morphological behavior was investigated from room temperature up to 250°C. The resulting morphologies of each sample are represented in the ABC phase diagram shown in Figure 2.1.

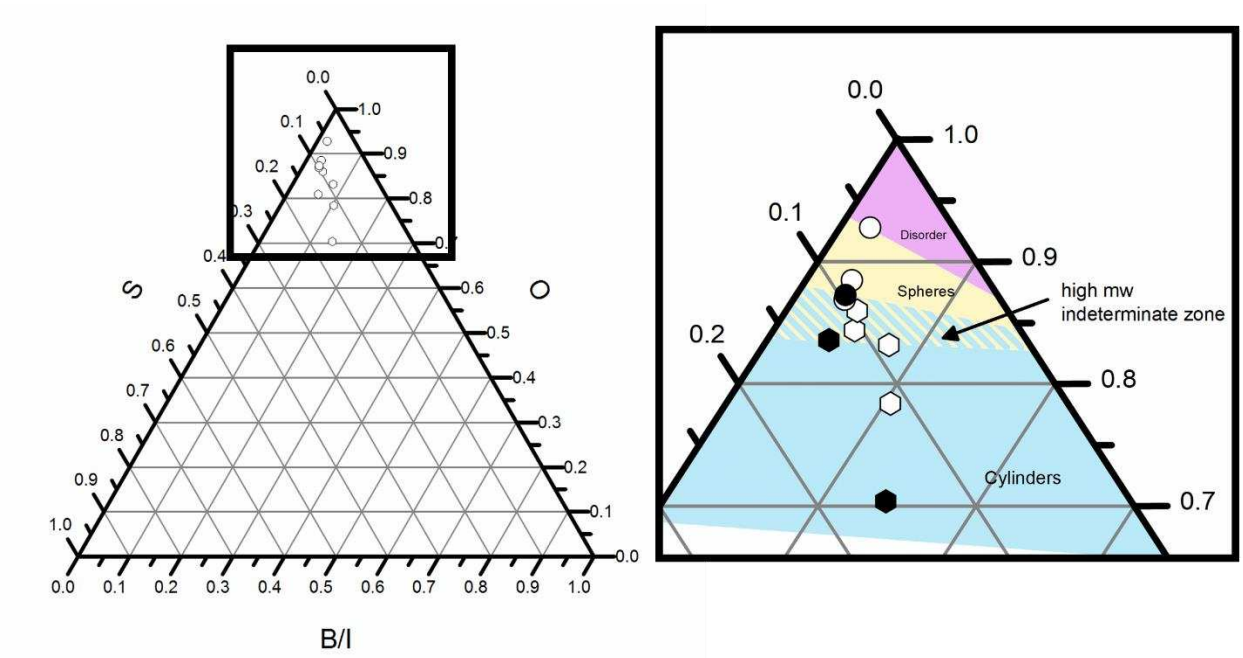

Figure 2.1: Close up SBO/SIO phase diagram showing investigated cylinders, spheres, and disorder regions and a cylinder-sphere high molecular weight indeterminate zone. Full hexagons are SBO and SIO polymers which form hexagonally packed cylinders (HPC). Open hexagons represent SIO and SBO polymers which form liquid-like cylinders. Full circles represent SIO polymers which form the body-centered cubic (BCC) morphology. Open circles represent SIO polymers which form a liquid-like packing of spheres. The dotted lines in the phase regions denote where experimental data is still needed to confirm the phase boundary.

The synthetic challenges that accompany making enough polymers to adequately study the phase region should not be understated. In the highly asymmetric region of the phase diagram, even small changes in majority block volume fraction require large changes in majority block molecular weight. For example, in one sample, a 0.01 increase in PEO volume fraction at the upper end of the expected spheres region corresponds to larger than a 15kDa increase in PEO molecular weight. In fact, exploration of the volume fraction range between 0.87-0.92 required PEO molecular weights spanning 77kDa to 180kDa, depending on the specific molecular weight of the A and B blocks. Achieving these large molecular weights of PEO can present some difficulties when the polymerization is carried out anionically. Despite the generally accepted living character of the polymerization of ethylene oxide by the anionic mechanism, we observed that the required use of extended reaction times to needed to achieve high conversion (reactions left longer than 24 hours) resulted inside reactions with the polyisoprene and polybutadiene blocks of the macroinitiator. In some cases, the use of excess monomer and running reactions to

incomplete conversion of monomer was used to mitigate these effects. While, in theory, the molecular weight of the PS-PI macroinitiator could be decreased to reduce the molecular weight of PEO required, the goal to achieve mechanical function and physical crosslinking through the PS domains in these sphere-forming polymers required a threshold PS block molecular weight greater than about 8 kDa.

Unfortunately, the use of high molecular weight PEO as the majority block in these ABC systems, also driven by our interest in hydrogel applications of these block polymers (PEO is water soluble), presented us with complicating factors when trying to incorporate electron microscopy as a third major characterization tool in this investigation. With a crystallization temperature of approximately 65 ˚C, and sample compositions comprising 70% PEO and greater, we found sectioning thin slices by cryo-ultramicrotome extremely difficult and were never able to achieve TEM images from these slices that provided any conclusive additional characterization insight. This effort was likely equally hampered by the natural distortion of the melt morphology upon crystallization of the PEO. While TEM has been used as a successful tool in the investigation of other PS-PI-PEO samples[26], those studies involved materials in which PEO was often a minority component relative to the PS and PI blocks, and of much smaller molecular weights where the impacts of mass crystallization in one domain is more easily suppressed.

2.3.2 Sphere Formation

Four SIO polymers were characterized as phase separating into a sphere morphology. SIO-4a formed a body-centered cubic (BCC) structure and SIO-5a, 5b, and 5c phase separated into a liquid-like packing of spheres (LLP). The morphology of SIO-4a was determined using SAXS. During a temperature ramp in the SAXS, SIO-4a developed into body-centered cubic spheres following a 140 minute anneal at 250°C as exhibited by the SAXS diffraction pattern with peak position ratios, q_{hkl}/q^*_{100}, of √2, √4, √6, √8, √10, √12 and √14 consistent with the allowed reflections for the Im3(bar)m space group (Figure 2.2a). Before annealing, the principal scattering peak (q*) and two broad higher order peaks with decreasing intensity were visible (Figure 2.2a). After a 2 hour anneal at 250°C, these broad peaks resolved into scattering peaks corresponding to the √4, √6, and √8 reflections expected for the BCC morphology. The

presence of higher-angle scattering beyond the principal scattering reflection both before and after annealing suggests that under both conditions the samples possess order beyond simple phase separation. Traditionally, this behavior in sphere-forming systems is associated with the polymer sample adopting a liquid-like packing in the melt below some critical temperature needed to provide the chain mobility to adopt the thermodynamically favored body-centered cubic lattice (e.g. 250°C, here). Thus, above 250°C we see an increased resolution of the scattering reflections and the emergence of an assignable BCC diffraction pattern, which persists as the sample cools. Synchrotron SAXS of SIO-4a taken at 100°C after annealing at 250°C (Figure 2.3a) is likewise indicative of the periodic BCC lattice with multiple higher-order diffraction peaks consistent with the allowed scattering reflections of the $Im\bar{3}m$ space group. Notably, while the signal to noise ratio associated in the data collected with the synchrotron source is far superior to that collected using our laboratory source (rotating Cu anode), similar degrees of peak broadness in both sets of data suggests these attributes are related to real morphological characteristics that persist after annealing such as interfacial breadth and sphere size polydispersity, rather than simply being a product of limited instrument resolution.

Consistent with this SAXS data, dynamic mechanical spectroscopy (DMS) as a function of temperature indicates the formation of this more-ordered, and presumably triply-periodic BCC structure after heating, with a plateauing of the elastic shear modulus after cooling from 250°C (Figure 2.2b).[38] A frequency sweep (at 150 ˚C after annealing) of SIO-4a shows similar plateauing of the elastic modulus at low frequencies consistent with the observed formation of the triply periodic BCC structure (Figure

2.3b).[38] Both SAXS and rheology thus confirm the formation of the BCC lattice with sufficient heating, and importantly, retention upon cooling.

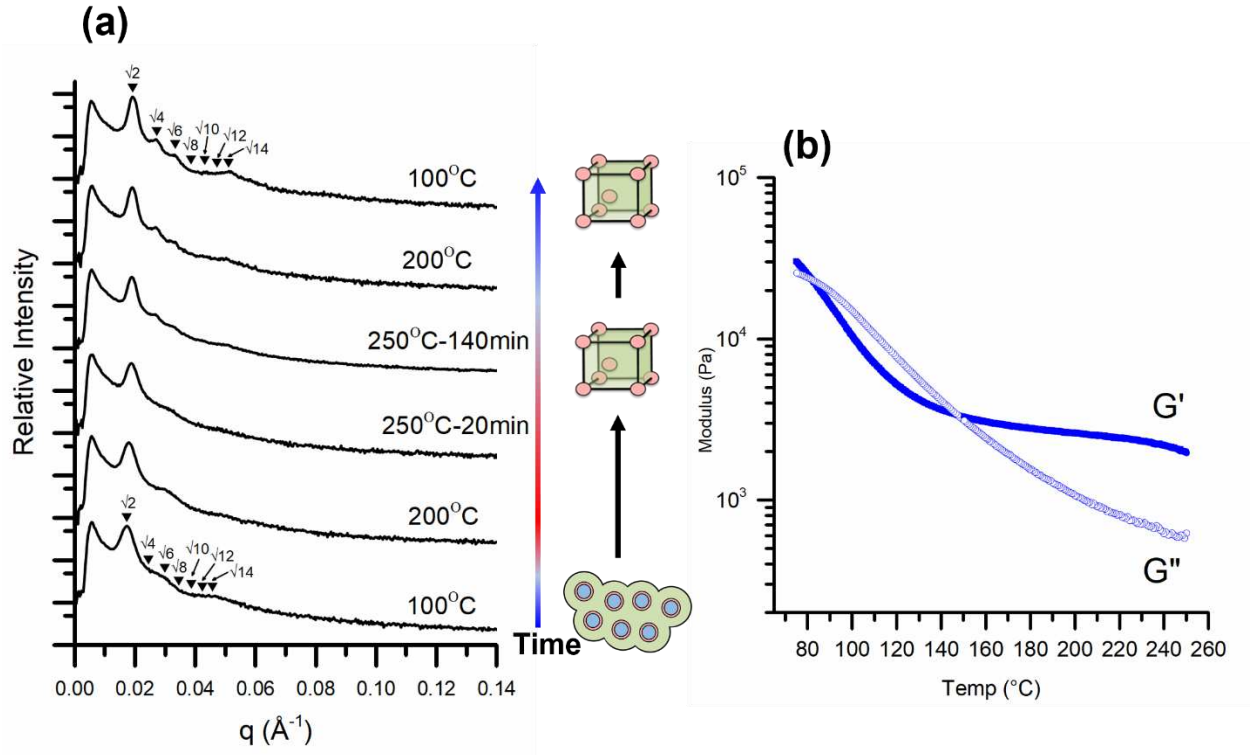

Figure 2.2: (a) SIO-4a SAXS temperature ramp. The polymer first formed a liquid-like packing of spheres and upon annealing ordered into a body-centered cubic structure. The arrows indicate the expected reflections for a BCC morphology calculated from the position of the principal scattering peak in each sample. (b) DMS for SIO-4a shows that after heating the sample to 250°C, both the elastic and loss modulus flatten as the temperature decreases.

SIO-5a, SIO-5b, and SIO-5c were also characterized as forming a sphere morphology but did not ultimately develop a BCC structure under any annealing conditions tested. SIO-5a and SIO-5c are discussed in later sections. SIO-5b had similar scattering profiles to the low temperature SIO-4a SAXS scattering profile (Figure 2.3a). However, annealing at 250°C for 12 hours did not result in the development of more distinct and assignable diffraction peaks. This persistence of the non-diffracting scattering profiles of 5b is similar to the SIO-4a sphere-forming sample before high temperature anneal. The SIO-5b and SIO-4a unannealed scattering profiles both exhibit a broad secondary peak spanning the q region expected for the √4 and √6 positions of the developing BCC lattice of SIO-4a, with 10x smaller scattering intensity than the principal peak. A third broad peak with even smaller scattering intensity

persists in the q region where the √8, √10, √12, and √14 scattering reflections in the SIO-4a sample eventually developed. The presence of the recurring but progressively decaying broad peaks is consistent with the expected form scattering from a collection of packed spheres which lack the periodic order of the BCC structure that developed in the annealed SIO-4a sample. Instead, SIO-5b and the SIO-4a sample before the high temperature anneal persist with this liquid-like packing of spheres similar to what has been observed in multiple AB block polymer systems.[39] DMS of SIO-5b is likewise consistent with the lack of a developed periodic structure as the rheology, unlike in SIO-4a, shows little to no changes between the heating and cooling cycles (Figure S8). Frequency sweep analysis of SIO-5b (Figure 2.3b) does show the similar elastic modulus plateau at low frequencies as seen in the frequency sweep of SIO-4a, a further indicator of the triply periodic nanostructure in these samples irrespective of the degree of longer-range lattice development.

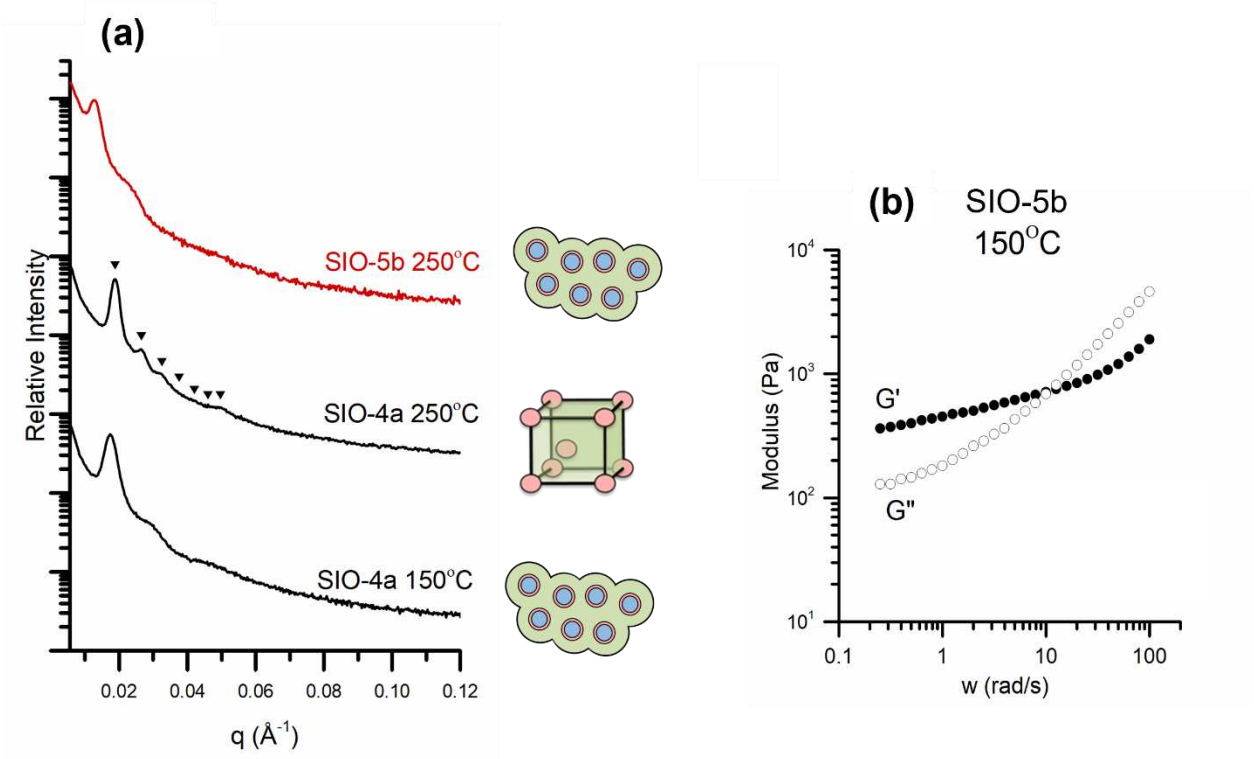

Figure 2.3: (a)SAXS profiles for SIO-4a at 150 ℃ and SIO-4a and 5b annealed to 250 ℃. The red scattering profile is the new sample while the black scattering data is used as a comparison. The arrows indicate the expected reflections for a BCC morphology calculated from the position of the principal scattering peak in each sample. Based on the scattering profiles, only sample SIO-4a achieves the BCC structure after annealing at 250 ℃. The scattering intensity profile for SIO-4a at 150 ℃, before annealing, is also given for comparison, showing consistency with the liquid-like packing of SIO-5b. (b) Frequency sweep for SIO-5b shows a plateauing of the elastic modulus at low frequencies which points to the presence of a triply periodic structure.

Of interest, of course, is being able to define the nature of the PI or PB domain structure at the sphere interface. That is, it would be valuable to understand if the PI or PB domains form continuous shells enveloping the PS spherical cores, or if islands decorating the sphere surface form instead. Interestingly, Morse and coworkers only considered the traditional core shell morphology in their calculations, but justifiably so given they only considered non-frustrated ABC systems.[27] ABC systems in which the block arrangement is chosen so as to place the largest enthalpic penalty for contact between the A and C blocks are considered non-frustrated, in that those blocks are not required to form a high energy interface as a result of being covalently juxtaposed. On the other hand, ABC systems in which the largest enthalpic penalty for contact occurs between the A and B or B and C blocks are intrinsically frustrated because they cannot avoid formation of the highest energy interface. Experimentally, frustrated systems at times have deviated from the traditionally identified block polymer morphological structures by voluntarily introducing the more energetically favorable A/C interface. For example, a "spheres on spheres" morphology, in which islands of PI form on the surface of PS cores was experimentally identified in a system based on PS-PI-PMMA by Stadler and coworkers.[2] In this morphology, the polymer is believed to use PI island formation as a way to reduce PI/PMMA contact by forming a less energetically costly but unforced PS/PMMA interface. Given the similarly frustrated chain architecture in PS-PI-PEO, we acknowledge that there is a considerable possibility of the similar "spheres-on-spheres" behavior in these systems.

Additionally, we posit that if one considers only the domain thickness that would be required for formation of a continuous PI shell about the PS cores in these SIO and SBO samples, that significant circumferential PI chain stretching would be required achieve the necessary PI surface coverage. The total sphere size for the SIO-4a sample as calculated from the principal scattering peak of the SAXS scattering profile which formed the BCC morphology after annealing ($q^*=0.0193Å^{-1}$) would be 11.4nm. The PS core would have a radius of 10.4nm, but due to the large differences in volume fractions between the PS and PI blocks, the PI block would need to have a thickness of 1.0 nm to completely cover the PS core. Island formation not only introduces opportunities to optimize interfacial energy, but simultaneously relieves severe PI chain stretching from being necessary. Of course, this is all in speculation, with conclusive microscopy evidence proving elusive to our efforts.

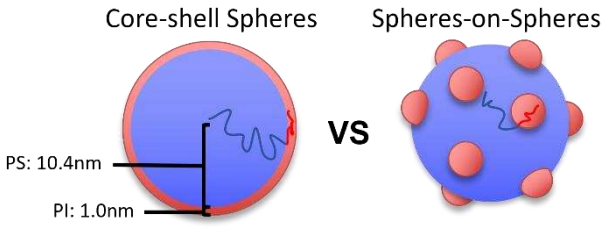

Figure 2.4: Schematic representation of the estimated sizes of the PS and PI domains within a sphere in the SIO-4a samples as calculated from the q(0.019Å^{-1}) of the SAXS scattering profile which formed the BCC morphology after annealing. In the core-shell sphere, the PS core has a radius of 10.4nm. The PI block would need to have a thickness of 1.0nm to completely cover the PS core. Therefore, we suspect the spheres form a spheres-on-spheres morphology to limit the amount of chain stretching in the PI block.*

2.3.3 Cylinder Formation

Two of the polymer samples (SIO-3a and SIO-4b) ordered into hexagonally-packed cylinders (HPC). SAXS and rheological data for SIO-3a shown in Figure 5 is presented as a representative example of the of HPC phase behavior exhibited in these samples. During a temperature ramp performed in situ during SAXS data collection, SIO-3a developed from a liquid like packing of cylinders into hexagonally-packed cylinders following a 60 minute anneal at 250°C as confirmed by a diffraction pattern consistent with domain organization on a hexagonal lattice. These SAXS patterns exhibit peak position ratios,

q_{hkl}/q^*_{100}, of √1, √3, √4, √7, √9, √12 and √13 consistent with those expected for a unit cell of hexagonal symmetry (Figure 2.5a). Before annealing, the scattering profile of SIO-3a (e.g., at 150°C) contains the principal peak (q*) indicating phase separation, a small shoulder on the principal peak, and a broad peak that is 1/3 the principal peak intensity also possessing its own right-side shoulder. Once annealed, the shoulder on the principal scattering peak resolves into the √3 and the √4 reflections, while the largest intensity secondary peak resolves into the √7 and √9 reflections with the √7 peak having the highest intensity, and the final broad shoulder resolves into the expected √12 and √13 reflections. Similar to the formation of BCC spheres after high temperature annealing in SIO-4a, the presence of higher-angle scattering beyond the principal scattering reflection both before and after annealing suggests that under both conditions the samples possess order beyond simple phase separation. In this case, SIO-3a and SIO-4b are initially able to form cylindrical domains in the melt but those domains remain largely disordered, until finally heated above some critical temperature where they are able to adopt the thermodynamically preferred hexagonally-packed lattice (e.g. 250°C, here). Thus, above a threshold temperature or annealing time, we see an increased sharpness in the scattering reflections and the emergence of an assignable HPC diffraction pattern. This change in the structure of the cylinder morphology is also observed using dynamic mechanical spectroscopy (DMS) (Figure 2.5b). The transition to higher elastic and loss moduli through heating from 100°C to 200°C which is maintained upon cooling is reflective of a change of the ordering of the cylindrical domains as detected in the SAXS. A frequency sweep of this sample results in plateauing of the elastic modulus (G') at 150ºC (Figure 2.5c). This is likely associated with cylindrical domain alignment to the reciprocal shear flow direction, acting to further increase the longer-range ordering of the morphology.[40]

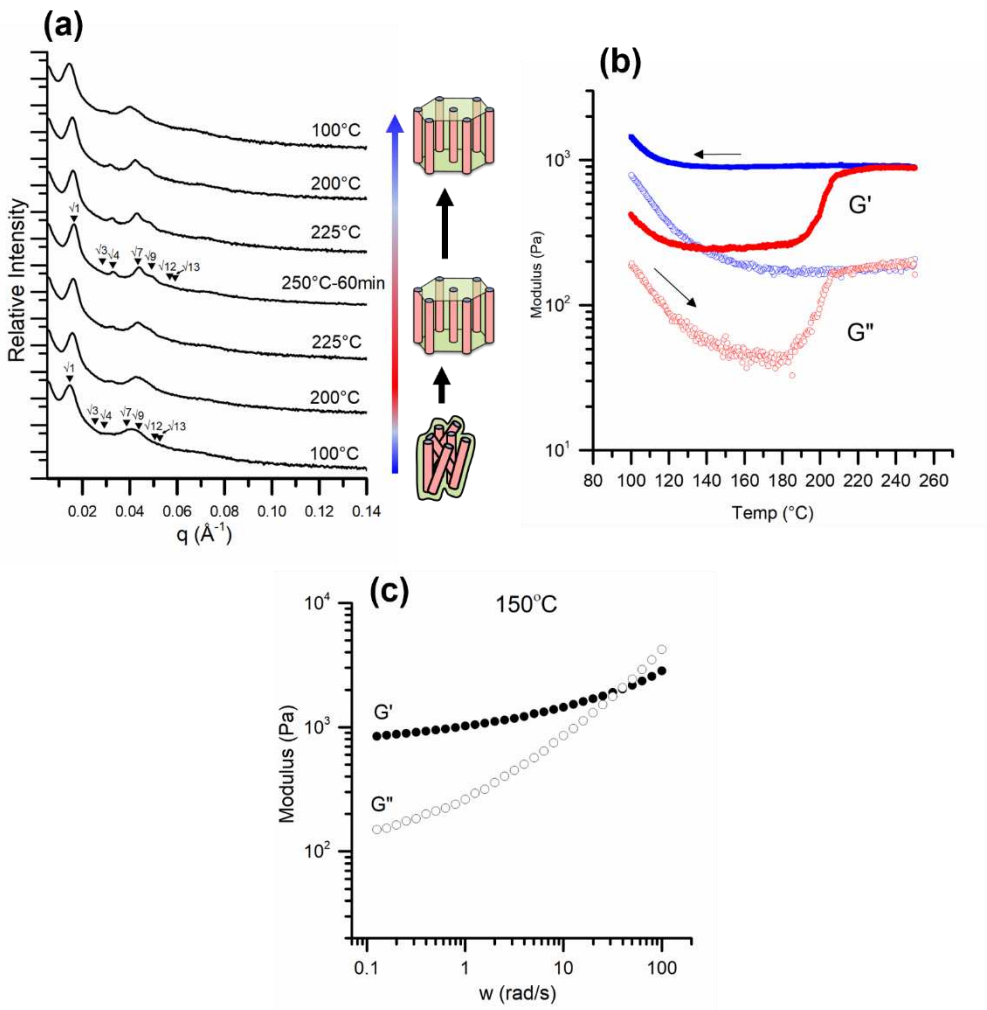

Figure 2.5: (a) SAXS for SIO-3a at 150°C shows the formation of liquid-like cylinders ordering into hexagonally packed cylinders (HPC) upon heating to 250°C. The arrows indicate the expected reflections for a HPC morphology calculated from the position of the principal scattering peak in each sample. The HPC morphology is maintained upon cooling. (b) DMS for SIO-3a from 100°C to 250 °C. Red is the first heating cycle and blue is the subsequent cooling cycle. The rise in both the elastic and loss modulus shows the ordering of the cylinders into the HPC morphology which remains upon cooling (c) Frequency sweep for SIO-3a shows a plateauing of the elastic modulus at low frequencies which points to the presence of ordered cylinders.

Unlike in SIO-3a and SIO-4b, SBO-1a and SIO-3b did not exhibit any development of a well-defined diffraction pattern in their SAXS scattering profile, even after a 12 hour anneal at 250°C. SAXS and rheological data for SBO-1a are shown in detail in Figure 2.6. The assignment of the morphology was done by comparing the SAXS scattering profile to the scattering profile of SIO-3a prior to its development of higher-order diffraction, when its cylindrical domains were still likely characterized by a packing by a disordered or liquid-like structure (Figure 2.6a). Like SIO-3a prior to annealing, the presence of a principal scattering peak and higher-angle scattering in the SAXS scattering profile of SBO-

1a and -3b show that there is phase separation in these samples from the onset, and the remaining higher q form scattering present suggest some non-diffracting but still significant degree of spatial correlation among the domains. Notably, a frequency sweep of SIO-1a (and SIO-3b, data not shown) does not show the plateauing of the elastic modulus at low frequencies observed in LLP sphere-forming samples at moderately high temperatures (e.g., 150°C, Figure 2.6b), a recognized distinguishing characteristic of these two morphological states.[38] In contrast, however, frequency sweeps at high temperatures do show a plateauing of the storage modulus, which is a behavior exhibited at lower temperature by both lower molecular weight HPC samples (SIO-3a, SIO-4b), as well as a LLP sphere-forming sample of similar molecular weight (SIO-5b). Compositionally, SBO-1a falls between the two lower molecular weight HPC forming samples on the phase diagram, but with its much larger molecular weight appears kinetically hampered from ordering. This high molecular weight is likely contributing to the unusual behavior in the frequency sweeps at high temperatures as is discussed in later paragraphs. Despite the plateauing of the elastic modulus at high temperatures, there is no evidence of a shift in morphology shown in the SAXS or the DMS; therefore, we have characterized SBO-1a as forming LLP cylinders.

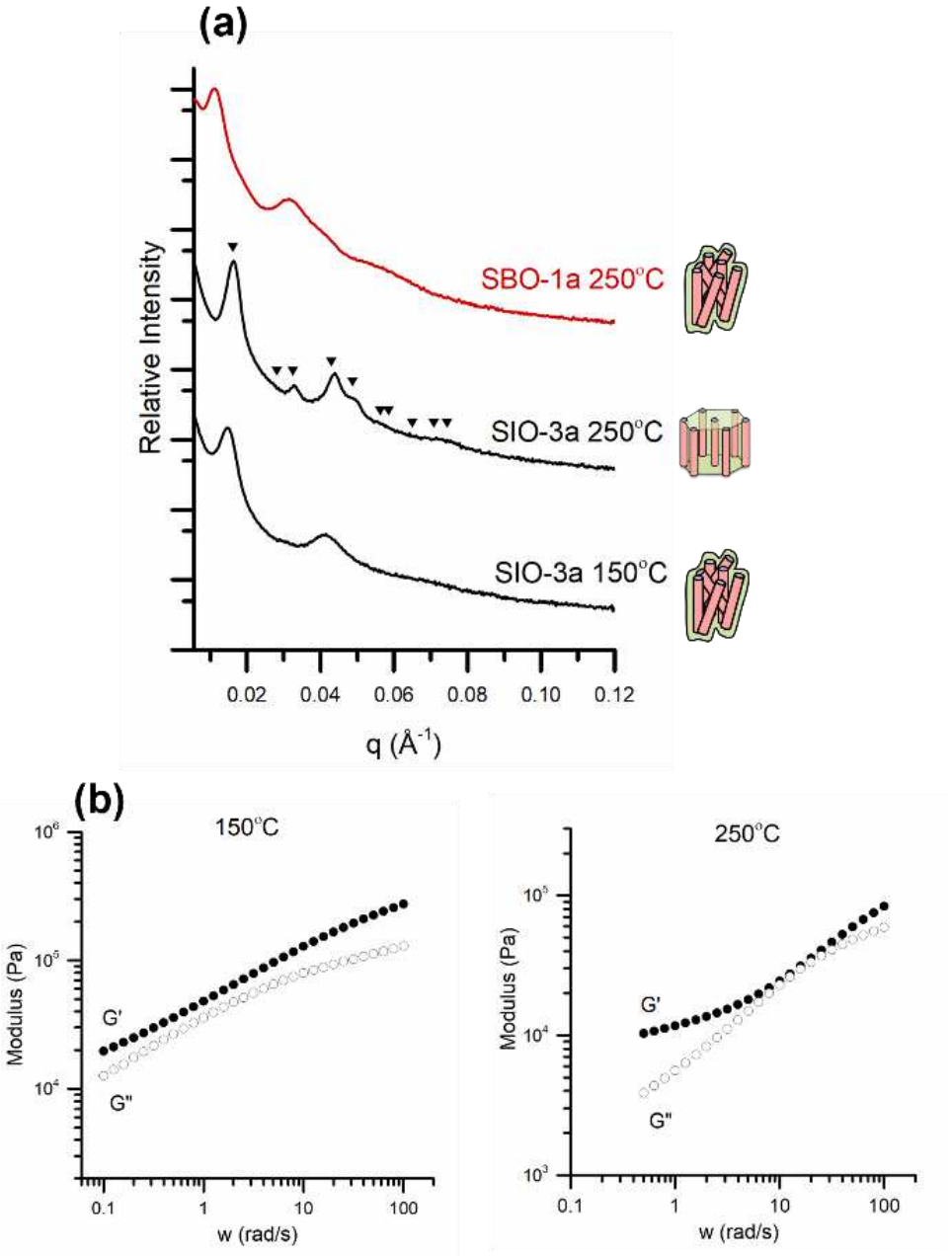

Figure 2.6: a) SAXS of SIO-3a at 150ºC before annealing which forms liquid-like cylinders and SIO-3a and SBO-1a after annealing at 250ºC. The red scattering profile is the new sample while the black scattering data is used as a comparison. The arrows indicate the expected reflections for a HPC morphology calculated from the position of the principal scattering peak in each sample. SBO-1a has a similar scattering profile to SIO-3a before annealing which shows that it is forming liquid-like cylinders. b) Frequency sweeps for SBO-1a at 150°C and 250C show that plateauing of the elastic modulus only occurs at high temperatures unlike in sphere-forming samples.

2.3.4 High Molecular Weight Indeterminate Zone at the Sphere-Cylinder Boundary

In our attempt to help define what a portion of the experimental ABC phase diagram for SBO and SIO polymers in this asymmetric region might look like, we could use the definitive assignments of SIO-4a and SIO-4b together with the computational trends identified by Morse and Coworkers[8] to help place bounds associated with sphere or cylinder morphology formation. However, for samples that both fall between these bounds, and for which self-assembly appears kinetically limited by its high molecular weight to liquid like packing, differentiating between a sphere-forming and cylinder-forming polymers given the difficulties associated with ultramicrotomography necessary for electron microscopy is quite challenging. As mentioned previously, the boundaries of this region, in general, have not been extensively studied experimentally, even with smaller molecular weight analogs of the larger ABC polymers of interest to us. While cylinder morphologies have been observed, and computational studies of block polymers with asymmetrically large A or C blocks have shown evidence of sphere morphology formation, in-depth evaluation of the compositional boundary thermodynamically defining the transition between these phases has been largely overlooked.[8,9,41]

SBO-2a, SBO-2b, and SIO-5a fall into this "high molecular weight indeterminant zone" which falls between the clear cylinder and sphere phase boundaries placed in Figure 1. This is termed the high molecular weight indeterminant zone because all samples have significantly larger molecular weights than the lattice-forming structures of SIO-4a and SIO-4b. SAXS data for SBO-2a, SBO-2b, and SIO-5a remain consistent with a liquid-like packing morphology even when heated to 250ºC. SAXS data for SBO-2a, SBO-2b, and SIO-5a at 100ºC all exhibit higher order scattering suggesting the presence of domain correlation beyond simple phase separation within the sample, but not with any periodic consistency that would produce a diffraction condition in the SAXS data (Figure 2.7). When comparing the SAXS data for SBO-2a, SBO-2b, and SIO-5a at 100ºC, the samples have very similar scattering profiles. However, when the samples are heated to 250ºC in situ while SAXS data is collected, SBO-2a and SBO-2b begin to more closely resemble the scattering profile produced by the liquid-like packing of cylinders formed by SBO-1a, while the SAXS data for SIO-5a resembles the scattering profile produced

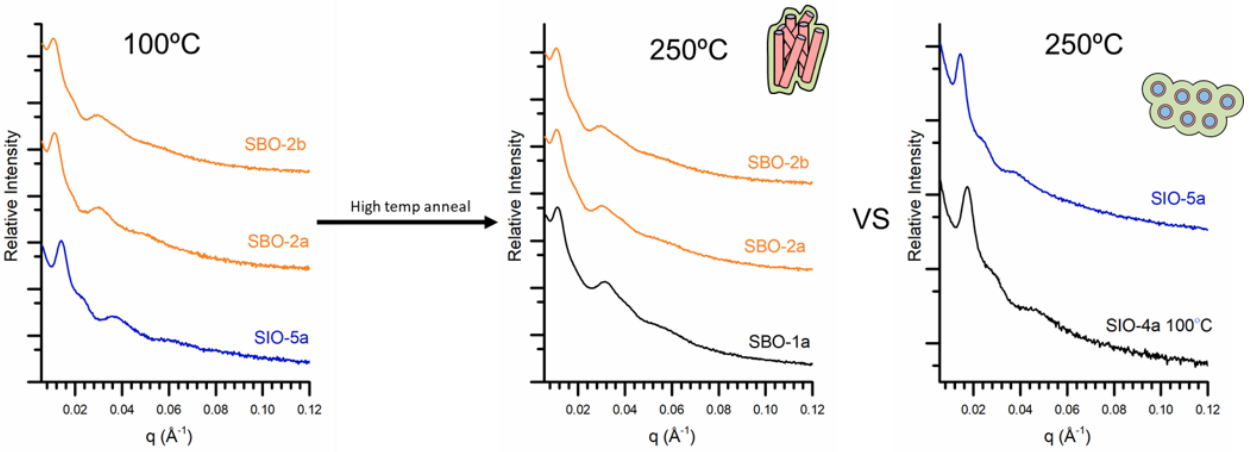

Figure 2.7: SAXS scattering for the samples in the sphere-cylinder high molecular weight transition region—SBO-2a (orange), SBO-2b (orange), and SIO-5a (blue)—before annealing (100ºC) and after high temperature annealing (250ºC). The black scattering data is used as a comparison. While the samples look similar before annealing, they can only be identified as forming a liquid-like morphology. However, after annealing, SBO-2a and SBO-2b have similar SAXS scattering profiles to SBO-1a which forms liquid-like cylinders and SIO-5a has a similar scattering profile to SIO-4a before it was annealed which formed liquid-like spheres.

by the liquid-like packing of spheres formed by SIO-4a (prior to annealing). Despite these subtle changes in the SAXS profiles, DMS data for these samples does not show significant changes in the moduli characteristic of traditional order-order transitions between two developed morphologies.[42]

The differences between SIO-5a and SBO-2a and SBO-2b are even more apparent from frequency sweeps where the elastic modulus for SIO-5a plateaus at 150 ˚C similar to the sphere-forming samples of SIO-4a and SIO-5b (Figure 2.8). However, the elastic modulus for SBO-2a and SBO-2b only plateau at higher temperatures, similar to SBO-1a which forms liquid-like cylinders. It has been previously shown that connectivity of the domain structure affects the rheological response of a block polymer.[38,42] Therefore, the plateauing of the elastic modulus SIO-5a and SIO-5b at lower temperatures is likely caused by sphere domains which possess both greater local translational mobility and triply-continuous periodicity, and therefore are more prone to producing the elastic response to oscillatory shear, even at lower temperatures. The frequency sweep behavior of SBO-1a, SBO-2a, and SBO-2b, conversely, is not necessarily what would be expected of HPC samples, but also is not typical of sphere-forming samples either. This behavior is likely not simply an effect of molecular weight difference, as SIO-5a and

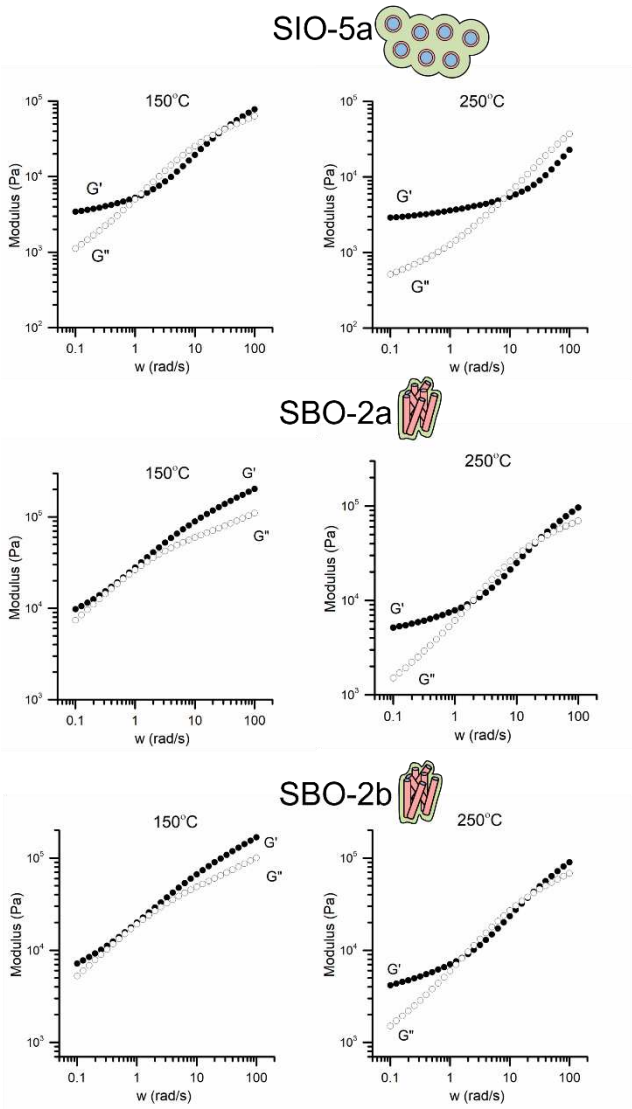

Figure 2.8: Frequency sweep for SIO-5a shows that it plateaus at 150ºC similar to other sphere-forming samples and maintains this plateau when frequency sweeps are performed at 250 ºC. Frequency sweeps for SBO-2a and SBO-2b show that they only plateau at high temperatures which is similar to other samples which formed liquid-like cylinders.

SBO-2a share larger, similar molecular weights in comparison with a smaller SBO-1a (Table 2.1). With all of these attributes of behavior taken collectively, we tentatively characterized SBO-2a and 2b as forming liquid-like cylinders and SIO-5a as forming liquid-like spheres, while acknowledging that the larger molecular weights of the samples ultimately make conclusive characterization uncertain, if not inappropriate in terms of suggesting absolute thermodynamic or equilibrium behavior. However, we also recognize that, given our interest in what morphologies one can experimentally access, and if hydrogel

design, in particular, can be predicated on access to sphere-based morphology in this region, these investigations helping to define morphological development in the context of slowed self-assembly kinetics have tremendous practical value.

In this light, rather than placing the SBO-2a, SBO-2b, and SIO-5a samples directly into the sphere or cylinder bounded regions, we acknowledge the unique impact that high molecular weight has in identifying the equilibrium morphology and define this region as the indeterminant zone at the sphere-cylinder boundary. In total, only three samples in these studies, SIO-4a, SIO-3a, and SIO-4b, produced SAXS data with assignable higher-order diffraction peaks upon annealing at elevated temperatures, while the remaining SBO and SIO samples produced SAXS data with features consistent with the form-scattering of liquid-like packing even after extended 12-hour anneals. Whether each sample ultimately developed into its thermodynamically preferred ordered morphology or remains kinetically trapped with its domains in a liquid-like state of disorder, appears to be strongly rooted in the total molecular weight of the block polymer. The samples that developed ordered lattices of spheres or cylinders were the lowest molecular weight samples investigated (Table 2.1). The kinetics of morphology formation in linear polymer chains are well known to depend on molecular weight because chain dynamics become more and more inhibited with increasing entanglements per chain. Coupled with the enthalpic barriers associated with dissimilar block contact or block diffusion through dissimilar polymer domains, these entanglements severely impeded chain exchange between the developing sphere or cylinder domains. Continual chain exchange facilitates the formation of uniformly distributed domain sizes necessary for highly-ordered lattice development. The slowing of chain exchange, therefore, results in a broad distribution of domain sizes that promote liquid-like disorder, and limit domain organization necessary to achieve a diffraction condition. Unfortunately, the large asymmetry in composition needed to produce the morphologies of interest in this study require minimum molecular weights requiring impractically long thermal anneal times if high levels of order are desired. Solvent annealing may provide an alternative but is notorious for producing non-thermodynamically-favored morphologies with even small degrees of block selectivity. As mentioned at the outset, electron microscopy would provide an invaluable tool with respect to allowing us

to identify sphere or cylinder domain structures more definitively in these samples; however, we have found the high PEO content and the complications associated with its crystallization (both in terms of sample preparation and distortion of the morphology during the molecularly violent crystallization event) unsuccessful. And while the sum of these complications makes identification challenging, the combination of unique form-scattering and rheological behavior have proven helpful in distinguishing domain structure even when the liquid-like disorder persists.

2.3.5 Sphere-Disorder Phase Boundary

One sample, SIO-5c, was characterized as sphere-forming at low temperatures and then showing characteristics of disordering as the temperature was increased. Between 150°C and 200°C, SIO-5c exhibits a SAXS scattering profile similar to the LLP spheres shown by SIO-5a and SIO-5b. Uniquely however, a decrease of intensity and significant broadening in the SAXS principal scattering peak began as the temperature was increased further. While higher-angle form scattering still suggests the preceense of sphere domains, the sample seems to be detectably moving towards disorder at temperatures above 200°C (Figure 2.9a). This is corroborated by DMS which shows a loss of modulus during the heating cycle with the sample starting to quickly lose both elastic and loss modulus above 200°C (Figure 2.9b). Frequency sweeps of SIO-5c show the significant decrease in elastic modulus at low frequencies consistent with a less-ordered structure despite SAXS showing the presence of some continued phase separation (Figure 2.9c). This type of behavior, including the persistence of spherical domains well above expected disorder temperatures has been characterized previously in AB systems.[43]Therefore, we suspect the SIO-5c sample, with the largest PEO volume fraction of any sample in the study, is likely sitting on or adjacent to the boundary between the sphere phase region and disorder. Notably, none of the SIO or SBO polymers exhibited sufficient decreases in modulus during rheological measurements to suggest a full or complete transition to disorder, even above 300°C.

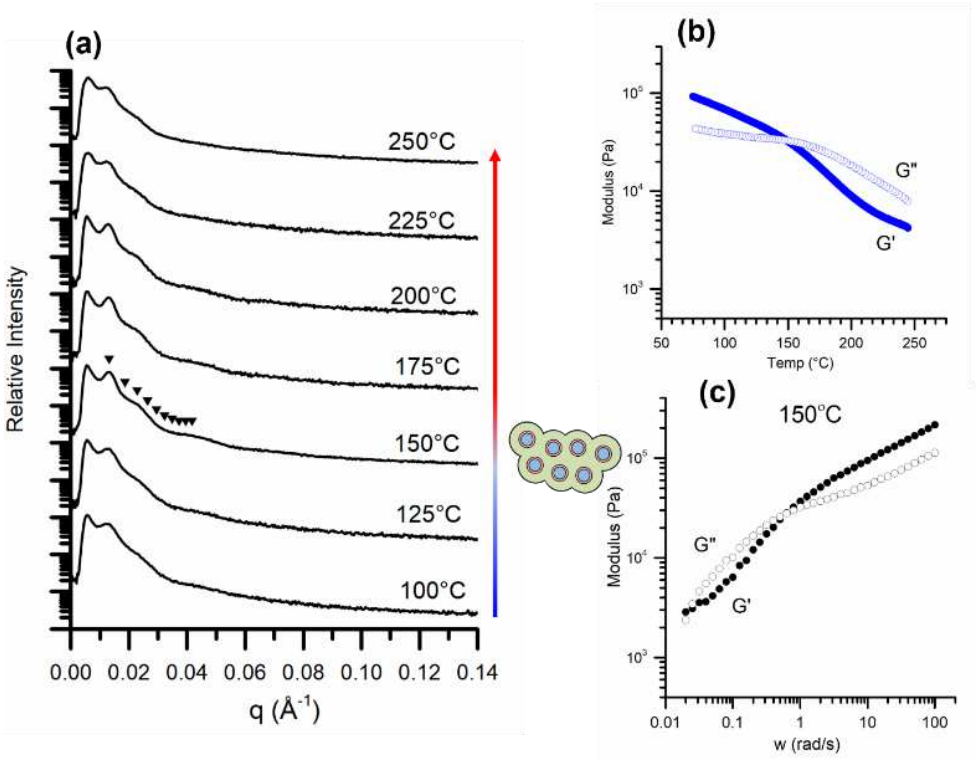

Figure 2.9:(a) SAXS scattering profiles of SIO-5c from 100°C to 250°C shows the formation of LLP spheres at 150°C and the disordering of the spheres above 200°C. The arrows indicate the expected reflections for a BCC morphology calculated from the position of the principal scattering peak in each sample. (b) DMS of SIO-5c shows the polymer's modulus start to decrease at 200°C. (c) Frequency sweeps of SIO-5c shows the decrease in modulus at low frequencies that is consistent with a less-ordered morphology

2.4 Conclusion

This chapter focuses on ABC block copolymers with molecular weights larger than 100kDa that were synthesized to target the sphere region of the ABC phase diagram, using asymmetrically large volume fractions of the C block to achieve the necessary interfacial curvature to favor sphere domain formation. Minority component A to B block volume fraction ratios of 3:1, 2:1, and 1:1 were investigated. We believe this is the first time the melt-assembly of the ABC sphere morphology and its potential phase boundaries have been experimentally investigated, particularly with polymer systems that contain an asymmetrically large volume fraction of the C block. PS-PI-PEO and PS-PB-PEO polymers were synthesized by anionic polymerization, processed by melt-pressing, and characterized by SAXS and

rheology to determine morphological behavior. Body-centered cubic spheres were observed when the PEO volume fraction was greater than 0.87 and total polymer molecular weight was less than 90kDa. Hexagonally-packed cylinders were observed when the PEO volume fraction was less than 0.87 and total polymer molecular weight was less than 55kDa. A liquid-like packing of cylinders was observed when the PEO volume fraction was less than 0.80 and total polymer molecular weight was greater than 55kDa. A liquid-like packing of spheres was observed when the PEO volume fraction was greater than 0.875 and total polymer molecular weight was greater than 90kDa. There was a high molecular weight indeterminant zone between the sphere and cylinder phase regions at PEO volume fractions between 0.80 and 0.875, within which determination of the differences between a polymer forming a liquid-like packing of spheres or a liquid-like of cylinders was not straightforward when the polymer molecular weights were above 100kDa. The onset of disordering was observed to occur when the volume fraction of PEO was larger than 0.93. Large polymer molecular weights were shown to inhibit the development of periodic, lattice level order during melt assembly.

2.5 Experimental

2.5.1 Materials

Styrene (99.5% for analysis, stabilized, Acros) and ethylene oxide (99.5%, compressed gas, Aldrich) were purified by vacuum distillation from dried dibutylmagnesium (1.0M solution in heptane, Aldrich). 1,3-Butadiene (99+%, p-tert-butylcatechol inhibitor, Aldrich) and Isoprene (99%, p-tert-butylcatechol inhibitor, Aldrich) were purified by vacuum distillation from n-butyl lithium (1.6M solution in hexane). Argon degassed cyclohexane (CHX) was purified by passing the solvent over activated alumina followed by Q-5-like supported copper catalyst (Glass Contour). Argon-degassed tetrahydrofuran (THF) was purified by passing the solvent over activated alumina. High-purity argon (99.998%, Airgas) was passed through additional oxygen and moisture traps prior to use. All chemical syntheses were carried out in a dry argon atmosphere using standard Schlenk line techniques.

2.5.2 Methods

Anionic Polymerization of PS-PB-OH and PS-PI-OH

Purified styrene monomer was added under argon to a stirring solution of sec-butyl lithium (1.3M solution in cyclohexane/hexane(92/8), Acros) and dry, air-free cyclohexane in a 1 L reaction vessel at 40°C. Stirring continued for approximately 8 hours. The reactor pressure was then reduced to approximately 1 psig. Purified diene (isoprene or 1,3 butadiene gas) was added to the reaction vessel slowly to ensure pressure did not rise above 10psig. The reaction was maintained at 40°C for 8 hours. At this time, purified ethylene oxide was added to the reactor and allowed to react for 24 hours. The reaction was terminated by direct addition of sparged acidic methanol. The polymer was rotovapped and precipitated in a 1:4 mixture of isopropanol and methanol (2 L total) to give a white solid. The polymer was dried under vacuum at room temperature for 48 hours. Because the PS-PI-OH and PS-PB-OH polymers were synthesized in cyclohexane, the resulting isomer ratios average 92% 1,4-PS-PI and 8% 3,4-PS-PI and 91% 1,4-PS-PB and 9% 1,2-PS-PB.

Anionic Polymerization of PS-PB-PEO and PS-PI-PEO

PS-PB-OH or PS-PI-OH (1g) was dried overnight under vacuum in a 2L reaction vessel with a glass stirbar. The reactor was evacuated and backfilled with purified argon before the addition of approximately 1L of dry, air-free THF. Concentrated potassium naphthalenide in dry, air-free THF was added to the polymer solution via cannula until a light green color persisted for at least 15 minutes. The temperature of the reaction mixture was raised to 40°C. A 1.5 molar excess of purified ethylene oxide was added under argon with vigorous stirring. Stirring was continued for no more than 24 hours. The reaction was terminated by direct addition of 0.1M hydrochloric acid in methanol. The polymer was rotovapped and precipitated into pentane to give a light purple solid of PS-PB-PEO or a light yellow solid of PS-PI-PEO. The polymer was dried under vacuum at room temperature for 48 hours.

NMR and GPC

Size exclusion chromatography (SEC) was performed on a Viscotek GPC-Max chromatography system fitted with three 7.5 340 mm PolyporeTM (Polymer Laboratories) columns in series, an Alltech external column oven, and a Viscotek differential refractive index (RI) detector. PS molecular weight and dispersity, and dispersity of the PS-PB, PS-PI, PS-PI-PEO, and PS-PB-PEO samples were determined using a THF (40°C) mobile phase (1 mL/min) with PS standards (Polymer Laboratories) at 2mg/mL concentration. 1H-NMR spectra were collected at room temperature in $CDCl_3$ on a Bruker NEO400 MHz spectrometer with ProdigyTM BBFO Probe (n = 128, delay = 10 sec, acquisition time = 2.5 sec).

Small Angle X-ray Scattering (SAXS)

SAXS data were collected on a Rigaku S-Max 3000 High Brilliance 3 Pinhole SAXS system outfitted with a MicroMax-007HFM Rotating Anode (CuKa), Confocal Max-FluxTM Optic, Gabriel Multiwire Area Detector and a Linkam thermal stage. Samples were subjected to a heating cycle from 100°C to 250°C and annealed for 1 hour with 10min acquisition times every 50°C. If no changes in the scattering profile were observed, the sample was allowed to continue annealing for up to 12 hours. The sample was then cooled back to 100°C with 10min acquisition times every 50°C. The crystallization of PEO below 70°C disrupts the polymer morphology, so it is not useful to characterize the polymers below 75°C.

Synchrotron SAXS

Synchrotron SAXS data were collected at the Advanced Photon Source at Argonne National Laboratory using the 12-ID-B beamline with $\lambda = 0.886$ Å wavelength X-rays. The sample-to-detector distance was 3.6m, and data was acquired with a Pilatus 2M detector. Samples were subjected to a heating cycle from 100°C to 200°C and annealed for 1 hour every 50°C. The sample was then cooled back to 100°C with 10min acquisition times every 50°C.

Polymer processing for SAXS

Polymer was placed into an 8mm x 1mm round mold between two pieces of Teflon coated Kapton sheets. The discs were then held (Carver Press) under a constant pressure at 150°C for approximately 10 minutes until no bubbles could be seen in the polymer melt.

Polymer processing for rheology

Polymer was placed into an 25mm x 1mm round mold between two pieces of Teflon coated Kapton sheets. The discs were then held under a constant pressure on a Carver Press at 150°C for approximately 10 minutes until no bubbles could be seen in the polymer melt.

Rheology

Rheological tests were performed on a TA Instruments ARES rheometer with 25 mm parallel plates. Dynamic mechanical spectroscopy was performed for each sample using a 1-3.5% shear strain (verified linear viscoelastic region) and with 1% frequency from 100°C to 250°C with two heating and one cooling cycle at 1°C/sec. Dynamic frequency sweeps (oscillatory shear) were performed for each sample using a 1–3.5% shear strain (verified linear viscoelastic region) over a frequency range of 0.1 to 100 rad/s.

2.6 References:

1. Epps, T. H. *et al.* Ordered Network Phases in Linear Poly(isoprene-b-styrene-b-ethylene oxide) Triblock Copolymers. *Macromolecules* **37**, 8325–8341 (2004).

2. Breiner, U., Krappe, U., Jakob, T., Abetz, V. & Stadler, R. Spheres on spheres - A novel spherical multiphase morphology in polystyrene-block-polybutadiene-block-poly(methyl methacrylate) triblock copolymers. *Polym. Bull.* **40**, 219–226 (1998).

3. Stadler, R. *et al.* Morphology and Thermodynamics of Symmetric Poly(A-block-B-block-C) Triblock Copolymers. *Macromolecules* **28**, 3080–3091 (1996).

4. Gil Haenelt, T., Meyer, A., Abetz, C. & Abetz, V. Planet-Like Nanostructures Formed by an ABC Triblock Terpolymer. *Macromol. Chem. Phys.* **220**, (2019).

5. Chatterjee, J., Jain, S. & Bates, F. S. Comprehensive phase behavior of poly(isoprene-b-styrene-b-ethylene oxide) triblock copolymers. *Macromolecules* **40**, 2882–2896 (2007).

6. Mogi, Y. *et al.* Superlattice Structures in Morphologies of the ABC Triblock Copolymers. *Macromolecules* **27**, 6755–6760 (1994).

7. Mogi, Y. *et al.* Preparation and Morphology of Triblock Copolymers of the ABC Type. *Macromolecules* **25**, 5408–5411 (1992).

8. Tyler, C. A., Qin, J., Bates, F. S. & Morse, D. C. SCFT study of nonfrustrated ABC triblock copolymer melts. *Macromolecules* **40**, 4654–4668 (2007).

9. González-Pizarro, D. A., Soto-Figueroa, C., Rodríguez-Hidalgo, M. D. R. & Vicente, L. Mesoscopic study of the ternary phase diagram of the PS-PB-P: T BMA triblock copolymer: Modification of the phase structure by the composition effect. *Soft Matter* **14**, 508–520 (2018).

10. Bailey, T. S., Hardy, C. M., Epps, T. H. & Bates, F. S. A noncubic triply periodic network morphology in poly(isoprene-b-styrene-b-ethylene oxide) triblock copolymers. *Macromolecules* **35**, 7007–7017 (2002).

11. Radlauer, M. R. *et al.* Morphological consequences of frustration in ABC triblock polymers. *Macromolecules* **50**, 446–458 (2017).

12. Hückstädt, H., Göpfert, A. & Abetz, V. Influence of the block sequence on the morphological behavior of ABC triblock copolymers. *Polymer* **41**, 9089–9094 (2000).

13. Rueschhoff, L. M. *et al.* Fabricating Ceramic Nanostructures with Ductile-like Compression Behavior via Rapid Self-Assembly of Block Copolymer and Preceramic Polymer Blends. *ACS Appl. Nano Mater.* **2**, 250–257 (2019).

14. Tamate, R. *et al.* Photo/thermoresponsive ABC triblock copolymer-based ion gels: photoinduced structural transitions †. *Soft Matter* **14**, 9088 (2018).

15. Liu, S., Yang, Y., Zhang, L., Xu, J. & Zhu, J. Recent progress in responsive photonic crystals of block copolymers. *Journal of Materials Chemistry C* **8**, 16633–16647 (2020).

16. Pitto-Barry, A. & Barry, N. P. E. Pluronic® block-copolymers in medicine: From chemical and biological versatility to rationalisation and clinical advances. *Polym. Chem.* **5**, 3291–3297 (2014).

17. Schacher, F. H., Rupar, P. A. & Manners, I. Functional block copolymers: Nanostructured materials with emerging applications. *Angewandte Chemie - International Edition* **51**, 7898–7921

(2012).

18. Lewis, J. T., Fischenich, K. M., Haut Donahue, T. L. & Bailey, T. S. Nanostructure-Driven Replication of Soft Tissue Biomechanics in a Thermoplastic Elastomer Hydrogel. *ACS Biomater. Sci. Eng.* **4**, 3854–3863 (2018).

19. Gupta, M. K. *et al.* Cell Protective, ABC Triblock Polymer-Based Thermoresponsive Hydrogels with ROS-Triggered Degradation and Drug Release. *J. Am. Chem. Soc* **136**, 14896–14902 (2014).

20. Onoda, M. *et al.* Precisely Tunable Sol-Gel Transition Temperature by Blending Thermoresponsive ABC Triblock Terpolymers. *ACS Macro Lett.* **7**, 950–955 (2018).

21. Fink, Y., Urbas, A. M., Bawendi, M. G., Joannopoulos, J. D. & Thomas, E. L. Block copolymers as photonic bandgap materials. *J. Light. Technol.* **17**, 1963–1969 (1999).

22. Kang, Y., Walish, J. J., Gorishnyy, T. & Thomas, E. L. Broad-wavelength-range chemically tunable block-copolymer photonic gels. *Nature Materials* **6**, 957–960 (2007).

23. Henderson, K. J., Zhou, T. C., Otim, K. J. & Shull, K. R. Ionically cross-linked triblock copolymer hydrogels with high strength. *Macromolecules* **43**, 6193–6201 (2010).

24. Sugiyama, F. *et al.* Stretchable and Degradable Semiconducting Block Copolymers. *Macromolecules* **51**, 5944–5949 (2018).

25. Guo, C. & Bailey, T. S. Highly distensible nanostructured elastic hydrogels from AB diblock and ABA triblock copolymer melt blends. *Soft Matter* **6**, 4807 (2010).

26. Bailey, T. S., Pham, H. D. & Bates, F. S. Morphological behavior bridging the symmetric AB and ABC states in the poly(styrene-b-isoprene-b-ethylene oxide) triblock copolymer system. *Macromolecules* **34**, 6994–7008 (2001).

27. Bailey, T. S. Morphological Behavior Spanning the Symmetric AB and ABC Block Copolymer States. (2001).

28. Qiao, Y. *et al.* Symmetric Poly(ethylene oxide- b -styrene- b -isoprene) Triblock Copolymers: Synthesis, Characterization, and Self-Assembly in Bulk and Thin Film. *Macromolecules* **47**, 6373–6381 (2014).

29. Tang, C. *et al.* Square packing and structural arrangement of ABC triblock copolymer spheres in thin films. *Macromolecules* **41**, 4328–4339 (2008).

30. Meuler, A. J., Hillmyer, M. A. & Bates, F. S. Ordered network mesostructures in block polymer materials. *Macromolecules* **42**, 7221–7250 (2009).

31. Huq, N. A., Ekblad, J. R., Leonard, A. T., Scalfani, V. F. & Bailey, T. S. Phototunable Thermoplastic Elastomer Hydrogel Networks. *Macromolecules* **50**, 1331–1341 (2017).

32. Scalfani, V. F. & Bailey, T. S. Access to nanostructured hydrogel networks through photocured body-centered cubic block copolymer melts. *Macromolecules* **44**, 6557–6567 (2011).

33. Fischenich, K. M., Lewis, J. T., Bailey, T. S. & Haut Donahue, T. L. Mechanical viability of a thermoplastic elastomer hydrogel as a soft tissue replacement material. *J. Mech. Behav. Biomed. Mater.* **79**, 341–347 (2018).

34. Löbling, T. I. *et al.* Bulk morphologies of polystyrene-block-polybutadiene-block-poly(tert-butyl methacrylate) triblock terpolymers. *Polymer* **72**, 479–489 (2015).

35. Neumann, C., Abetz, V. & Stadler, R. Phase behavior of ABC-triblock copolymers with two inherently miscible blocks. *Colloid Polym. Sci.* **276**, 19–27 (1998).

36. Avgeropoulos, A., Paraskeva, S., Hadjichristidis, N. & Thomas, E. L. Synthesis and microphase separation of linear triblock terpolymers of polystyrene, high 1,4-polybutadiene, and high 3,4-polyisoprene. *Macromolecules* **35**, 4030–4035 (2002).

37. Fetters, L. J., Lohse, D. J., Richter, D., Witten, T. A. & Zirkel, A. Connection between Polymer Molecular Weight, Density, Chain Dimensions, and Melt Viscoelastic Properties. *Macromolecules* **27,** 4639–4647 (1994).

38. Kossuth, M.B., Morse, D.C., Bates, F. S. Viscoelastic behavior of cubic phases in block copolymer melts. *J. Rheol. (N. Y. N. Y).* **43**, 167–194 (1999).

39. Kim, J. K. & Han, C. D. Phase Behavior and Phase Transitions in AB- and ABA-type Microphase-Separated Block Copolymers. *Adv. Polym. Sci.* **231**, 77–145 (2009).

40. Ryu, C. Y., Lee, M. S., Hajduk, D. A. & Lodge, T. P. Structure and viscoelasticity of matched asymmetric diblock and triblock copolymers in the cylinder and sphere microstructures. *J. Polym. Sci. Part B Polym. Phys.* **35**, 2811–2823 (1997).

41. Qin, J., Bates, F. S. & Morse, D. C. Phase behavior of nonfrustrated ABC triblock copolymers: Weak and intermediate segregation. *Macromolecules* **43**, 5128–5136 (2010).

42. Ryu, C. Y. & Lodge, T. P. Thermodynamic stability and anisotropie fluctuations in the cylinder-to-sphere transition of a block copolymer. *Macromolecules* **32**, 7190–7201 (1999).

43. Dormidontova, E. E. & Lodge, T. P. The order-disorder transition and the disordered micelle regime in sphere-forming block copolymer melts. *Macromolecules* **34**, 9143–9155 (2001).

CHAPTER 3: EFFECTIVENESS OF AN INSTRINIC ENERGY DISSIPATION MECHANISM IN A SINGLE-NETWORK HYDROGEL WITH FATIGUE RESISTANCE

3.1 Chapter Summary

In this chapter, the design strategy for a single-network fatigue-resistant hydrogel with an intrinsic energy dissipation mechanism is presented and tested. The fatigue-resistant and energy-dissipative hydrogel is made from a blend of polystyrene-*b*-polyisoprene-*b*-poly(ethylene oxide) (PS-PI-PEO, SIO) and polystyrene-*b*-polyisoprene-*b*-poly(ethylene oxide)-*b*-polyisoprene-*b*-polystyrene (PS-PI-PEO-PI-PS, SIOIS) polymer microphase separated into a network of tethered micelles. The SIOIS hydrogel is tested in comparison to a similar SOS hydrogel which has a fatigue-resistant network, but does not have an energy dissipation mechanism to study the effectiveness of the network design to dissipate energy while maintaining fatigue resistance. Mechanical compression and tensile tests were used to study the energy dissipation and fatigue resistance of the swollen hydrogel and how those properties relate to bulk toughness in the network. During compressive cycles, the SIOIS hydrogel dissipated 1.82x more energy than the SOS hydrogel at 40% strain and 1.5x more energy at 80% strain. During tensile testing, the SIOIS hydrogel had a 2.74x larger bulk toughness than the SOS hydrogel. The SIOIS hydrogel also showed that it is fatigue-resistant because it maintained its elasticity, high modulus at low strains, energy dissipation, and <1sec recovery times over 12 compressive cycles at 80% strain. Additionally, the structural differences between the SIOIS and SOS hydrogels were compared using SAXS and hydrogel swelling ratios.

3.2 Introduction

The design of hydrogel networks that can withstand mechanically intensive applications has been growing due to interest in using hydrogels in the biomedical field[1–4] in applications such as tissue engineering[5–7] and flexible sensors.[8–11] Hydrogels are excellent candidates for use in these applications because the crosslinked and swollen polymer network is characterized by a large water volume uptake and good elasticity[12] and flexibility[13]. Because in the past hydrogels have demonstrated a susceptibility to mechanical fatigue and brittleness, new design strategies have sought to impart fatigue resistance and bulk toughness to the hydrogel network. While fatigue resistance[6,14,15] and bulk toughness[16–18] have both been implemented into hydrogel networks individually, current hydrogel science has failed to produce a material that exhibits both properties in any significant capacity.

One such example of a hydrogel with exceptional fatigue resistance has been designed by our group. This hydrogel exhibits a high fatigue resistance while still maintaining elasticity, high modulus at low strain, and less than one second recovery times.[6,19] This hydrogel is a thermoplastic elastomer comprised of a blend of diblock and triblock copolymers polystyrene-b-poly(ethylene oxide) (PS-PEO, SO) and polystyrene-b-poly(ethylene oxide)-b-polystyrene (PS-PEO-PS, SOS). This blend of AB and ABA block copolymers self-assembles into a sphere morphology (Figure 3.1a) with amphiphilic character, in which the spheres are made up of glassy, hydrophobic PS, while the matrix in which the spheres sit is comprised of hydrophilic PEO. The ABA polymer spans between the PS spheres so that the spheres act as physical crosslinks providing the structure to the hydrogel network. The ABA strands that tether spherical domains have a very narrow distribution of molecular weights, causing nearly identical chain lengths. The spherical cores are ordered in a body-centered cubic lattice, ensuring a spatially even distribution of crosslinks in the network. The entanglements among the tethers act as additional mobile crosslinks which can move in order to rapidly redistribute stress when the network is under strain. Despite this collection of fatigue-resistant properties, the SOS hydrogels have also proven to be prone to fracture

due to the network's inability to dissipate energy that is concentrated at a crack tip. Therefore, an energy dissipation mechanism is needed in the hydrogel to reduce its brittleness.

Designing a hydrogel that combines fatigue resistance in a hydrogel with an energy dissipation mechanism that can provide toughness to the hydrogel has been a key question for the field.[13,20] Double-network hydrogels have been the most popular avenue for providing an energy dissipation mechanism to the hydrogel. In these double-network hydrogels, one network provides the stability and recovery of the gel shape and the other network is weaker to allow selective network fracture as a way to dissipate energy.[17] Most of the work on double-network hydrogels has been done to find different physical or chemical crosslinks such as ionic bonds,[16,18] and hydrogen bonds[21–23] to act as a recoverable bonds in the sacrificial network. However, these double-network hydrogels still suffer from temporary plastic deformation, longer than ideal recovery times, or low modulus at low strains which is not ideal for many tissue-based applications.[24] We hypothesize that these recovery mechanics are because the energy dissipation mechanism is not an intrinsic part of the recovery system but is two systems working independently. Therefore, these challenges are inherent to the double-network design.

Our strategy to design a fatigue-resistant and energy-dissipative hydrogel has been to introduce an energy dissipation mechanism directly into the single network polymer chains of the already fatigue-resistant SOS hydrogel. This design places an elastic, hydrophobic polymer B block between the hydrophobic polystyrene cores and the hydrophilic polyethylene oxide corona to create a blend of ABC and ABCBA block copolymers which still form a sphere morphology (Figure 3.1b). In the ABC form of the sphere morphology, the rubbery B block is predicted to form a collapsed shell around the glassy PS core.[25] The PEO is solvated with water, forming a matrix surrounding each core and shell domain which are situated on a BCC lattice. Pentablock (ABCBA) copolymer formed by the coupling of two PEO (C block) chain termini in an ABC triblock copolymer creates the network of tethered spheres shown to have good fatigue resistance previously by our group.[6]

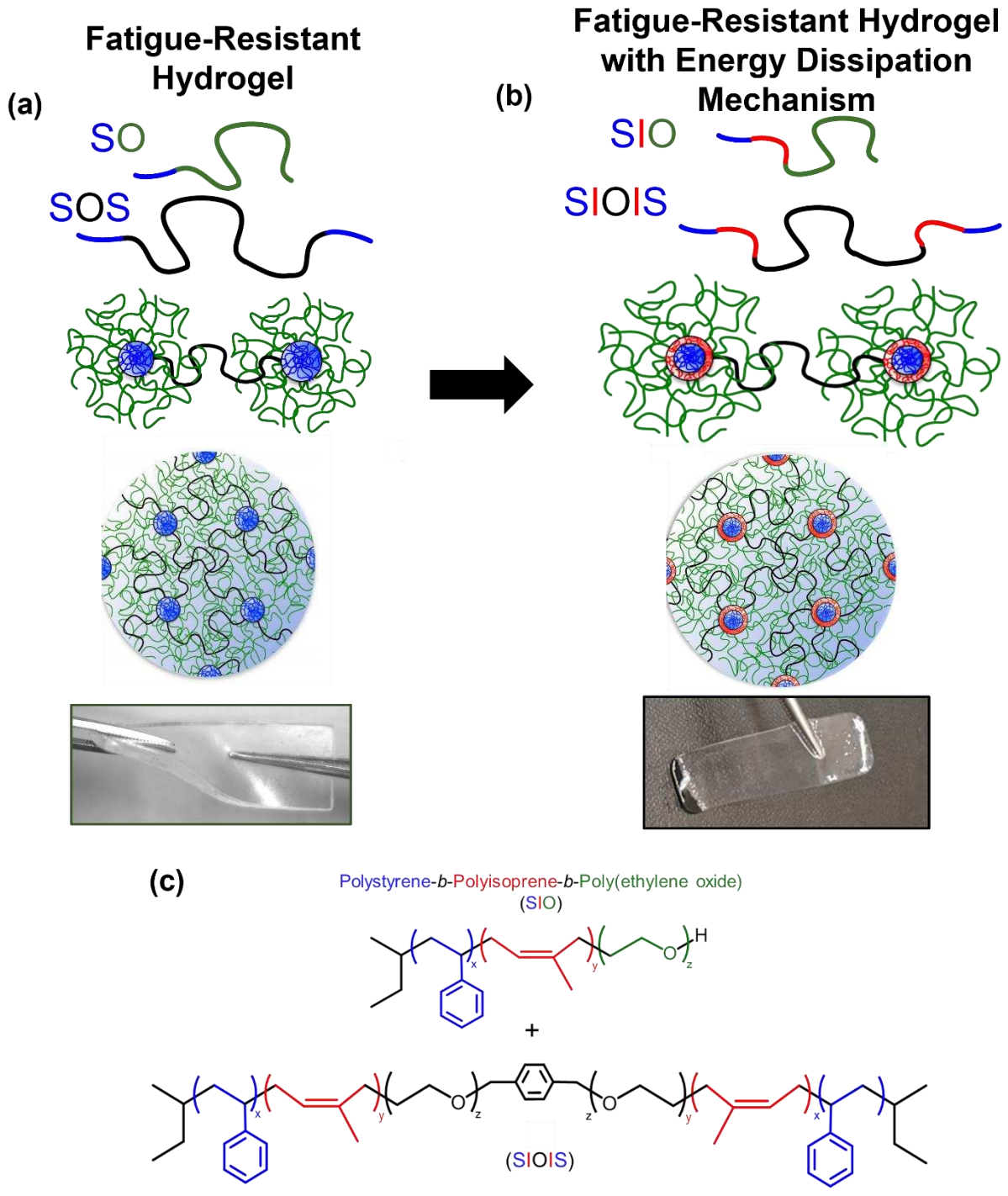

Figure 3.1: (a) Generalized depiction of the polymers and network which make up the fatigue-resistant hydrogel containing the polymers SO and SOS previously reported by the Bailey lab with a photograph of a swollen gel (b) Generalized depiction of the of the polymers and network which make up the fatigue-resistant hydrogel network synthesized with the energy dissipative PI block to make SIO and SIOIS.(c) Chemical structures of the SIO and SIOIS block polymers.

The potential for energy dissipation in this system is based on the hypothesis that strain transferred to this new B block will result in forced contact between its hydrophobic backbone and the hydrophilic solvent, water. A large part of the energy required to create such contacts is energy that will be dissipated. The magnitude can be approximated by considering the free energy of mixing of a polymer-solvent solution between the B block and the aqueous phase. When strain is placed on the hydrogel, mechanical energy will cause the solvated PEO chains to stretch, an entropically unfavorable configuration. At some point when the strain in the PEO chains becomes high enough, some of the mechanical energy being placed on the system is used to stretch the B block into the hydrogel matrix rather than breaking the C-O bonds in PEO (Figure 2.2). This will mechanically raise the enthalpy associated with introducing the hydrophobic B block into the aqueous region of the hydrogel matrix. By choosing a B block with sufficiently high hydrophobicity, the increase in enthalpy will exceed the entropic advantage associated with mixing the dissimilar species; thus, the net change in free energy of mixing the B block and water will overall be positive. The fraction of the mechanical energy that contributes to the creation of such an unfavorable solution is energy that will be dissipated. When the strain is released, the B block and PEO chains will elastically return to their original conformational states because of the entropically-driven restoring force intrinsic to stretched polymer chains. Therefore, the rapid recovery and fatigue resistance of the original SOS hydrogel is maintained.

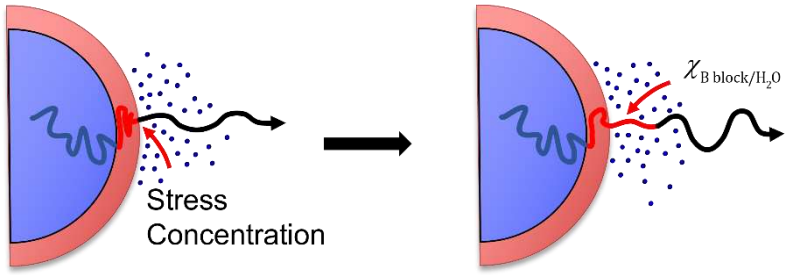

Figure 3.2: Schematic depiction of the energy dissipation mechanism. The black line represents a PEO chain tethered to another sphere. The red line is the PI block and the blue line is the PS block. When the PEO is stretched causing a stress concentration at the PI/PEO junction, instead of breaking, the PI is pulled into the water matrix. This forced interaction between PI and H_2O creates energy that is dissipated.

Polyisoprene (PI) has been chosen as this middle block to be inserted into the SOS hydrogel because it is sufficiently hydrophobic and can be incorporated into the current anionic polymerization procedure used in our group for PS-PEO. Polyisoprene also is liquid/rubbery at room temperature with a Tg around -70 ˚C which ensures that the chains are accessible to pulled into the water matrix when necessary. [26] The block polymers used in this hydrogel are therefore from a blend of polystyrene-*b*-polyisoprene-*b*-poly(ethylene oxide) (PS-PI-PEO, SIO) and polystyrene-*b*-polyisoprene-*b*-poly(ethylene oxide)-*b*-polyisoprene-*b*-polystyrene (PS-PI-PEO-PI-PS, SIOIS) (Figure 3.1c).

In this work, we study the impact of the insertion of a rubbery, hydrophobic B block—polyisoprene—as an intrinsic energy dissipation mechanism in comparison to the original fatigue-resistant SOS hydrogel. This comparison is used to investigate if the insertion of the energy dissipation mechanism maintains the fatigue-resistant properties of the hydrogel network and to examine the effectiveness of the energy dissipation mechanism to measurably dissipate energy and to provide bulk toughness to the hydrogel. The SOS hydrogel is therefore used as a control to study the effects of the new PI block in the SIOIS hydrogel. Throughout this study, the accuracy of the comparison is discussed.

3.3 Results and Discussion

3.3.1 Material Synthesis and Characterization

The SIOIS and SOS polymer systems were synthesized in three steps: macroinitiator synthesis, PEO growth, and a coupling reaction to form the final polymer that will be used in the hydrogel. For SIOIS, the PS-PI-OH macroinitiator was synthesized by sequential addition using anionic polymerization. The PS block size was chosen to ensure the PS molecular weight was large enough for the polymer to remain glassy even when existing in small domains and surrounded by a potential plasticizing polymer of polyisoprene. The PI block size was chosen to ensure the molecular weight was larger than the weight of entanglement for polyisoprene, but still small enough to not require a subsequently large PEO molecular weight that would be difficult to synthesize as discussed in chapter 2. For SOS, the PS-OH macroinitiator was synthesized using anionic polymerization. The PS molecular weight for the SOS polymer was

targeted to match the PS molecular weight of the SIOIS polymer. PEO was then grown in separate reactions from the PS-OH and PS-PI-OH polymers using anionic polymerization. PEO growth in the presence of PI has been shown to be slow, so a stoichiometric excess of EO is added to ensure full conversion. To target the impact of the PS core on the hydrogel function, the size of the PS block was kept nearly the same between the SOS and SIOIS hydrogels within the range of error using ^{1}H-NMR end group analysis (Appendix B Figures B.1-4). The PEO block sizes for both SIO and SO were chosen to target a matching PEO volume fraction that would still fall into the identified volume fraction range for sphere formation observed in AB and ABC polymer systems (>0.87). Because the sphere-forming blocks for SOS and SIOIS contain different molecular weights, the PEO molecular weights in the systems are different.

The resulting SIO and SO polymers were coupled in individual reactions using di-bromoxylene to produce a blend of SIO and SIOIS and a blend of SO and SOS respectively. The coupled polymers were then blended with respective uncoupled polymer to get the final percentage of uncoupled(SIO or SO) and coupled(SIOS or SOS) polymer used for this study. Size exclusion chromatography(SEC) was used to determine the molecular weight distributions of coupled and uncoupled in each polymer system. The subsequent studies performed were on these two hydrogel systems, SOS and SIOIS. SIOIS is a blend of 44% PS-PI-PEO-PI-PS and 56% PS-PI-PEO. SOS is a blend of 41% PS-PEO-PS and 59% PS-PEO (Figure 3.3).

Table 3.2: Table of polymers used to make hydrogels (a) Molecular weights obtained form 1H-NMR (b) volume fractions calculated using the density of the polymers at 140°C[25] (c) Coupling percentage confirmed by GPC for the SOS and SIOIS polymer systems including the uncoupled SO and SIO polymers which become part of the SOS and SIOIS blend after coupling.(d) Sphere size calculated from SAXS and polymer volume fraction.

Polymer	S Mn[a] (g/mol)	B/I Mn (g/mol)	O Mn (g/mol)	Total Mn (g/mol)	f_S[b]	$f_{B/I}$	f_O	Coupling Percentage[c]	SC Sphere Radius (nm)[d]
SO	9600	-	73000	82500	0.126	-	0.874	-	
SOS	19200	-	146000	165100	0.126	-	0.874	41% SIOIS	11.25
SIO	10200	2800	102300	115300	0.096	0.031	0.874	-	
SIOIS	20400	5200	204600	230600	0.096	0.031	0.874	44% SIOIS	13.99

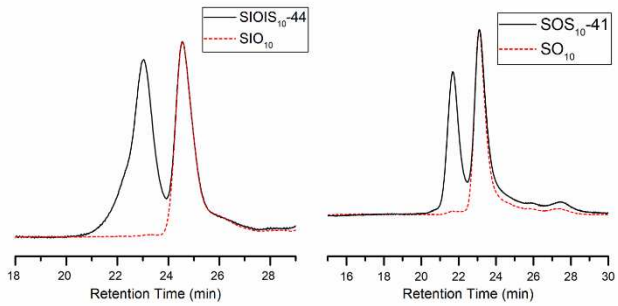

Figure 3.3: (a) GPC data for the SIOIS and SOS hydrogel systems. Black lines show the coupled and uncoupled polymer in the blend and the red lines show the relative elution time of the uncoupled polymer before the coupling reaction.

3.3.2 Hydrogel Formation

The synthesized polymer systems were then processed individually to form the tethered micelle network and swollen in water to form hydrogels. Previous study of the SOS system has shown that the formation of glassy spheres is crucial to the structural integrity of the tethered micelle polymer network.[19] The spheres act as the physical crosslinks in the network with the coupled polymer spanning between them. In the SOS system, the spheres were formed in the melt by heating at 150°C for 20 minutes in a melt press with a small amount of pressure during which time the PS and PEO polymers microphase separate to form a sphere morphology. Upon removal from the heat, the PS block becomes glassy creating the physical crosslink. Melt assembly was not sufficient for the SIOIS hydrogel as the larger molecular weight chains have slower chain mobility kinetics as is detailed in chapter 2. Therefore, solvent assembly in $CHCl_3$ was used to promote phase separation for SIOIS. The SIO/SIOIS polymer was dissolved in 1%w/v chloroform and allowed for the solvent to completely evaporate, usually around 7 days. Samples were then dried under room temperature vacuum for 2 hours to ensure all solvent was removed before being placed in DI water for 24 hours. It is well-known that sample reproducibility can be an issue during solvent-casting, so care was taken to use the same sample concentration and solvent casting set-up for each sample (Figure 2.4).

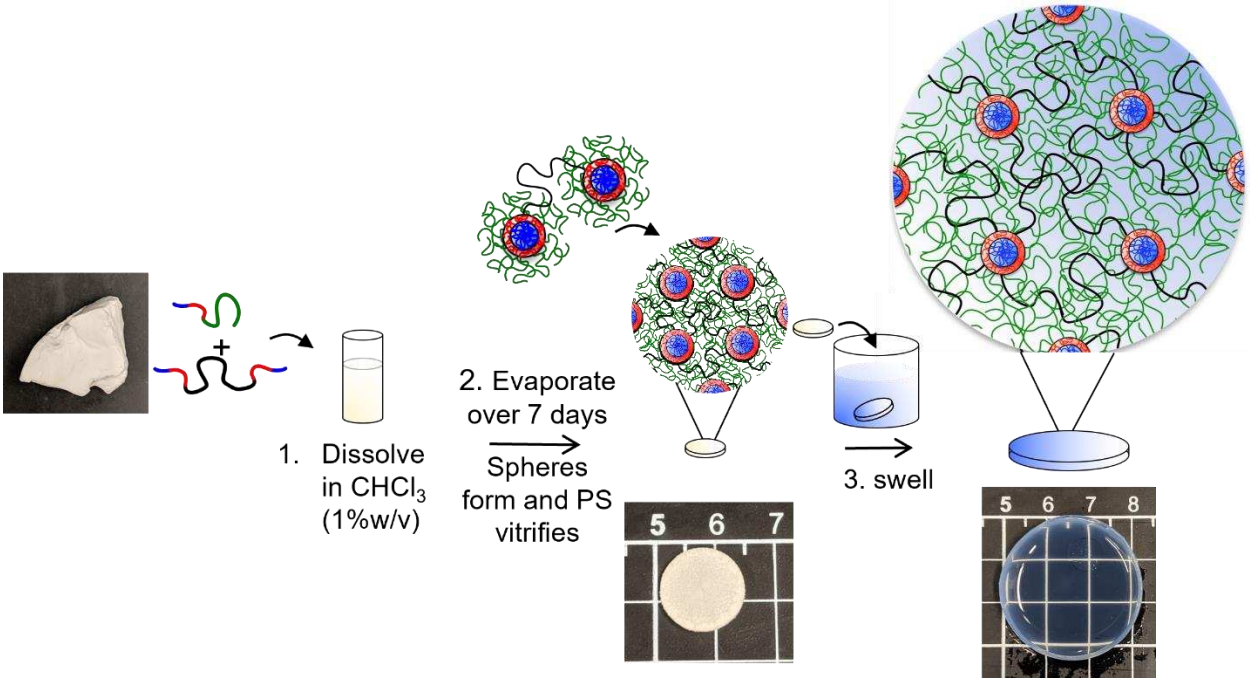

Figure 3.4: Schematic representation of the processing of the SIOIS polymer. The blend of SIO and SIOIS polymer is dissolved in CHCl3 and left to evaporate over ~7 days. In solution, the polymers phase separate into the sphere morphology which is trapped upon drying. The PS sphere are now glassy at RT. When swollen in water, the glassy PS spheres act as physical crosslinks tethered together by SIOIS. Inset photos show the physical state of the SIOIS polymer during each step.

The formation of a sphere morphology in dry samples of the SIOIS and SOS polymers was confirmed using small angle X-ray scattering (SAXS) (Figure 3.5a). The SOS hydrogel was melt-pressed and then heated again in the SAXS. The SIOIS hydrogel was solvent-cast as described above and then heated in the SAXS. Both samples were heated to 100°C because PEO is crystalline below 70°C. The triangles correspond to expected scattering reflections for a body-centered cubic sphere morphology. The SAXS data for SOS shows resolved peaks at the $\sqrt{4}$ and $\sqrt{6}$ reflections. These same reflections are broadly combined into one peak in the SIOIS SAXS profile. The presence of these resolved scattering peaks indicates that the SOS system is forming a periodic morphology of spheres situated on a BCC lattice. The lack of these resolved scattering peaks in the SIOIS sample indicate that the SIOIS system is forming a liquid-like packing of spheres, a morphology of spheres not situated in a periodic lattice structure. The formation of this non-periodic structure in the SIOIS system is expected due to the large molecular weight polymers which have been shown to have decreased SAXS resolution even in melt-pressed samples due to the kinetics of phase separation that occurs with larger polymer chains. While the SOS forms this BCC

shape in the melt, once the polymer blend is solvated with water, the BCC structure is largely lost resulting in a more liquid-like packing of the spheres. The spheres themselves are different sizes. The size of the spheres can be determined from the principal scattering peak (q*) using Bragg's Law and the volume fraction of the polymer blocks as described in Appendix D. An SIOIS sphere is approximated to have a radius of 13.99nm while an SOS sphere is approximated to have a radius of 11.25nm. The larger size of the SIOIS sphere is to be expected considering the larger molecular weights of the polymers in the sphere-forming portion of the SIOIS sample.

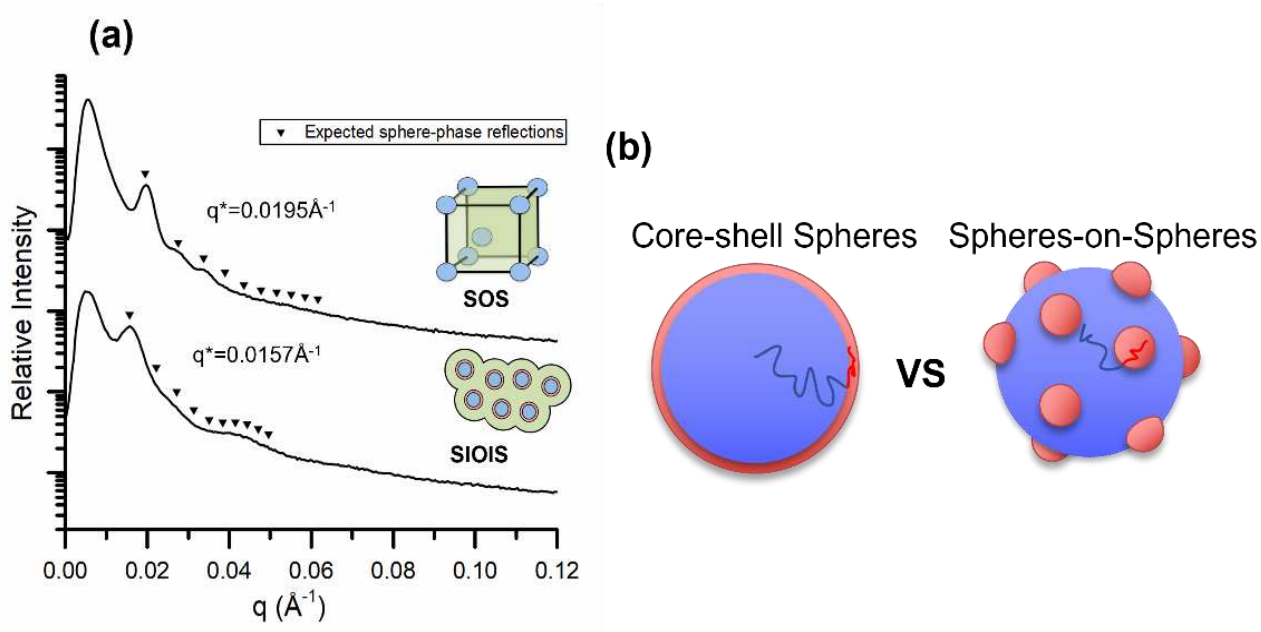

Figure 3.5: (a) Shows the SAXS for the SIOIS-44 and SOS-41 polymer blends. The triangles show the scattering reflections for a polymer forming spheres situated on a BCC lattice. SOS-41 is forming this BCC morphology of spheres. SIOIS-44 is forming a liquid-like spheres morphology. (b) Schematic depictions of the size of the PS-PI spheres. PS is represented by blue and PI is represented by red.

Based on the size of the spheres calculated from the SAXS, the actual radius of the PI shell in the SIOIS around each glassy PS sphere would be forced to be very small to cover the entire surface of the sphere (1.24nm). If the PI was truly in an even layer around the PS sphere, this small radius of PI would require the PI to be lying flat in sheets. Therefore, it is more likely that the PI has formed rubbery spheres on the PS spheres allowing a larger freedom of movement for the PI block similar to the "spheres-on-spheres" morphology observed by Stadler et. al. with PS-PB-PMMA polymers (Figure 3.5b).[27] Formation

of this “spheres-on-spheres” morphology is typically observed due to frustration between the order of the blocks in an ABC block copolymer not following the increasing order of interaction parameters between the blocks.[28] This block frustration is true for SIOIS where the χ value of each block results in interaction parameter ratios between the blocks which favor interactions between the PS and PEO blocks over interactions between the PB and PEO blocks.[29,30] This relationship is also true for the PS-PB-PMMA polymer in which the “spheres-on-spheres” morphology was first observed.[31] However, regardless of block/interaction parameter frustration, continuous domains require significant chain stretching which also would contribute to the formation of the “spheres-on-spheres” morphology in the SIOIS hydrogel. The “spheres-on-spheres” morphology could be visible using transmission electron microscopy (TEM) but is not distinguishable by SAXS which can only show the general “sphere” form. Unfortunately, the necessity of using polymer samples with large molecular weights and large PEO content which is crystalline at the low temperatures required for processing samples inhibits the preparation of TEM samples. The grouping of PI in spheres rather than a flat layer would likely not have an impact on the energy dissipation mechanism or the recovery mechanism as the polymer as the PI-PEO junction point is still accessible during mechanical load.

A comparison of the swelling ratios of the SIOIS and SOS hydrogels (n=4) shows that the SOS hydrogel is taking up less water than the SIOIS hydrogel despite having a smaller amount of coupled

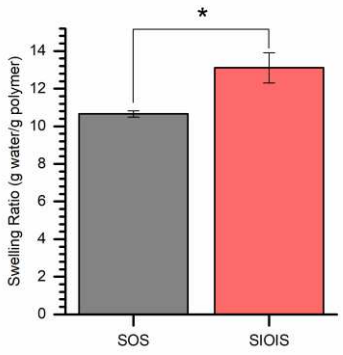

*Figure 3.6: Graph of the average swelling ratio of the SIOIS hydrogel system and the SOS hydrogel system with standard deviation. The * indicates that the values between SOS and SIOIS are significantly different.*

polymer. (Figure 3.6) In a typical hydrogel system, crosslink density is inversely related to swelling; therefore, it would be expected that the larger coupling of the SIOIS hydrogel would result in a smaller swelling ratio. It is unclear why the swelling ratio is different for these hydrogels. It is possible that some of the large molecular weight polymer in the SIOIS is not participating in crosslinking the network. This could be from more looping of the polymer network or the presence of a known high molecular weight contaminant of PEO that can be formed during the synthesis of SIO that then causes star polymers of PEO to form during the coupling reaction.[32]

As discussed above, limiting the variables between the SOS and SIOIS molecules was important to probe the effectiveness of the PI block as energy dissipation mechanism. When comparing hydrogels, the swelling ratio, the coupling percentage, and the modulus of the material are related, therefore we could choose any to control. Previous work in this group has shown that while swelling ratio and coupling percentage are related, swelling ratio is even more strongly tied with modulus of the polymer due to variables in how the coupling percentage is calculated from SEC. Because of the divergence from the expected swelling ratio of the SIOIS polymer and because our goal was to compare the mechanical properties of the SIOIS and the SOS polymers, we chose to use the compressive moduli of the samples as a comparison. Therefore, the swelling ratios and coupling percentages shown here are the result of a preliminary study comparing the compressive modulus of SIOIS and SOS samples at multiple coupling percentages and swelling ratios. Once the SIOIS polymer was coupled, the SOS was blended to match the coupling percentage that would match the compressive modulus of the SIOIS found in the preliminary study.

3.3.3 Mechanical Performance

Unconfined compression tests were completed on the SOS and SIOIS systems to 40% compressive strain and 80% compressive strain (Figure 3.7a). The stress-strain curves show the averaging of 6 successive cycles for 4 samples of SOS and 6 successive cycles for 5 samples of SIOIS. The compressive moduli for both samples are different at 20% and 40% strain but statistically similar at 60%

and 80% strain.as shown in Figure 3.7b. While hysteresis in the loading and unloading compression curves is observed in both samples, the hysteresis in the curves for SIOIS is larger than in the SOS at 40% strain and 80% strain. It is likely that some of the hysteresis is caused by the movement of water back into the sample after compression as has been seen previously with SOS compression tests[6]. However, the difference between the amount of energy dissipated cannot be contributed solely to the water. The energy needed to pull the B block into the water during loading is energy that is not stored during the mechanical event; therefore, the stress that was experienced by the polymer chains during unloading is much lower

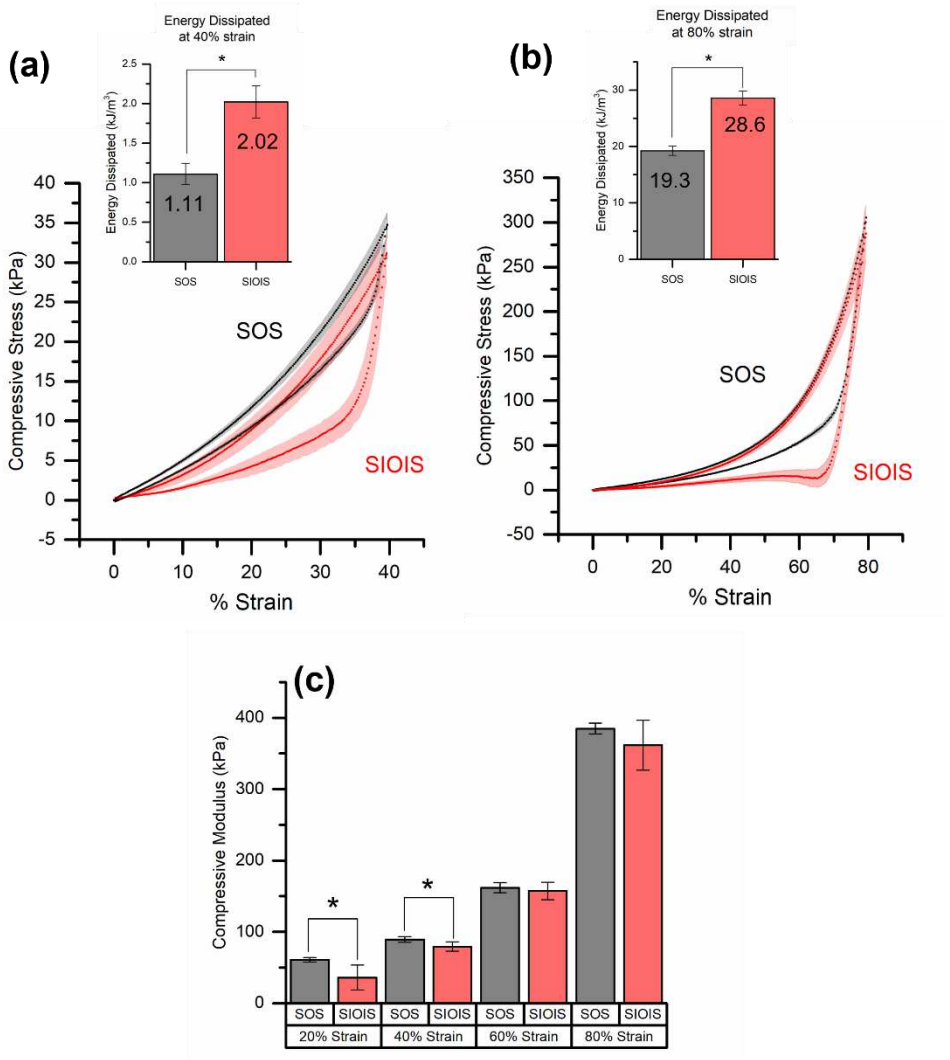

*Figure 3.7: Compression cycles for the SOS hydrogel system and the SIOIS hydrogel system to (a)40% and (b) 80% strain. Averaging of 4 samples (SOS) and 5 samples (SIOIS) completing 6 consecutive cycles each with y-axis error bars. Insets show the difference in the average energy dissipated during an average loading and unloading cycle. The energy dissipation values for SOS and SIOIS are significantly different. (c)Average compressive modulus for the SOS and SIOIS systems at 20%, 40%, 60% and 80% strain. The * indicates that the values between SOS and SIOIS are significantly different.*

resulting in the hysteresis in the compression cycle. The difference in the hysteresis shows a 1.82x increase in the energy that is dissipated by the SIOIS hydrogel at 40% strain and a 1.5x increase in the energy that is dissipated by the SIOIS hydrogel at 80% strain.

The fatigue resistance of both the SOS and the SIOIS hydrogels is shown in Figure 3.8a with unconfined compression for a single SOS and SIOIS sample over 6 cycles at 40% strain and over 12 cycles at 80% strain with less than 1 second recovery times between cycles. For both hydrogels, there is a small decrease in the compressive stress after the 1st cycle with complete elasticity in all cycles as well as little change in the hysteresis between the cycles. Additionally, the elasticity, high modulus at low strains, and fast recovery times that are important characteristics of the SOS hydrogel are still observed in the initial cycle of the SIOIS hydrogel and throughout multiple cycles of its use. Figure 3.8b shows that there is nearly no change in the energy dissipated between 12 cycles of either hydrogel. The lack of significant change in the modulus, recovery time, and energy dissipated by either hydrogel shows that the SIOIS

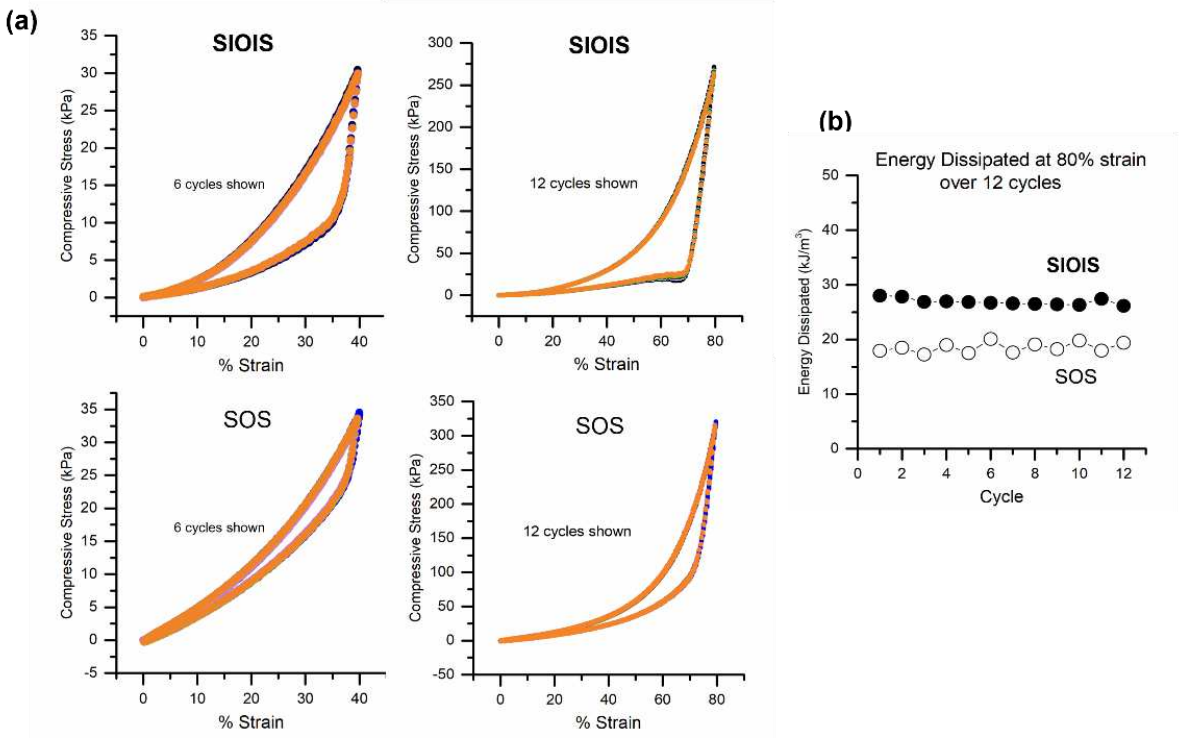

Figure 3.8: (a)6 consecutive compression cycles and 12 consecutive compression cycles for a representative SOS and SIOIS hydrogel with less than one second recovery between each cycle overlaid. (b) Energy dissipated during each cycle of the 12 cycle series for a SOS hydrogel and a SIOIS hydrogel to 80% strain showing that there is little change of the amount of energy dissipated between each cycle.

hydrogel is using the tethered micelle network to distribute stress. The fast recovery times while still dissipating energy shows that the energy dissipation mechanism is not impeding the recovery of the SIOIS hydrogel maintaining its fatigue resistance. When considering the total amount of energy dissipated over multiple cylces, the SIOIS hydrogel is able to dissipate 1.8x as much energy over the 6 cycles as the SOS hydrogel when compressed to 40% strain and 1.45x as much energy as the SOS hydrogel for 12 cycles at 80% strain (Figure 9). This study demonstrates the potential of the SIOIS hydrogel to have a longevity of its mechanical properties.

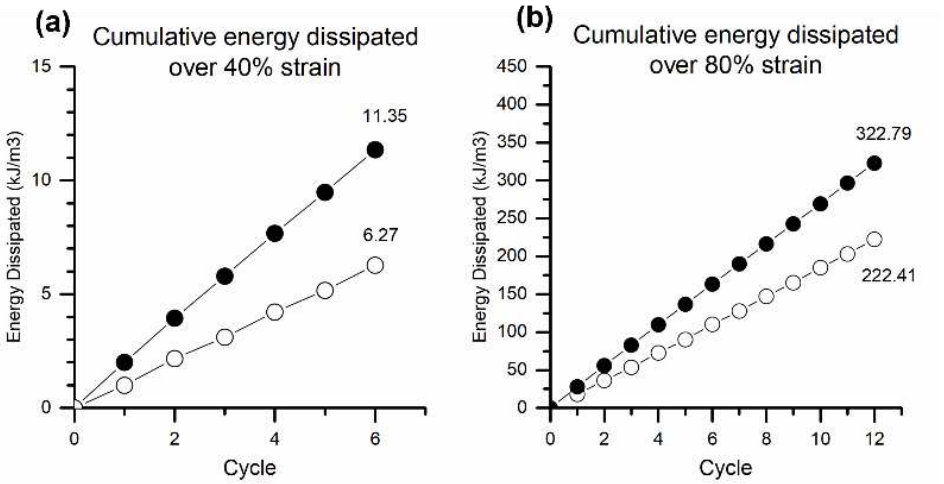

Figure 3.9:(a) The amount of energy that is dissipated over 6 cycles of an SOS hydrogel and an SIOIS hydrogel at 40% strain. (b) The amount of energy dissipated over 12 cycles of the SOS and SIOIS hydrogel when compressed to 80% strain.

To test different mechanical loading forces on the hydrogel network, cyclic tensile tests were performed to 75% average strain length at break at 2% strain/sec. Cyclic tensile tests for both the SIOIS and SOS do show elasticity in the hydrogel, but do not show a hysteresis between the loading and unloading curves as was observed in cyclic compression testing (Figure 3.10). The lack of hysteresis observed during cyclic tensile testing is likely caused by fewer chains being engaged to the point of failure during tensile testing. During compression, chains and their junctions are engaged over the entire surface area of the gel because of the change of size as the hydrogel is compressed. However, during tension, chains and junctions are only experiencing forces in a uniaxial direction. The change in the enthalpy of the system due to mixing is partly governed by the volume fractions of polymer and water

that are in contact.[33] Therefore, the lack of energy dissipation is likely the result of too few PI chains being forced to mix with water as an energy dissipation mechanism. It is possible that energy dissipation is still occurring, but is not contributing significantly enough to the network to register as a difference in the loading and unloading cycles during the cyclic tensile test.

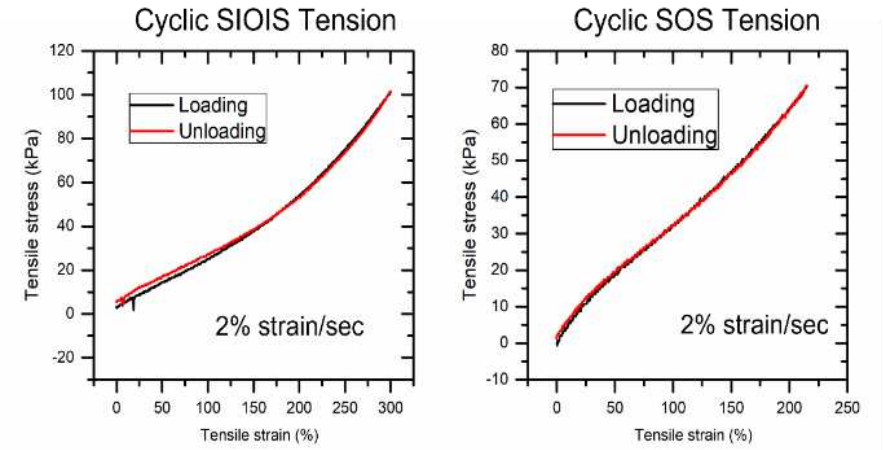

Figure 3.10: Cyclic tensile tests for an SIOIS hydrogel and an SOS hydrogel completed at 2% strain/sec up to 75% of the average strain at break for each hydrogel. The cyclic tensile tests for both samples show no hysteresis between the loading and unloading cycles.

Uniaxial tension tests to break were completed for 3 SOS and SIOIS hydrogels as shown in Figure 3.11a. Similar to the compression tests, the initial moduli of the samples is similar in both hydrogels. However, the moduli seem to have an inflection point above 200% strain where the modulus increases. This could be the result of the polymer drying during testing and allowing pockets of PEO to crystallize, increasing the stiffness of the gel. The similarity in the moduli at low strain of both SOS and SIOIS points to the presence of a similar number of crosslink junction points in both hydrogels. The similarity in the crosslink density suggests that the tethered spheres are behaving similarly in both hydrogels and the presence of the energy-dissipative B block is not negatively impacting the formation of the tethers during the polymer processing step. The SIOIS hydrogel has both higher stress at break and higher strain at break for all three samples. Therefore, the SIOIS hydrogel has an 2.74x increase in the overall bulk toughness available compared to the SOS hydrogel as shown in Figure 3.11c. This is likely a result of the PI acting as a slight plasticizer to the junction between the PEO and the glassy PS sphere. Throughout the study of the SOS network, the Bailey group has long suspected that the point of failure in the SOS gels is the junction where the glassy sphere is covalently bonded to the hydrated PEO. Therefore,

we suspect that, in the SIOIS gel, the PI is a rubbery junction point which provides flexibility to the junction resulting in an increase in the tensile strain at break, even if the PI is not interacting with the water to dissipate energy. From tensile testing alone, it is unclear if the increased strain at break is caused by the PI block entering the water matrix and elongating the chain distance between crosslinks or if the increased flexibility allowed better movement and elongation of the PEO chains.

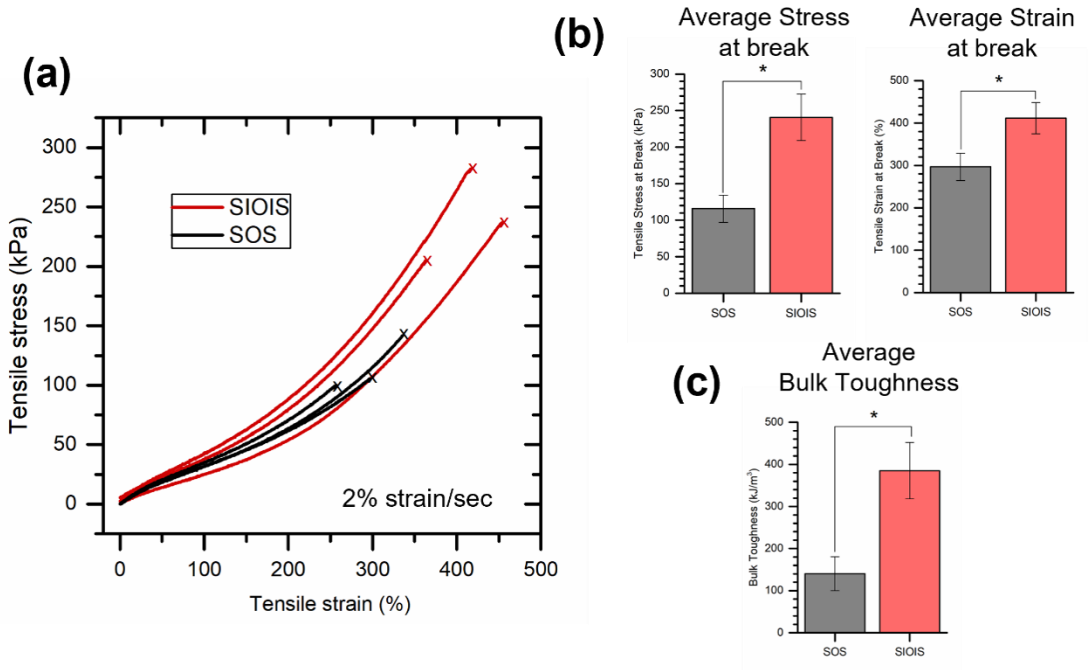

*Figure 3.11: (a) Tensile tests for 3 SIOIS hydrogels and 3 SOS hydrogels completed at 2% strain/sec. (b) Comparisons of average stress at break, average strain at break. (c) Average bulk toughness of the SIOIS hydrogels and SOS hydrogels. The * indicates that the values between SOS and SIOIS are significantly different.*

While we believe the comparison between the SIOIS hydrogel and the original, non-dissipative hydrogel (SOS) was necessary to observe the impact of the energy dissipation mechanism, the difficulty in making an accurate comparison between the two should not be understated. Future studies are of interest to understand the role that a similar-sized sphere rather than a similar sized PS chain would play.

3.4 Conclusion

An energy-dissipative and fatigue-resistant hydrogel (SIOIS) was compared to the fatigue-resistant hydrogel (SOS) to study the effectiveness of combining energy dissipation and fatigue resistance into a single network through compression and tensile testing. The inserted PI block did have an effect on

the physical and mechanical properties of the hydrogel. The formation of the sphere morphology in the SIOIS polymer was significantly different than the SOS polymer and required solvent-casting to process the polymer instead of melt-pressing. The SIOIS hydrogel swelled more than the SOS hydrogel despite having a larger coupling percentage. During compressive cycles, the SIOIS hydrogel was able to dissipate more energy than the SOS hydrogel and 40% and 80% strain while having nearly the same compressive modulus. During tensile testing the SIOIS hydrogel, had a larger average strain at break, stress at break, and overall bulk toughness than the SOS hydrogel. Overall, the inserted PI block provides a rubbery plasticizer to the junction point of the PS and PEO chains where fracture is likely occurring resulting in an increased toughness to the hydrogel. The PI block is also dissipating measurable amounts of energy when enough of the chains are engaged with the water matrix such as in compression testing. Importantly, the fatigue resistance of the tethered micelle hydrogel network is not affected by the insertion of the energy-dissipative PI block with the fast recovery times, high moduli at low strains and elasticity of the SOS hydrogel being maintained in the SIOIS hydrogel. This design strategy is a promising step to having energy dissipation and fatigue resistance in a single-network hydrogel.

3.5 Experimental

3.5.1 Materials

Styrene (99.5% for analysis, stabilized, Acros) and ethylene oxide (99.5%, compressed gas, Aldrich) were purified by vacuum distillation from dried dibutylmagnesium (1.0M solution in heptane, Aldrich). Isoprene (99%, p-tert-butylcatechol inhibitor, Aldrich) was purified by vacuum distillation from n-butyl lithium (1.6M solution in hexane). Argon degassed cyclohexane (CHX) was purified by passing the solvent over activated alumina followed by Q-5-like supported copper catalyst (Glass Contour). Argon-degassed tetrahydrofuran (THF) was purified by passing the solvent over activated alumina. High-purity argon (99.998%, Airgas) was passed through additional oxygen and moisture traps prior to use. All chemical syntheses were carried out in a dry argon atmosphere using standard Schlenk line techniques.

3.5.1 Methods

Synthesis of PS-PI-OH Macroinitiator

Purified styrene monomer was added under argon to a vigorously stirring solution of sec-butyl lithium and dry, air-free cyclohexane in a 1 L reaction vessel. The temperature of the reaction mixture was raised to 40°C and stirring continued for approximately 8 hours. At this point, the reactor pressure was reduced to approximately 1 psig. Purified Isoprene was added to the reaction vessel slowly to ensure pressure did not rise above 10psig. The reaction was maintained at 40 °C for 8 hours. At this time, ethylene oxide was added to the reactor and allowed to react for 24 hours. The reaction was terminated by direct addition of acidic methanol. The polymer was rotovapped and precipitated in a 1:3 mixture of isopropanol and methanol (2 L total) to give a white solid. The polymer was dried under vacuum at room temperature for 48 hours.

Synthesis of PS-PI-PEO

PS-PI-OH (1g) was dried overnight under vacuum in a 2L reaction vessel with a Teflon stir bar. The reactor was evacuated and backfilled with purified argon before the addition of approximately 1 L of dry, air-free THF. Concentrated potassium naphthalenide in dry THF was added to the polymer solution via cannula until a light green color persisted for at least 15 minutes. The temperature of the reaction mixture was raised to 45°C and excess ethylene oxide was added under argon with vigorous stirring. Stirring was continued for approximately 24 hours. The reaction was terminated by direct addition of acidic methanol. The polymer was rotovapped and precipitated in pentane to give a light yellow solid. The polymer was dried under vacuum at room temperature for 48 hours. The polyisoprene isomers were 92% 1,4-polyisoprene and 8% 3,4-polyisoprene.

Synthesis of PS-OH Macroinitiator

In a 1L reactor, purified styrene was added to a vigorously stirring solution of sec-butyl lithium and dry, air-free cyclohexane (500mL). The reactor was heated to 40°C and allowed to react for 8 hours.

Ethylene oxide was then added and allowed to react for 24 hours. The reaction was terminated with acidic methanol. The polymer was precipitated into methanol.

Synthesis of PS-PEO

PS-OH (1g) was placed into a 2L reactor and evacuated for 12 hours. The reactor was evacuated and backfilled with Argon 5x before adding 1L of dry, air-free THF. Once the polymer was dissolved, concentrated potassium naphthalenide was added via cannula until a light green color persisted for 15 minutes. Ethylene oxide was added and allowed to react for 24 hours. The reaction was terminated with acidic methanol. The polymer was precipitated into pentane with roughly the ratio of 1ml THF:8mL pentane. The polymer was then placed into the vacuum oven and allowed to dry for 48 hours.

Coupling of PS-PI-PEO to make PS-PI-PEO-PI-PS and PS-PEO to PS-PEO-PS

Uncoupled polymer (SO or SIO) (1g) was dried overnight under vacuum in a 500mL flask. The polymer was then dissolved in ~200mL of dry, air-free THF. Potassium naphthalenide with a known concentration was added to the purification flask via air-free syringe until a light green color persisted for at least 20 minutes. The solution of α,α′-dibromo-p-xylene dissolved in THF was added to the flask via syringe pump (1mol DBX:2mol KNAP added) over the course of 8 hours. The next day, the polymer was precipitated into pentane and dried under vacuum at room temperature for 48 hours.

NMR/GPC

^{1}H NMR spectra were collected in $CDCl_3$ (unless otherwise stated) using a Bruker Advance NEO 400 MHz Spectrometer equipped with Prodigy BBFO cryo-probe (ns = 256, 10 s delay, 2.5sec acquisition time). Volume fractions were calculated using the molecular weight and the polymer density at 140°C.[34]

Gel Permeation Chromatography was completed using a Viscotek RIMax system fitted with three 7.5 x 300 mm PolyPore (Agilent) columns in series, an Alltech external column oven set to 40 °C, and a Viscotek differential refractive index (RI) detector with sample concentrations of 2 mg mL^{-1} . Stabilized and degassed THF was used as the eluent and run time was 45 minutes for all samples. Mass percent of coupled polymer was calculated by taking the area under curve of each sample. For the SIOIS polymer, the high molecular weight contaminant was excluded from the area.

Hydrogel Processing and Fabrication

SOS polymer was melt processed using a Carver Model CH manual hydraulic press using various stainless steel molds with FEP-coated Kapton FN (Dupont, 500FN131) and preheated aluminum plates on either side of the sample. The sample mold was filled with excess polymer, placed between the plates, placed under slight pressure (100lbs) and heated at 150°C for 20 minutes or until the pressed sample was clear while still warm. The sample was then removed from heat and allowed to come to room temperature. The polymer was then placed in DI water and sparged for 60 seconds to remove excess oxygen from the water. The sample was left to come to equilibrium for 24 hours before testing.

SIOIS polymer (0.1g) was placed into a glass 5 mL vial with a 3mm diameter base with 1mL of $CHCl_3$ and a small stirbar until the polymer was completely dissolved. After the polymer was dissolved, the stir bar was removed, and the open vial was covered in foil and placed into a vacuum holm with the ChemCap partially open to air. The sample was left for 7 days to evaporate before opening. To ensure complete evaporation of the $CHCl_3$, the sample was left under vacuum for 2 hours. ^{1}H-NMR with Toluene-d_8 as the solvent was used to confirm the absence of excess $CHCl_3$. The polymer was then placed in DI water and sparged for 60 seconds to remove excess oxygen from the water. The sample was left to come to equilibrium for 24 hours before testing.

SAXS

SAXS data were collected on a Rigaku S-Max 3000 High Brilliance 3 Pinhole SAXS system outfitted with a MicroMax-007HFM Rotating Anode (CuKa), Confocal Max-FluxTM Optic, Gabriel Multiwire Area Detector and a Linkam thermal stage. Dry samples were subjected to a heating ramp from to 150°C at 10°C/sec and annealed for 1 hour. The sample was then cooled back to 100°C and data was collected for 1 hour. The crystallization of PEO below 70°C disrupts the polymer morphology, so it is not useful to characterize the polymers below 75°C. The SOS sample was melt pressed at 150°C for 20 min and cooled to room temperature before being subjected to the temperature ramp. The SIOIS SAXS sample was taken directly into the SAXS after solvent casting with no additional annealing step.

Compression

Compression tests were performed on an TA Ares rheometer using a Peltier base attachment. The circular samples were punched out of a larger hydrogel to an 8mm diameter. The tests were done with the sample submerged underwater with the upper plate having a diameter of 25mm and a lower plate having a functionally infinite diameter. The samples were compressed at a strain rate of 10%strain/sec with no hold period between cycles. Unless otherwise noted, the data is the average of 5 samples of SIOIS and 6 cycles for each sample and 4 samples of SOS and 6 cycles for each sample. Compressive Young's moduli were calculated by dividing the stress at a given strain by that strain. Energy dissipated was calculated by subtracting the area under the unloading curve from the area under the loading curve with the units corrected. Recovery testing was completed on one sample of SOS and one sample of SIOIS at 10%strain/sec to 40% strain for 6 cycles and to 80% strain for 12 cycles.

Tension

Tensile testing was completed on an Instron Model 4442 system fitted with pneumatic grips and a 50N load cell. A dogbone shape was punched out of the swollen hydrogel to use for testing with the resulting dogbone being on average 13.5mmx1mmx1.5mm. Once in the grips, the sample was pulled until a force of ~0.10N was observed to ensure that the hydrogel was fully engaged. Samples were strained at 2%strain/sec until break. For cyclic tensile testing, the sample was strained at 2%strain/sec up to 75% of the average strain at break for the polymer system. Bulk toughness was calculated by taking the area under the tensile curve with units corrected.

Statistical Difference Analysis

Data sets were first evaluated for normality using the Anderson-Darling test and then evaluated for equal variance using Levene's test. Once these parameters were established, significance was determined using ANOVA with post hoc Tukey's test (p value = 0.05). For data sets that did not have equal variance, the Games-Howell test was performed (p value = 0.05). All statistics were performed using Minitab 18.

3.6 References

1. Calvert, P. Hydrogels for Soft Machines. *Adv. Mater.* **21**, 743–756 (2009).
2. Cascone, S. & Lamberti, G. Hydrogel-based commercial products for biomedical applications: A review. *Int. J. Pharm.* **573**, (2020).
3. Correa, S. *et al.* Translational Applications of Hydrogels. *Chemical Reviews* **121**, 11385–11457 (2021).
4. Fan, H. & Gong, J. P. Fabrication of Bioinspired Hydrogels: Challenges and Opportunities. *Macromolecules* 2769–2782 (2020) doi:10.1021/acs.macromol.0c00238.
5. Spicer, C. D. Hydrogel scaffolds for tissue engineering: the importance of polymer choice. *Polym. Chem.* **11**, 184 (2019).
6. Lewis, J. T., Fischenich, K. M., Haut Donahue, T. L. & Bailey, T. S. Nanostructure-Driven Replication of Soft Tissue Biomechanics in a Thermoplastic Elastomer Hydrogel. *ACS Biomater. Sci. Eng.* **4**, 3854–3863 (2018).
7. Wang, H. & Heilshorn, S. C. Adaptable Hydrogel Networks with Reversible Linkages for Tissue Engineering. *Adv. Mater.* **27**, 3717–3736 (2015).
8. Deng, Z. *et al.* Stimuli-Responsive Conductive Nanocomposite Hydrogels with High Stretchability, Self-Healing, Adhesiveness, and 3D Printability for Human Motion Sensing. *ACS Appl. Mater. Interfaces* **11**, 6796−6808 (2019) doi:10.1021/acsami.8b20178.
9. Ling, Q. *et al.* Tough, Repeatedly Adhesive, Cyclic Compression-Stable, and Conductive Dual-Network Hydrogel Sensors for Human Health Monitoring. *Cite This Ind. Eng. Chem. Res* **60**, 18373–18383 (2021).
10. Kweon, O. Y., Samanta, S. K., Won, Y., Yoo, J. H. & Oh, J. H. Stretchable and Self-Healable Conductive Hydrogels for Wearable Multimodal Touch Sensors with Thermoresponsive Behavior. *ACS Appl. Mater. Interfaces* **11**, 26134–26143 (2019).
11. Ge, G. *et al.* Muscle-Inspired Self-Healing Hydrogels for Strain and Temperature Sensor. *ACS Nano* **14**, 218–228 (2020).
12. Sun, J.-Y. *et al.* Highly stretchable and tough hydrogels. *Nature* **489**, 133-136 (2012) doi:10.1038/nature11409.
13. Creton, C. 50th Anniversary Perspective: Networks and Gels: Soft but Dynamic and Tough. *Macromolecules* **50**, 8297–8316 (2017).
14. Ito, K. Slide-ring materials using topological supramolecular architecture. *Curr. Opin. Solid State Mater. Sci.* **14**, 28–34 (2010).
15. Ito, K. Novel Cross-Linking Concept of Polymer Network: Synthesis, Structure, and Properties of Slide-Ring Gels with Freely Movable Junctions. *Polymer Journal,* **39***,* 489–499 (2007) doi:10.1295/polymj.PJ2006239.
16. Luo, F. *et al.* Oppositely charged polyelectrolytes form tough, self-healing, and rebuildable hydrogels. *Adv. Mater.* **27**, 2722–2727 (2015).
17. Gong, J. P., Katsuyama, Y., Kurokawa, T. & Osada, Y. Double-network hydrogels with extremely high mechanical strength. *Adv. Mater.* **15**, 1155–1158 (2003).

18. Su, E. & Okay, O. Polyampholyte hydrogels formed via electrostatic and hydrophobic interactions. *Eur. Polym. J.* **88**, 191–204 (2017).

19. Guo, C. & Bailey, T. S. Highly distensible nanostructured elastic hydrogels from AB diblock and ABA triblock copolymer melt blends. *Soft Matter* **6**, 4807 (2010).

20. Zhao, X. Multi-scale multi-mechanism design of tough hydrogels: Building dissipation into stretchy networks. *Soft Matter* **10** 672–687 (2014).

21. Tuncaboylu, D. C., Sari, M., Oppermann, W. & Okay, O. Tough and self-healing hydrogels formed via hydrophobic interactions. *Macromolecules* **44**, 4997–5005 (2011).

22. Hu, X., Vatankhah-Varnoosfaderani, M., Zhou, J., Li, Q. & Sheiko, S. S. Weak Hydrogen Bonding Enables Hard, Strong, Tough, and Elastic Hydrogels. *Adv. Mater.* **27**, 6899–6905 (2015).

23. Meco, E. & Lampe, K. J. Impact of Elastin-like Protein Temperature Transition on PEG-ELP Hybrid Hydrogel Properties. *Biomacromolecules* **20**, 1914–1925 (2019).

24. Fischenich, K. M., Lewis, J. T., Bailey, T. S. & Donahue, T. L. H. Mechanical viability of a thermoplastic elastomer hydrogel as a soft tissue replacement material. *J. Mech. Behav. Biomed. Mater.* **79**, 341–347 (2018) doi:10.1016/j.jmbbm.2018.01.010.

25. Tyler, C. A., Qin, J., Bates, F. S. & Morse, D. C. SCFT study of nonfrustrated ABC triblock copolymer melts. *Macromolecules* **40**, 4654–4668 (2007).

26. Widmaier, J. M. & Meyer, G. C. Glass Transition Temperature of Anionic Polyisoprene. *Rubber Chem. Technol.* **54**, 940–943 (1981).

27. Breiner, U., Krappe, U., Jakob, T., Abetz, V. & Stadler, R. Spheres on spheres - A novel spherical multiphase morphology in polystyrene-block-polybutadiene-block-poly(methyl methacrylate) triblock copolymers. *Polym. Bull.* **40**, 219–226 (1998).

28. Bailey, T. S. Morphological Behavior Spanning the Symmetric AB and ABC Block Copolymer States. (2001).

29. Qiao, Y. *et al.* Symmetric Poly(ethylene oxide- b -styrene- b -isoprene) Triblock Copolymers: Synthesis, Characterization, and Self-Assembly in Bulk and Thin Film. *Macromolecules* **47**, 6373–6381 (2014).

30. Cochran, E. W., Morse, D. C. & Bates, F. S. Design of ABC Triblock Copolymers near the ODT with the Random Phase Approximation. *Macromolecules* **36**, 782-792 (2003).

31. Löbling, T. I. *et al.* Bulk morphologies of polystyrene-block-polybutadiene-block-poly(tert-butyl methacrylate) triblock terpolymers. *Polymer.* **72**, 479–489 (2015).

32. May, A. W. Functional Nanostructured Ionic Liquid-based Block Copolymer Systems For Energy Applications. (2021).

33. Hiemenz, P. C. & Lodge, T. P. *Polymer Chemistry*. (2007).

34. Fetters, L. J., Lohse, D. J., Richter, D., Witten, T. A. & Zirkel, A. Connection between Polymer Molecular Weight, Density, Chain Dimensions, and Melt Viscoelastic Properties. *Macromolecules* **27**, 4639–4647 (1994).

CHAPTER 4: UNDERSTANDING STRUCTURE-PROPERTY RELATIONSHIPS IN THE SIOIS HYDROGEL THROUGH MODIFICATION OF POLYMER PROCESSING METHOD AND PS BLOCK SIZE

4.1 Chapter Summary

In this chapter, the effect of processing method and polystyrene block size on the mechanical properties of the SIOIS hydrogel was investigated as a way to further understand and optimize the structure property relationships of the SIOIS hydrogel studied in Chapter 3. It was found that solvent casting the SIOIS polymer from chloroform facilitates microphase separation between the PS and PI blocks which does not occur in melt-pressed samples resulting in the solvent-cast SIOIS hydrogels having superior energy dissipation capabilities and better bulk toughness. Additionally, this study compared the properties of an SIOIS hydrogel with a PS block molecular weight of 10kDa and an SIOIS hydrogel with a PS block molecular weight of 17kDa. It was observed that the polymer self-assembly process in the $SIOIS_{17}$ hydrogel is too slow compared to the solvent evaporation rate. This results in the polymer microstructure being trapped in a nonequilibrium state with an larger ratio of looping crosslinks to bridging crosslinks between PS spheres. The relative decrease in the amount of bridging polymers causes a decrease in the modulus of the $SIOIS_{17}$ hydrogel compared to $SIOIS_{10}$.

4.2 Introduction

The basis of this dissertation was to design a hydrogel that is both fatigue-resistant and capable of dissipating energy within the network. Since 2010, the Bailey group has created and developed the process of making fatigue-resistant hydrogels through the formation of so-called “tethered micelles” as a way to distribute stress throughout the hydrogel network.[1] In chapter 3, a modification to a fatigue-

resistant hydrogel was detailed as a way to provide an energy dissipation mechanism to this tethered micelle network. The success of this tethered micelle hydrogel system, SIOIS, relied on a specific molecular design strategy: (1) the phase separation between the PS, PI, and PEO blocks to ensure the energy dissipation mechanism was available to the water and (2) the SIOIS coupled polymer spanning between multiple spheres to form the evenly-spaced physical crosslinks which provide fatigue resistance to the network just as had occurred in the SOS hydrogel.[2]

While the SIOIS hydrogel was made as a modification to the SOS hydrogel systems used by our group, adding a polymer block has dramatic effects on the self-assembly of the block polymer both in the actual microstructure formed and the periodicity of the structure as shown in Chapter 2. Therefore, it was important to understand how these changes in the microphase structure affected the mechanical properties of the hydrogel. The studies presented here started as investigations into challenges that arose by processing and charaterizing the SIOIS hydrogel in the same ways as the SOS hydrogel. These investigations became formalized studies which could provide insight about what is happening molecularly within the SIOIS hydrogel especially in ways that have not affected the SOS hydrogel. When the first SIOIS hydrogel was originally synthesized, melt processing was not successful in producing a hydrogel which exhibited the hysteresis in the compression cycle that would be expected of a polymer which is dissipating energy (Appendix C Figure C.1). We hypothesized that due to the small interaction parameter between the PS and PI blocks and the small PI molecular weight that it was possible that the PI was mixing with the PS and therefore was not available on the outside of the sphere to be pulled into the water as a way to dissipate energy. One of the parameters governing the self-assembly of block polymers is based on χN where χ is the interaction parameter governing the energy of mixing the two blocks and N is the number of monomer molecules in the chain which is discussed here as molecular weight.[3] As χN increases, the likelihood of microphase separation between two blocks also increases. Therefore since we could not change the interaction parameters between the two blocks, we hypothesized that increasing the molecular weight of the PS block would force phase separation between the two blocks. This larger PS size would also allow us to study how the size of the sphere affects the formation of the SIOIS hydrogel

spheres. Since the Bailey group first synthesized the block polymers for the SOS hydrogel, the PS block had always had a molecular weight around 8800g/mol[1,2,4] with no investigation into how changing the PS block size affects the formation of the tethered micelle network. We had previously made an SIOIS hydrogel using an PS-PI macroinitiator where the PS block was 7700 g/mol. However, the SIOIS hydrogel created from that macroinitiator was quite brittle and did not hold up to mechanical testing (Appendix C Figure C.2). We suspect that the PS spheres were not truly glassy in that hydrogel. The T_g of polystyrene is known to scale linearly with molecular weight up to around 10kDa in bulk polymer.[5] However, in the hydrogel, the PS is in individual domains rather than in the bulk while also being surrounded by a plasticizer in the form of the PI; therefore, the T_g is likely to be lower than expected in the bulk. Therefore, by increasing the molecular weight of the PS block, we were also able to test how much of an increase was necessary for the PS spheres to be glassy. While the morphological development of a general AB sphere morphology has been studied,[6,7] the lack of experimental data for the ABC sphere morphologies results in a gap in understanding how the sphere morphology develops when there is an additional block that must be accounted for during mixing especially when the polymers have very large molecular weights.

During the course of processing these higher molecular weight PS samples, solvent-casting was tested as a method for developing the sphere morphology in place of melt-processing. Solvent casting is a method of polymer processing where the polymer is fully dissolved in solvent and slowly dried over days or weeks.[8–10] In the solvent, polymer chains are free to move and arrange within favorable interaction parameters depending on the choice of solvent and its miscibility with each block. In the solvent, the polymer chains have a much larger freedom of movement as the solvent lowers the Tg of the polymer chains, so they are not inhibited by entanglements as in the melt. When the solvent is neutral to the polymer chain, the blocks are mixing evenly; however, any slight selectivity of a solvent to a one polymer block over another will result in that immiscible block collapsing into itself. Then, as the solvent slowly evaporates, the concentration of the solvent is very low at the surface of the hydrogel resulting in the blocks being forced to mix and microphase separating in small sections at the surface of the hydrogel. The

solvent evaporation must be slow enough to allow the polymer chains enough time to self-assemble into their preferred equilibrium state. If the time is not long enough, one risks "freezing" the non-equilibrium state of the assembling polymers. As the solvent is evaporated, the T_g of the polymer increases and the PS spheres become glassy. Because such a small number of chains are microphase separating, there is a much smaller number of defects and the polymer has the ability to move more freely to form more highly segregated structures to minimize the interfacial contact between the blocks.[9] While solvent-casting is typically used to make thin films, it can also be useful for promoting phase separation in bulk polymer.[11,12]

The first part of this chapter examines the challenges in the SIOIS hydrogel which led to the study of how different polymer processing methods affect the mechanical properties of the hydrogel. Then, this chapter compares the mechanical properties of the two hydrogels with different PS molecular weights when processed similarly. These studies work together to provide some exploration into the structure-property relationships of the SIOIS hydrogel and how best to obtimize the mechanical properties of the hydrogel by targeting the molecular level of the polymer.

4.3 Results and Discussion

4.3.1 Initial Hydrogel Formation

Two SIOIS systems were synthesized for this study as a way to test our hypothesis that a larger PS sphere would allow better phase separation between the PS and PI blocks and how sphere size affects hydrogel formation. Therefore, two different polymer systems were made: $SIOIS_{10}$ and $SIOIS_{17}$ where the 10 and 17 refer to the average molecular weight of the PS block in each system. The process for the synthesis of $SIOIS_{10}$ was detailed in chapter 3. $SIOIS_{17}$ was synthesized using the similar anionic polymerization method as $SIOIS_{10}$ through three steps: synthesis of PS-PI macroinitiator, synthesis of PS-

Table 4.1: Molecular weight of each block calculated using end-group analysis from ^{1}H-NMR. Volume fractions were calculated using molecular weight and average polymer density at 140°C.[13] Coupling percentage was calculated from GPC shown in Figure 1.

Polymer	S Mn (g/mol)	B/I Mn (g/mol)	O Mn (g/mol)	Total Mn (g/mol)	f_S	$f_{B/I}$	f_O	Coupling Percentage	SC Sphere Radius (nm)
SI_{10}	10200	2800	-	13000	0.757	0.243	-	-	-
SIO_{10}	10200	2800	102300	115300	0.096	0.031	0.874	-	-
$SIOIS_{10}$	20400	5600	204600	230600	0.096	0.031	0.874	44% SIOIS	13.99
SI_{17}	17200	4100	-	21300	0.781	0.220	-	-	-
$SIOIS_{17}$	17200	4100	172500	193800	0.096	0.027	0.877	-	-
$SIOIS_{17}$	34400	8200	345500	387600	0.096	0.027	0.877	46% SIOIS	21.15

PI-PEO, and finally coupling of PS-PI-PEO to make a blend of PS-PI-PEO-PI-PS and PS-PI-PEO. The molecular weights for the $SIOIS_{17}$ hydrogel were chosen so that the PS molecular weight was at least 50% larger than the PS molecular weight for $SIOIS_{10.}$ The PI and PEO molecular weights were targeted to allow for similar volume fractions[13] between the three blocks as in the $SIOIS_{10}$ polymer (Table 4.1). DSC of the SIO_{10} and SIO_{17} polymer does not show the PS glass transition to be at room temperature. Howver, in the SIO polymers, the T_g of PS is mainly covered by the much larger PEO crystallization peak. (Appendix C Figures C.6). To form the hydrogels, the SIO polymers were coupled and then blended with the necessary amount of corresponding SIO polymer so that they have similar coupling percentages to allow for comparison of the swelling ratios and mechanical properties in compression and tensile testing. GPC was used to determine whether the correct percentage of uncoupled to coupled polymer was achieved during blending (Fig 4.1). The $SIOIS_{10}$ polymer has the high molecular weight contaminant that was determined by May[14] to be caused by coupling of excess PEO which is formed when the SIO synthesis is not sufficiently dilute. This high molecular weight contaminant is observed as a large molecular weight shoulder in the GPC, but this shoulder is excluded when the coupling percentage is calculated.

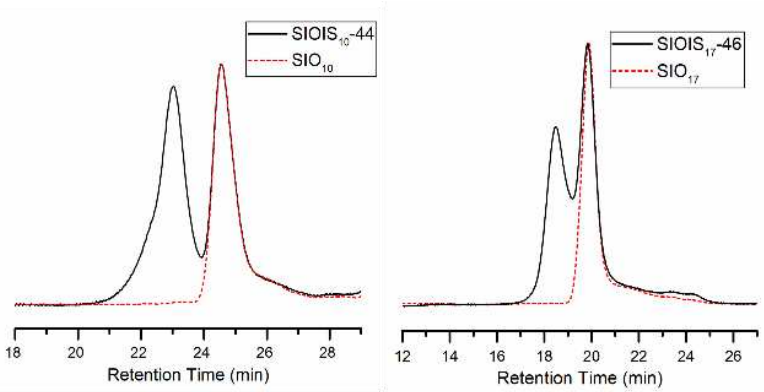

Figure 4.1: Size exclusion chromatography of SIOIS10 and SIOIS17. The black lines indictate the coupled polymer SIOIS and the red dashed lines indicate the original SIO polymer before coupling. The numbers in the name indicate the amount of SIOIS present in each SIOIS blend. SIOIS 17 is 44% SIOIS and 56% SIO and SIOIS17 is composed of 46% SIOIS and 54% SIO.

Once coupled, the SIOIS polymers were pressed in a mold at 150°C for 20 minutes then swollen in DI water for 24 hours. The resulting hydrogels were then subjected to a preliminary study of the compression stress-strain curves for each gel. The $SIOIS_{10}$ hydrogel has a similar compressive modulus to the SOS hydrogel discussed in Chapter 3 (Appendix C C.1), but has less hysteresis between the loading and unloading cycles than the SOS hydrogel. The $SIOIS_{17}$ hydrogel has a much lower compressive modulus than both the SOS and SIOIS hydrogels even with a similar coupling percentage to both samples. Images of these melt-pressed gels show that while $SIOIS_{10}$ looks transparent similar to the SOS hydrogel, $SIOIS_{17}$ has opaque sections. We hypothesized that this opacity was caused by sections of the hydrogel not phase separating into the sphere morphology during melt processing to allow solvation with the water. As detailed in Chapter 2, the large molecular weights that are necessary to form spheres with these polymers can often lead to slow kinetics resulting in polymers which are not fully microphase separated. The molecular weight of the $SIOIS_{17}$ hydrogel was much larger than any hydrogel we had made previously. We hypothesized that the total polymer molecular weights necessary to increase the PS block molecular weight while still maintaining the volume fractions resulted in a polymer that was not completely phase separating during the melt-processing time. However, long processing times (>30) resulted in degradation of the polymer.

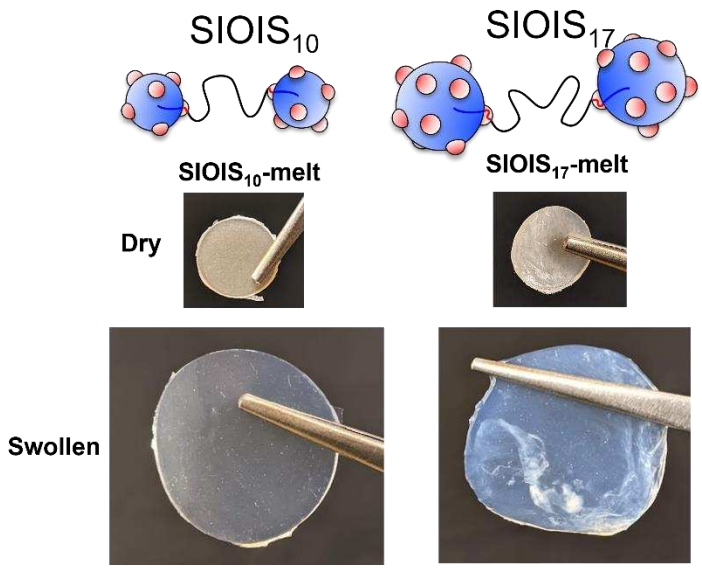

Figure 4.2: Schematic depictions of the SIOIS10 polymer and the SIOIS17 polymer chain. Images of the melt-processed SIOIS10 and SIOIS17 hydrogels while dry and swollen with water. Opaque sections can be seen in the SIOIS17 swollen sample.

4.3.2 Solvent Casting

Solvent-casting was used to process the polymers as a way to overcome the slow kinetics of these large polymers in the melt. A schematic depiction of the solvent-casting process is shown in Figure 3.4. The SIO/SIOIS polymer was dissolved in 1%w/v chloroform and allowed for the solvent to completely evaporate, usually around 7 days. Samples were then dried under room temperature vacuum for 2 hours to ensure all solvent was removed before being placed in DI water for 24 hours. After solvent casting, the samples were then placed in DI water for 24 hours. It took some experimentation for the solvent casting method to be finalized. Consideration of the choice of solvent included choosing a solvent in which all three blocks were soluble but is not so selective to one block as to cause the formation of a non-equilibrium morphology. Solvent casting is often used to form morphologies that are metastable[15–17] by choosing solvents that are selectively more soluble to specific blocks especially to change the stucture of the sphere. While some of the microspheres formed by this method such as the "spheres on spheres morphology" would still allow the PI block to access the water matrix during mechanical loading, our goal was to come as close to an equilibrium state as possible so that it could be compared with SOS which was being formed in the melt. However, having a polymer with three unique blocks complicates

the choice of a completely neutral solvent. Toluene and THF were tested as potential solvents. However, the hydrogel formed from the THF-cast polymer was quite brittle and broke into pieces of swollen polymer while in water. The toluene-cast gel did not swell at all and broke apart before being placed in the water (Appendix C Figure C.11). Chloroform was ultimately chosen as the solvent because it was able to dissolve all three blocks. Chloroform also is a slightly better solvent for PS than for PI[11,12] which causes the PS to be more solvated than the PI block resulting in better phase separation between the two blocks. Therefore, even though our goal was to find a neutral solvent, we believed this selectivity would benefit the goal of microphase separation between PS and PI. The main drawback to using chloroform is that the chloroform can become trapped within the PEO chains. Therefore, each sample was dried under vacuum at room temperature for 2 hours. Additionally, ^{1}H-NMR of the polymers using toluene-d8 as the solvent showed no chloroform remaining in the sample (Appendix C Figure C.10). While temperature annealing under vacuum is often applied to the dry solvent-cast polymer, we found that this degraded the polymer sample even with short (2 hour) anneal times.

The concentration of the solvent cast solution and the volume of solvent used was important during testing as too little polymer in solution resulted in polymer samples that, once swollen, were too thin for accurate compression and tensile testing. Additionally, due to the use of high sided containers as the solvent-casting "mold", if the volume of the solution was too high, the polymer formed would be cup-shaped with thick sides and a thin bottom. Decreasing the volume of the polymer solution still does result in a slight rise in the edges of the polymer as can be seen in Figure 4.5, but the base of the hydrogel has a more evenly distributed thickness.

Images of the swollen gels processed through solvent casting show that both the $SIOIS_{10}$ and $SIOIS_{17}$ are transparent after swelling when processed using solvent-casting (Figure 4.3). Swelling ratios in Figure 2b show that the melt-processed samples for $SIOIS_{10}$ swelled less than the solvent-cast sample while the swelling for the solvent cast and melt-pressed samples for $SIOIS_{17}$ were within the range of error. Overall, the $SIOIS_{10}$ hydrogel swelled less than the $SIOIS_{17}$ hydrogel despite having a higher coupling percentage.

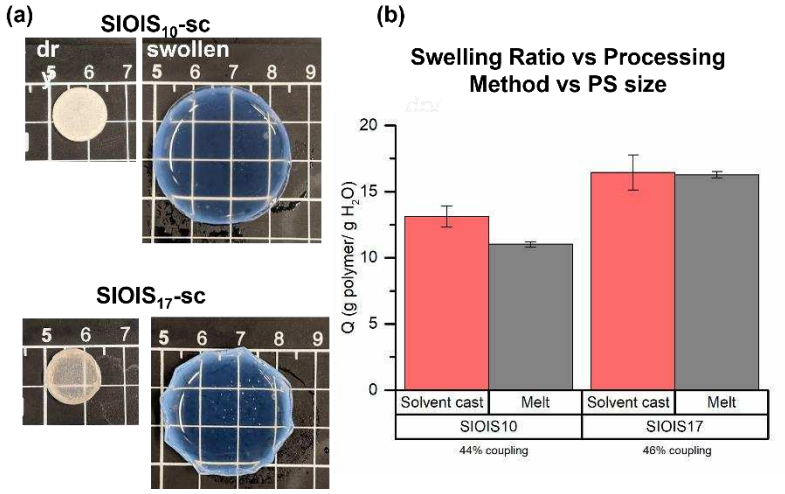

Figure 4.3: (a) Images of solvent cast(sc) SIOIS10 and SIOIS17 hydrogels when dry and when swollen. (b) Average swelling ratios of solvent cast and melt processed hydrogels of SIOIS10 and SIOIS17.

4.3.3 SAXS

To ensure the formation of sphere morphology in all the SIOIS systems, small angle X-ray scattering (SAXS) was performed on each coupled polymer sample while dry (Figure 4.4). The melt-pressed samples were heated to 150°C for 1 hour before cooling to 100°C where the scattering was collected while the solvent-cast samples were heated to 100°C for one hour to ensure the PEO was not crystalline in the sample. The melt and solvent cast samples for both $SIOIS_{10}$ and $SIOIS_{17}$ all formed a liquid-like packing of spheres. This morphology is shown in the SAXS by the presence a principal scattering peak which indicates that microphase separation is occurring between the polymer blocks. However, the samples do not have the sharp resolutions at the scattering reflections expected for a BCC morphology. Instead, broad peaks are observed which is indicative of the general formation of spheres not situated in a periodic structure. This is expected due to the large molecular weights of the SIO polymers which are then doubled when the polymer is coupled. SAXS is only able to show the phase separation into the sphere morphology but is not able to determine the microstructure formed within the sphere by the PS and PI. Therefore, TEM would allow us to observe the phase separation in the sphere but has not been feasible due to the large molecular weights of the polymers. The size of the spheres formed can be

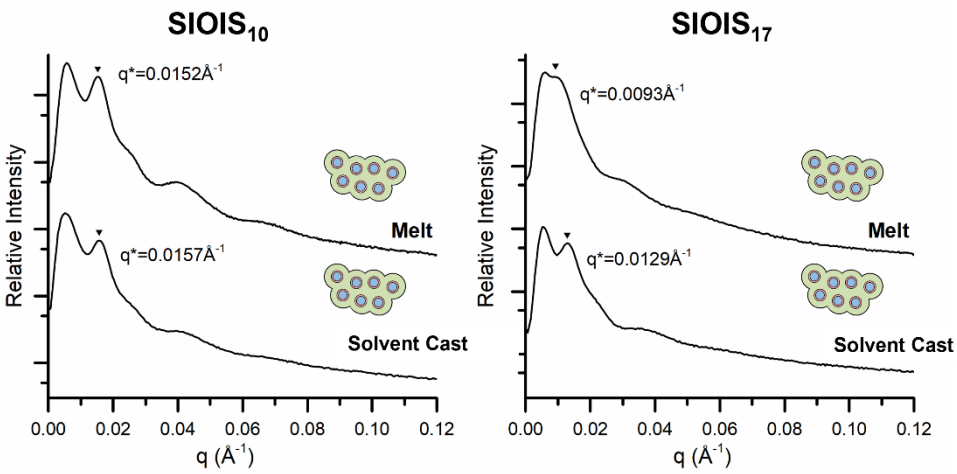

Figure 4.4: Small-angle X-ray scattering (SAXS) of solvent cast and melt processed samples of SIOIS10 and SIOIS17. All samples formed a liquid-like packing of spheres. The principal scattering peak is denoted with the black arrow and the q value is given.

determined using the inverse relationship between the principal scattering peak(q*) and the domain spacing in the morphology. This calculation assumes a BCC structure but is useful for giving an estimation of the average sizes of the spheres. The estimated radii of the spheres are shown in Table 1. The calculations for determining sphere size are shown in Appendix D. The spheres in the $SIOIS_{10}$ polymer are roughly the same size whether processed by melt or by solvent casting. In the $SIOIS_{17}$ polymer system, the polymer processed in the melt had significantly larger spheres than those formed in the polymer processed by solvent-casting. The $SIOIS_{10}$ had much smaller spheres than the $SIOIS_{17}$ polymer which is expected due to the differences in the molecular weights of the sphere-forming PS and PI blocks. This agrees with the literature expectation that the larger molecular weight samples will result in larger domains of spheres and therefore larger overall spheres.[18]

4.3.4 Compression Testing

SIOIS$_{10}$ and SIOIS$_{17}$ systems were subjected to cyclic compression testing up to 40% strain to test how the fatigue-resistant network and energy dissipation mechanism are affected by the changes in the sphere size and the processing method. The SIOIS$_{10}$ polymers processed in the melt had an average higher compressive modulus but was within the standard deviation of the solvent cast sample (Figure 4.5a). However, the SIOIS$_{10}$ solvent cast sample has a significantly larger amount of hysteresis between the loading and unloading cycles during compression. This hysteresis translates to a larger amount of energy dissipated by the solvent cast sample compared to the melt sample. Similarly in the SIOIS$_{17}$ samples, the solvent cast sample has a much larger hysteresis loop between the loading and unloading curves; however, the melt sample in the SIOIS$_{17}$ samples also has a lower average compressive modulus than the

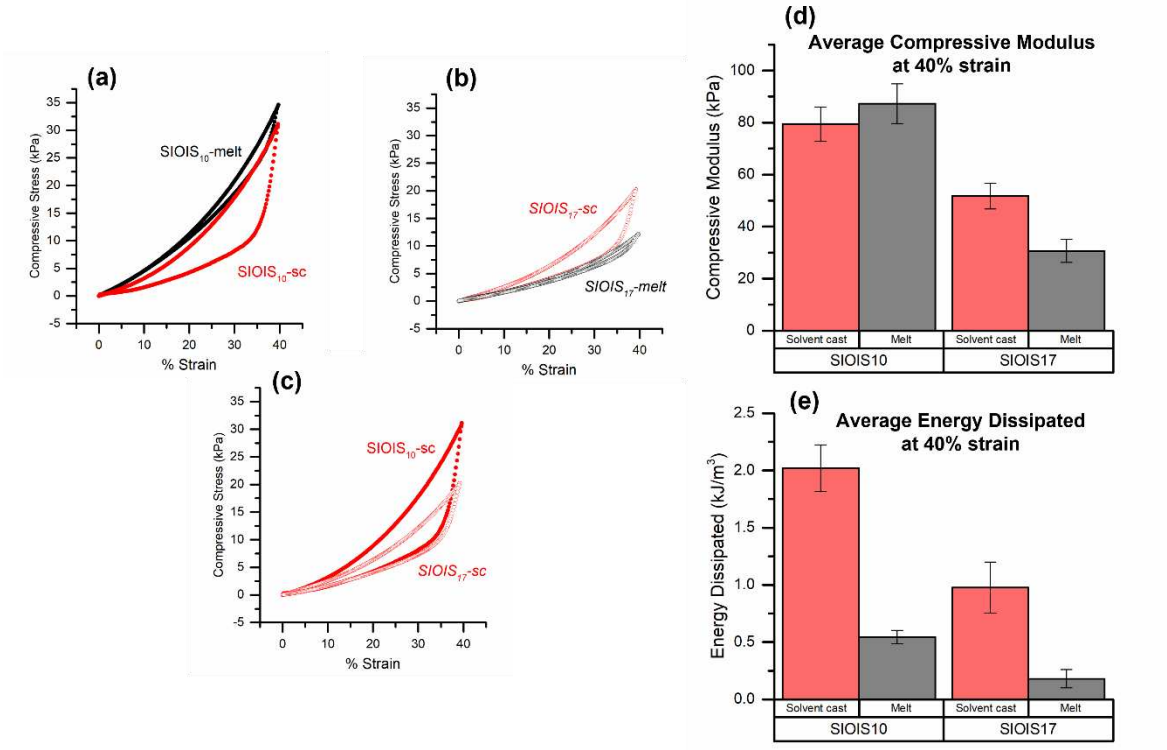

Figure 4.5: (a) Average stress-strain curves of compression cycles of SIOIS$_{10}$ hydrogels made by melt-processing(black) and by solvent-casting(red). (b) Average stress-strain curves of compression cycles of SIOIS$_{10}$ hydrogels made by melt-processing(black) and by solvent-casting(red). (c) Average stress-strain curves of compression cycles of SIOIS$_{10}$ (closed) and SIOIS17 (open) hydrogels. (d) Average compressive modulus taken at 40% strain of the SIOIS10 and SIOIS17 hydrogels processed by solvent-casting(red) and melt-processing(grey). (e) Average energy dissipated by a single compression cycle compressed to 40% strain of the SIOIS10 and SIOIS17 hydrogels processed by solvent-casting(red) and melt-processing(grey).

solvent cast sample (Figure 4.5b). However, even after the solvent casting, the SIOIS-17 hydrogel has a smaller modulus and less energy dissipated(Figure 4.5c) than the SIOIS-10 hydrogel as shown in Figures 4.5 d and e.

Compression tests of 6 successive cycles on one sample was completed to study the recovery properties of just the solvent cast polymers for $SIOIS_{10}$ and $SIOIS_{17}$. Figure 4.6 shows that the $SIOIS_{10}$-sc and the $SIOIS_{17}$-melt samples have nearly no decrease in the modulus and no change in the amount of hysteresis between each cycle. The $SIOIS_{17}$-sc sample, however, has a decrease in the modulus throughout all of the 6 cycles where the black curve is the 1st cycle and the orange curve is the final cycle. A slight decrease in the hysteresis between the loading curves is also observed. Because the overall area of the curve is decreasing rather than just the modulus, it seems possible that the change in the compression cycle is due to a slow recovery of the hydrogel network rather than permanent fatigue. This suggests that 10% strain/sec is the recovery rate limit for this specific hydrogel.

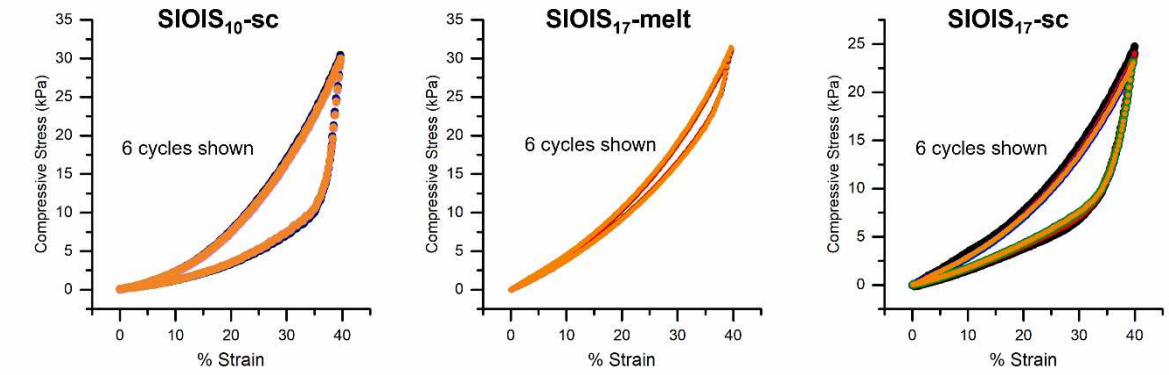

Figure 4.6: Stress-strain curves showing 6 overlaid compression cycles to 40% strain for a single sample each of an $SIOIS_{10}$ solvent cast hydrogel, a $SIOIS_{17}$ melt processed hydrogel, and a $SIOIS_{17}$ solvent cast polymer. The $SIOIS_{17}$ solvent cast hydrogel shows a loss of modulus and hysteresis over the 6 cycles.

4.3.5 Tensile testing

Uniaxial tensile testing was performed to break on the two SIOIS polymer systems as shown in Figure 4.7. For $SIOIS_{10}$ and $SIOIS_{17}$, all of the solvent cast samples had a higher strain at break and stress at break than the melt pressed samples (Figures 7a and 7b). The melt-pressed samples for both systems also had nearly the sample modulus as the solvent cast samples until break. When comparing the two hydrogel systems with different PS sizes, the $SIOIS_{10}$ had a much larger stress at break, but the $SIOIS_{17}$

had only slightly smaller average strain at break. Additionally, the modulus of the $SIOIS_{17}$ samples was much lower than the $SIOIS_{10}$ samples (Figure 4.7c). Only two tensile tests were able to be completed for the $SIOIS_{17}$-SC samples because the small modulus made it difficult for the instrument to grip the samples without breaking them before the test began. Overall, the $SIOIS_{10}$-sc hydrogel had a much larger average bulk toughness than any of the other gels (Figure 4.7d).

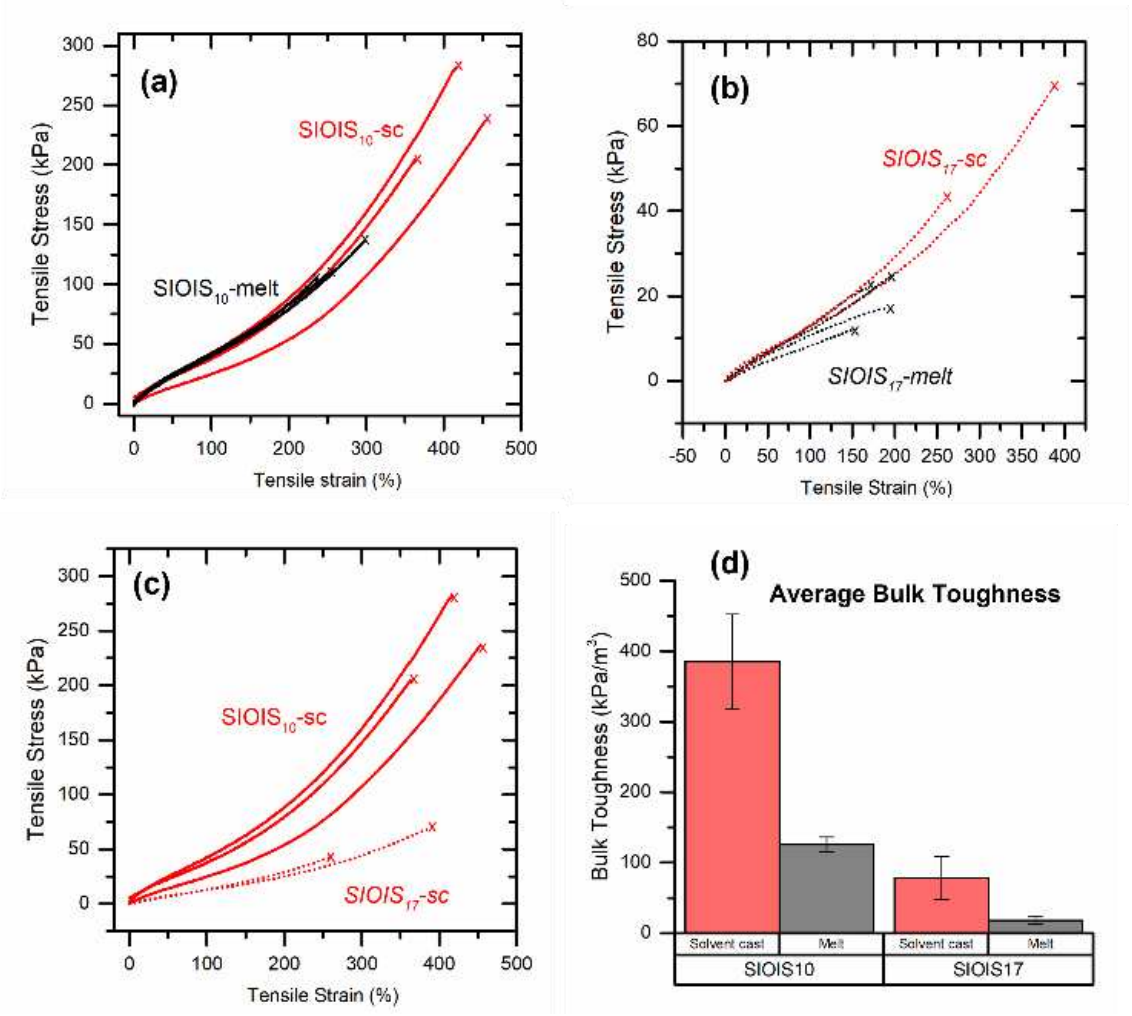

Figure 4.7: (a) Stress-strain curves showing tensile tests to break of $SIOIS_{10}$ hydrogels made by melt-processing(black) and by solvent-casting(red). (b) Stress-strain curves showing tensile tests to break of $SIOIS_{17}$ hydrogels made by melt-processing(black) and by solvent-casting(red). (c) Stress-strain curves showing tensile tests to break of $SIOIS_{10}$ (closed) and $SIOIS_{17}$ (open) hydrogels. (d) Average bulk toughness of the $SIOIS_{10}$ and $SIOIS_{17}$ hydrogels made by solvent-casting(red) and melt-processing(grey).

4.3.6 Impact of Polymer Processing on Sphere Formation

We had originally attempted solvent casting as a method for compatibilizing the polymer blocks which would promote phase separation between the PS and PI blocks and to remove kinetic barriers inherent in processing large molecular weight polymers. The benefits of processing the polymer through solvent-casting are confirmed when comparing mechanical properties of the melt pressed samples and the solvent cast samples of both of the SIOIS systems. The solvent cast systems performed much better in both compression and tensile testing than the melt pressed samples for both $SIOIS_{10}$ and $SIOIS_{17}$. Both $SIOIS_{10}$-sc and $SIOIS_{17}$-sc had larger amounts of energy dissipated during compression cycles than the melt pressed samples and were able to be stretched to larger strains during tensile testing than the melt-pressed samples resulting in a larger bulk toughness for the solvent cast gels. The energy dissipation in the SIOIS hydrogel comes from the forced stretching of the hydrophobic PI block into the water when the PEO block is sufficiently stressed. Therefore, the lack of hysteresis, and consequently the lack of energy dissipation, in the melt pressed samples indicates that in the melt-pressed polymer samples the PI block is not accessible at the sphere/water junction to be pulled into the water when needed. In the tensile testing, the melt pressed samples have a much smaller strain at break similar to the SOS hydrogel without the rubbery PI block because the PI block is not acting as a flexible junction between the glassy sphere and the PEO chain like it is in the solvent-cast samples. This flexible junction likely allows the polymer chain to better distribute the stress concentration at the junction even if the B block is not pulled into the water matrix. However, in the melt-processed system, the inaccessibility of the PI block is likely caused by a lack of phase separation between the PS and the PI blocks in the sphere which traps the PI within the sphere either in too short of chain lengths to allow stretching into the water matrix or PI chains are highly entangled with the PS to not allow movement. SAXS shows that the spheres are forming, but does not give insight into the microphase separation or lack of microphase separation within the sphere. It could be possible that when processed in the melt, the spheres are disordered mixes of PS and PI. Spheres processed through solvent casting likely form the spheres-on-spheres morphology discussed in Chapter 3

(Figure 4.8) due to the small volume fraction ratio of PI to PS and the frustration experienced within the interaction parameters of the blocks.[19]

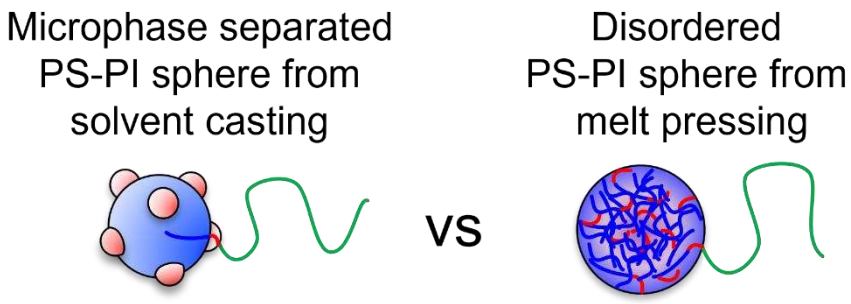

Figure 4.8: Schematic representation of a sphere-forming SIO chain where the PS and PI are microphase separated into the "spheres on spheres" morphology when processed by solvent-casting and a schematic representation of a sphere-forming SIO chain where the PS and PI blocks are in a mixed and disordered state within the sphere. Blue chains represent PS, red chains represent PI and green chains represent uncoupled PEO.

The lack of phase separation in the melt-processed SIOIS gels is likely caused by the small interaction parameter between the PS and PI blocks and the small PI volume fraction which are minimizing the enthalpic penalty of contact between the two blocks. This lack of phase separation is likely exasperated by the larger molecular weights of the SI polymers and the large X values associated with mixing PI and PEO. In the melt, for sharp PS/PI and PI/PEO interfaces to form, the PS-PI blocks must diffuse through PEO in order to rearrange the spheres and achieve the uniform stretching that is ensured by a strongly segregated microstructure.[20] Its likely that the large interaction parameter between the PI and PEO blocks means that this diffusion between spheres is not a thermodynamically favorable process even though the end result of a highly segregated morphology is thermodynamically favorable. While chain exchange dynamics have been studied in AB polymers,[6,20,21] similar studies have not been completed for ABC polymers in the melt. Furthermore, the large molecular weight differences between the sphere blocks and PEO matrix block makes this a slow kinetic process especially because there are sphere-forming blocks on both sides of the polymer chain. The resulting morphology is a disordered sphere of PS and PI chains where the PI is so entangled within the PS that it is not able to be pulled out of the sphere without breaking. Additionally, this disordered sphere morphology also results in PS spheres with a plasticizing polymer distributed within the typically glassy PS. It is likely that there are pockets of

the sphere that are not fully glassy; however, because the modulus of the polymer does not decrease in the SIOIS10-melt hydrogel, it's likely that there are enough glassy sections of the PS to maintain the physical crosslinks of the network despite the lack of phase separation between the PS and the PI. However, over time, stress relaxation within the non-glassy chain entanglements would result in the dissolution of the spheres and the hydrogel as a whole.

Ultimately, solvent-casting allows the polymer chains a better freedom of movement during microphase separation resulting in a microphase separated sphere with PI sections accessible to the water/PEO matrix during mechanical testing. PS and PEO have good selectivity for chloroform compared to PI which allows for better phase separation between the PS and PI blocks when the PI is already microphase separating in solution. The chains are able to move freely within solution without entanglements. As the solvent evaporates, the small layer of the SIOIS polymer is able to microphase separate through chain diffusion in the highly concentrated solution at the surface of the polymer solution. While the polymer is more concentrated than in free solution, entanglements are minimized due to the small area of microphase separation and PI blocks are likely already minimally phase separated from the PS. Additionally, the long processing times ensures enough time for equilibrium chain exchange to occur. As explored in chapter 3, the size of the spheres as calculated from SAXS likely results in glassy PS spheres which have small PI spheres attached to the surface of the larger PS as a way to limit chain stretching.[19] In this "spheres on spheres" morphology accessed through solvent-casting, the PI block is not excessively tangled with the PS block and is accessible to be pulled into the water/PEO matrix as a way to dissipate energy.

In the $SIOIS_{10}$ hydrogel, the formation of the overall tethered micelle network does not seem to be affected by the processing method. The swelling ratios and moduli between the solvent cast and melt-pressed samples in $SIOIS_{10}$ are similar. Because these properties are regulated by the crosslink density in the polymer network, the similar values between the solvent-cast and melt-pressed hydrogels indicate that similar amounts of crosslinks exist in a well-organized network in both systems. Because the tethered micelle network remains in tact, the $SIOIS_{10}$-sc hydrogel maintains the fatigue-resistant properties

expected from the tethered micelle network which is seen by the lack of significant change in the modulus or energy dissipation during multiple cycles of compression testsing. Alternatively, in $SIOIS_{17}$, the melt-pressed samples had a lower modulus than the solvent-cast samples and the melt samples observed nearly no change in the modulus during multiple cycles of compression testing while changes in the mechanical properties of the the solvent cast sample were observed. Therefore, solvent casting in the $SIOIS_{17}$ hydrogel must be changing the tethered micelle network. This will be discussed in the next section.

While solvent casting is useful for forcing microphase separation between the PS and the PI blocks, it is not an ideal solution for the long-term processing of a polymer that has mechanical applications. Solvent casting is very sensitive to the evaporation rate, substrate, solution concentration, and solvent choice. Additionally, many applications require specific sizes of samples for testing which are much larger than our current testing setup. Making larger solvent cast samples is much more difficult due to the necessity of finding a mold the correct size, longer wait times for evaporation, and uneven evaporation over a larger area. These problems result in less than ideal sample to sample replicability which is crucial to scaling the impact of the SIOIS hydrogel system. Instead of the using the PS block to increase the χN value between the PS and PI blocks, we could increase the molecular weight of the PI block. The increase in the PI molecular weight could force the phase separate between the PS and PI block and would have the potential benefit of providing a larger energy dissipation mechanism and larger flexible junction to the hydrogel. However, the larger PI block would require a larger total polymer molecular weight which could result in similar issues of slow kinetics during phase separation as seen in Chapter 2.

4.3.7 Impact of PS molecular weight on Mechanical Properties

The $SIOIS_{17}$ hydrogels were synthesized with the goal of a larger PS block thermodynamically forcing the phase separation of PS and PI blocks and also ensuring the presence of a high glass transition temperature in the PS block. While the phase separation problem seems to have been fixed by using a

solvent-processing method, the presence of the larger PS sphere is still useful for understanding how the sphere size affects the energy dissipation mechanism and the fatigue-resistant network.

While the solvent cast samples for both $SIOIS_{10}$ and $SIOIS_{17}$ dissipated more energy and had a larger bulk toughness than their melt processed counterparts, the $SIOIS_{10}$-sc also dissipated 2.1x times more energy and had and 4.9x larger bulk toughness than the $SIOIS_{17}$-sc hydrogel. Additionally, the $SIOIS_{10}$-sc hydrogel had a larger modulus than the $SIOIS_{17}$ hydrogel under both tensile strain and compressive strain despite the $SIOIS_{17}$-sc having a larger coupling percentage. In our SOS hydrogels, the modulus has been shown to correlate linearly with the swelling ratio of the polymer,[1] and we do observe that the swelling ratio of the $SIOIS_{10}$ polymer was smaller than the $SIOIS_{17}$ hydrogel.

In a basic hydrogel, the larger coupling percentage should result in more crosslinks within the network and therefore a smaller swelling ratio.[22]. However, the larger molecular weight of the $SIOIS_{17}$ polymer results in a larger network as observed from the domain spacing calculted from the SAXS principal scattering peak where the distance between the spheres is much larger than in $SIOIS_{10}$. This larger distance between crosslinks when the midblock molecular weight increases has been observed in ABA polymers due to the increase in the elasticity of the PEO midblock.[23–25] This larger distance between spheres would results in a larger amount of water than can be imbibed by the polymer network resulting in a larger swelling ratio. However, the decrease in the modulus observed in the $SIOIS_{17}$ hydrogel

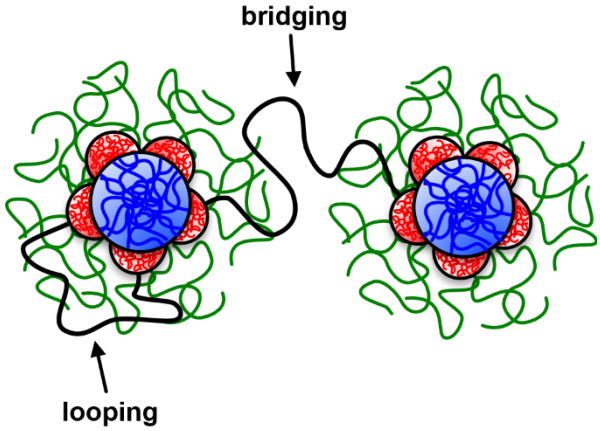

Figure 4.9: Schematic representation of looping SIOIS chains and bridging SIOIS chains. Blue chains represent PS, red chains represent PI, green chains represent uncoupled PEO chains, and black chains represent coupled PEO chains.

suggests that there are fewer overall crosslinks in the network, not just a larger amount of swelling. We hypothesize that this large distance between spheres is resulting in SIOIS polymer chains looping into their own sphere rather than bridging between PS-PI spheres (Figure 4.9).

Some percentage of chains (25-30%) looping is expected in ABA block polymer systems that form spheres.[25] When the number of chains that are looping chains increases, there are fewer crosslinks in the network leading to a larger swelling ratio and a lower modulus. While definitive reasons for the looping are not fully understood in the literature, we do know that morphologies are formed as a way to limit interfacial contact between immiscible blocks such as PI and PEO through a swapping of chains until an equilibrium morphology is formed. However, the chain dynamics of morphology formation have shown that it is often not thermodynamically favorable for these immiscible blocks to move through the PEO matrix to find a new PS sphere especially in the large and hydrophobic SI block of an $SIOIS_{17}$ chain.[6,20] Instead of traversing the large distance through an immiscible block, we hypothesize that the SI spheres are constantly "fusing" together into a large sphere to complete chain exchange before breaking apart similar to what occurs during chain exchange in block copolymer micelle solutions.[26,27] This fusing and splitting mechanism happens multiple times during the microphase separation process until the equilibrium sphere network is formed. These loops are likely trapped non-equilibrium morphology spheres which had not been given sufficient time to equilibrate into the expected sphere morphology with the lower percentage of looping chains.

Even solvent casting does not eliminate this issue. Solvent-casting has been used to enhance phase separation between large molecular weight polymers because it allows polymers to move more freely before chain exchange starts to occur due to a much less concentrated polymer than when the chains are in the melt. The resulting microphase separation only occurs at the much smaller highly concentrated surface of the solvent cast polymer. However, the solvent evaporation must be slow enough to allow chain exchange to occur without trapping the polymer in a non-equilibrium state. It is likely that in the $SIOIS_{17}$ hydrogel, the polymer chains are too long and are being trapped in spheres which are not at the equilibrium state. While slowing the evaporation rate of the solvent is possible, it would also be

possible to instead use a mixture of solvents for casting such as including a small amount of solvent that is selective towards PEO and slightly immiscible with PS such as water with a small percentage of THF.[28,29] The goal would be for the PS to begin to self-assemble while in the solvent to speed up the chain exchange process.

The change in the crosslink density in the $SIOIS_{17}$ polymer also affects the fatigue-resistant properties of the network. Because the ratio of looping to bridging polymer chains is not kept constant as might occur in an SIOIS hydrogel with a purposefully smaller coupling percentage, the network does not have an even-distributed number of crosslinks. This unequal distribution of crosslinks does not distribute stress as efficiently throughout the network resulting in small areas of chain fracture observed through a decrease in the compressive modulus throughout multiple compression cycles (Figure 4.6). Overall, the larger distance between spheres in the $SIOIS_{17}$ therefore results in a lower modulus in the hydrogel and a susceptibility to fatigue within the network due to the potential for uneven chain lengths between crosslinks. In addition to the fatigue-resistant network, the energy dissipation mechanism seems to be also affected by the decrease in the crosslinks in the $SIOIS_{17}$ hydrogel. It is possible that due to entanglements of the looping chains, that the PI block of looping chains could still participate as part of the energy dissipation mechanism. The smaller modulus of the $SIOIS_{17}$-sc hydrogel will necessarily result in a smaller amount of energy dissipated because of a decrease in the area under the curve (Figure 4.5c). Ultimately, it is unclear how the energy dissipation mechanism is truly affected by the looping chains and whether the PS molecular weight is playing more of a role in the presence of the looping chains than simply creating a large total polymer molecular weight. Fracture resistance studies could give us more localized insight into the energy dissipation mechanism similarities between solvent cast $SIOIS_{10}$ and $SIOIS_{17}$ specifically at a crack tip point rather than studying the bulk toughness of the hydrogel which gives only a picture of toughness to failure in the entire hydrogel.

4.4 Conclusion

The studies included in this chapter were the result of attempts to optimize the SIOIS hydrogel by increasing the PS block size and to allow better phase separation and processing in these large polymer systems through solvent-casting. Ultimately, we found that solvent-casting is the superior processing method for both $SIOIS_{10}$ and $SIOIS_{17}$ due to the solvent facilitating microphase separation between the PS and PI blocks which ensured that the PI was accessible as an energy dissipation mechanism in the hydrogel networks. This phenomenon was observed through the increase in energy dissipation and overall bulk toughness observed in the solvent-cast samples compared to the melt processed samples. In contrast, we had hypothesized that increasing the PS block size would allow the PS spheres to have a higher T_g and better phase separation between the PS and PI. While the $SIOIS_{17}$ did experience the better phase separation through the benefits of the solvent-casting method, the large PS block resulted in a very large overall polymer molecular weight which was too slow to fully self-assemble even through solvent-casting. The $SIOIS_{17}$ hydrogel exhibited a lower modulus in both compression and tensile testing than the $SIOIS_{10}$-sc hydrogel despite having a larger coupling percentage which should translate to a larger crosslink density.

These studies confirmed our hypothesis about the importance of the PI block's accessibility to be pulled into the PEO/water matrix and to confirm that the crosslinks in the tethered micelle network are highly important to the mechanical properties of the SIOIS hydrogel. These conclusions show the need for further study into the formation of spheres by ABC polymers as both the processing method and the sphere size affected the mechanical properties of the hydrogel by impacting how the spheres formed. Further study into the formation of the ABC sphere morphology will be crucial to the use and processing of the SIOIS hydrogel on a larger scale.

4.5 Experimental

4.5.1 Materials

Styrene (99.5% for analysis, stabilized, Acros) and ethylene oxide (99.5%, compressed gas, Aldrich) were purified by vacuum distillation from dried dibutylmagnesium (1.0M solution in heptane, Aldrich) two times. 1,3-Butadiene (99+%, p-tert-butylcatechol inhibitor, Aldrich) and Isoprene (99%, p-tert-butylcatechol inhibitor, Aldrich) were purified by vacuum distillation from n-butyl lithium (1.6M solution in hexane) two times. Argon degassed cyclohexane (CHX) was purified by passing the solvent over activated alumina followed by Q-5-like supported copper catalyst (Glass Contour). Argon-degassed tetrahydrofuran (THF) was purified by passing the solvent over activated alumina. High-purity argon (99.998%, Airgas) was passed through additional oxygen and moisture traps prior to use. All chemical syntheses were carried out in a dry argon atmosphere using standard Schlenk line techniques.

4.5.2 Methods

Synthesis of PS-PI-OH Macroinitiator

Purified styrene monomer was added under argon to a stirring solution of sec-butyl lithium (1.3M solution in cyclohexane/hexane(92/8), Acros) and dry, air-free cyclohexane in a 1 L reaction vessel at 40°C. Stirring continued for approximately 8 hours. The reactor pressure was then reduced to approximately 1 psig. Purified isoprene was added to the reaction vessel slowly to ensure pressure did not rise above 10psig. The reaction was maintained at 40°C for 8 hours. At this time, purified ethylene oxide was added to the reactor and allowed to react for 24 hours. The reaction was terminated by direct addition of sparged acidic methanol. The polymer was rotovapped and precipitated in a 1:4 mixture of isopropanol and methanol (2 L total) to give a white solid. The polymer was dried under vacuum at room temperature for 48 hours.

Synthesis of PS-PI-PEO(SIO) Polymers

PS-PI-OH (1g) was dried overnight under vacuum in a 2L reaction vessel with a glass stirbar. The reactor was evacuated and backfilled with purified argon before the addition of approximately 1L of dry,

air-free THF. Concentrated potassium naphthalenide in dry, air-free THF was added to the polymer solution via cannula until a light green color persisted for at least 15 minutes. The temperature of the reaction mixture was raised to 40°C. A 1.5 molar excess of purified ethylene oxide was added under argon with vigorous stirring. Stirring was continued for no more than 24 hours. The reaction was terminated by direct addition of 0.1M hydrochloric acid in methanol. The polymer was rotovapped and precipitated into pentane to give a light yellow solid of PS-PI-PEO. The polymer was dried under vacuum at room temperature for 48 hours.

Coupling of PS-PI-PEO chains to make PS-PI-PEO-PI-PS:

PS-PI-PEO-OH(1g) was dried overnight under vacuum in a 500mL purification flask. The polymer was then dissolved in ~200mL of dry, air-free THF. Potassium napthalenide with a known concentration was added to the purification via air-free syringe until a light green color persisted for at least 20 minutes. A solution of α,α′-dibromo-p-xylene dissolved in THF was added to the flask via syringe pump (1mol DBX:2mol KNAP added) over the course of 8 hours. The next day, the polymer was precipitated into pentane and dried under vacuum at room temperature for 48 hours.

Hydrogel Processing and Fabrication

Melt pressed polymers were processed using a Carver Model CH manual hydraulic press using various stainless steel molds with FEP-coated Kapton FN (Dupont, 500FN131) and preheated aluminum plates on either side of the sample. The sample mold was filled with excess polymer, placed between the plates, placed under slight pressure (500lbs) and heated at 150°C for 20 minutes or until the pressed sample was clear while still warm. The sample was then removed from heat and allowed to come to room temperature. The polymer was then placed in DI water and sparged for 60 seconds to remove excess oxygen from the water. The sample was left to come to equilibrium for 24 hours before testing.

SIOIS polymer (0.1g) was placed into a glass 5 mL vial with a 3mm diameter base with 1mL of $CHCl_3$ and a small stirbar until the polymer was completely dissolved. After the polymer was dissolved, the stir bar was removed, and the open vial was covered in foil and placed into a vacuum holm that with the ChemCap partially open to air. The sample was left for 7 days to evaporate before opening. To ensure

complete evaporation of the $CHCl_3$, the sample was left under vacuum for 2 hours. ^{1}H-NMR with Toluene-d_8 as the solvent was used to confirm the absence of excess $CHCl_3$. The polymer was then placed in DI water and sparged for 60 seconds to remove excess oxygen from the water. The sample was left to come to equilibrium for 24 hours before testing. This solvent-casting method was adapted from the methods of Radlauer et.al.,[11,12] and Qiao, et.al. Swelling ratio calculations were completed with n-=5 for all samples.

GPC, NMR, and Thermal Analysis

Gel Permeation Chromatography was completed using a Viscotek RIMax system fitted with three 7.5 x 300 mm PolyPore (Agilent) columns in series, an Alltech external column oven set to 40 °C, and a Viscotek differential refractive index (RI) detector with sample concentrations of 2 mg mL^{-1} . Stabilized and degassed THF was used as the eluent and run time was 45 minutes for all samples. Mass percent of coupled polymer was calculated by taking the area under curve of each sample. For the SIOIS polymer, the high molecular weight contaminant was excluded from the area. ^{1}H NMR spectra were collected in $CDCl_3$ (unless otherwise stated) using a Bruker Advance NEO 400 MHz Spectrometer equipped with Prodigy BBFO cryo-probe (ns = 256, 10 s delay, 2.5sec acquisition time). Thermal analysis was performed on a TA Instruments TGA Q500 and Discovery DSC 2500.

SAXS

SAXS data were collected on a Rigaku S-Max 3000 High Brilliance 3 Pinhole SAXS system outfitted with a MicroMax-007HFM Rotating Anode (CuKβ), Confocal Max-FluxTM Optic, Gabriel Multiwire Area Detector and a Linkam thermal stage. Dry samples were subjected to a heating ramp from to 150°C at 10°C/sec and annealed for 1 hour. The sample was then cooled back to 100°C and data was collected for 1 hour. The crystallization of PEO below 70°C disrupts the polymer morphology, so it is not useful to characterize the polymers below 75°C. The melt processed SAXS samples were melt pressed at 150°C for 20 min and cooled to room temperature before being subjected to the temperature ramp. The

solvent-cast SAXS samples were taken directly into the temperature after solvent cast with no additional annealing step.

Compression Testing

Biaxial compression was performed on an TA Ares rheometer using a Peltier base attachment. The circular samples were punched out of a larger hydrogel to an 8mm diameter. The tests were done with the sample submerged underwater with the upper plate having a diameter of 25mm and a lower plate having a functionally infinite diameter. The samples were compressed at a strain rate of 10%strain/sec with no hold period between cycles. The data is the average of 5 samples of SIOIS and 6 cycles for each sample. Compressive Young's moduli were calculated by dividing the stress at a given strain by that strain. Energy dissipated was calculated by subtracting the area under the unloading curve from the area under the loading curve with the units corrected.

Tensile Testing

Tensile testing was completed on an Instron Model 4442 system fitted with pneumatic grips and a 50N load cell. A dogbone shape was punched out of the swollen hydrogel to use for testing with the resulting dogbone being on average 13.5mmx1mmx1.5mm. Once in the grips, the sample was pulled until a force of ~0.10N was observed to ensure that the hydrogel was fully engaged. Samples were strained at 10%strain/sec until break. For cyclic tensile testing, the sample was strained at 2%strain/sec up to 75% of the average strain at break for the polymer system. Bulk toughness was calculated by taking the area under the tensile curve with units corrected. For $SIOIS_{10}$-melt, n=2 and for $SIOIS_{17}$-melt, n=3. For $SIOIS_{10}$-sc, n=2 and for $SIOIS_{17}$-sc, n=3.

4.6 References

1. Guo, C. & Bailey, T. S. Highly distensible nanostructured elastic hydrogels from AB diblock and ABA triblock copolymer melt blends. *Soft Matter* **6**, 4807 (2010).

2. Lewis, J. T., Fischenich, K. M., Haut Donahue, T. L. & Bailey, T. S. Nanostructure-Driven Replication of Soft Tissue Biomechanics in a Thermoplastic Elastomer Hydrogel. *ACS Biomater. Sci. Eng.* **4**, 3854–3863 (2018).

3. Bates, F. S. Polymer-Polymer Phase Behavior. *Sci. New Ser.* **251**, 898–905 (1991).

4. Huq, N. A., Ekblad, J. R., Leonard, A. T., Scalfani, V. F. & Bailey, T. S. Phototunable Thermoplastic Elastomer Hydrogel Networks. *Macromolecules* **50**, 1331–1341 (2017).

5. Santangelo, P. G. & Roland, C. M. Molecular weight dependence of fragility in polystyrene. *Macromolecules* **31**, 4581–4585 (1998).

6. Ryu, C. Y. & Lodge, T. P. Thermodynamic stability and anisotropie fluctuations in the cylinder-to-sphere transition of a block copolymer. *Macromolecules* **32**, 7190–7201 (1999).

7. Dormidontova, E. E. & Lodge, T. P. The order-disorder transition and the disordered micelle regime in sphere-forming block copolymer melts. *Macromolecules* **34**, 9143–9155 (2001).

8. Sinturel, C., Vayer, M., Morris, M. & Hillmyer, M. A. Solvent vapor annealing of block polymer thin films. *Macromolecules* **46** 5399–5415 (2013).

9. Kim, S. H., Misner, M. J., Xu, T., Kimura, M. & Russell, T. P. Highly oriented and ordered arrays from block copolymers via solvent evaporation. *Adv. Mater.* **16**, 226–231 (2004).

10. Morris, M. A., Gartner, T. E. & Epps, T. H. Tuning Block Polymer Structure, Properties, and Processability for the Design of Efficient Nanostructured Materials Systems. *Macromol. Chem. Phys.* **218**, (2017).

11. Radlauer, M. R. *et al.* Morphological consequences of frustration in ABC triblock polymers. *Macromolecules* **50**, 446–458 (2017).

12. Qiao, Y. *et al.* Symmetric Poly(ethylene oxide- b -styrene- b -isoprene) Triblock Copolymers: Synthesis, Characterization, and Self-Assembly in Bulk and Thin Film. *Macromolecules* **47**, 6373–6381 (2014).

13. Fetters, L. J., Lohse, D. J., Richter, D., Witten, T. A. & Zirkel, A. Connection between Polymer Molecular Weight, Density, Chain Dimensions, and Melt Viscoelastic Properties. *Macromolecules* **27** 4639–4647 (1994).

14. May, A. W. Functional Nanostructured Ionic Liquid-based Block Copolymer Systems For Energy Applications. (2021).

15. Gil Haenelt, T., Meyer, A., Abetz, C. & Abetz, V. Planet-Like Nanostructures Formed by an ABC Triblock Terpolymer. *Macromol. Chem. Phys.* **220**, (2019).

16. Wang, Y. C., Inoue, A., Hasegawa, H. & Takenaka, M. The Formation of OTDD Network Structure in PS-b-PI-b-PDMS Triblock Terpolymer. *Macromol. Chem. Phys.* **218**, 1–7 (2017).

17. Kong, W., Jiang, W., Zhu, Y. & Li, B. Highly Symmetric Patchy Multicompartment Nanoparticles from the Self-Assembly of ABC Linear Terpolymers in C-Selective Solvents. *Langmuir* **28**, 11714−11724 (2012) doi:10.1021/la3014943.

18. Hashimoto, T., Fujimura, M. & Kawai, H. Domain-Boundary Structure of Styrene-Isoprene Block Copolymer Films Cast from Solutions. 5. Molecular-Weight Dependence of Spherical Microdomains. *Macromolecules* **13**, 1660–1669 (1980).

19. Breiner, U., Krappe, U., Jakob, T., Abetz, V. & Stadler, R. Spheres on spheres – a novel spherical multiphase morphology in polystyrene-block-polybutadiene-block- poly(methyl methacrylate) triblock copolymers. *Polym. Bull.* **40**, 219–226 (1998).

20. Fleischer, G., Kärger, J. & Stühn, B. Chain diffusion in the melt of an asymmetric diblock copolymer in the disordered and ordered state. *Colloid Polym. Sci.* **275**, 807–813 (1997).

21. Yokoyama, H. & Kramer, E. J. Diffusion of triblock copolymers in a spherical domain structure. *Macromolecules* **33**, 954–959 (2000).

22. Flory, P. J. & Rehner, J. Statistical Mechanics of Cross-Linked Polymer Networks II. Swelling. *J. Chem. Phys. J. Chem. Phys. J. Chem. Phys. J. Chem. Phys. Solut. Long Chain Compd. J. Chem. Phys. J. Chem. Phys.* **11**, 1214–1365 (1943).

23. Scalfani, V. F. & Bailey, T. S. Access to nanostructured hydrogel networks through photocured body-centered cubic block copolymer melts. *Macromolecules* **44**, 6557–6567 (2011).

24. Mai, S. M. *et al.* Microphase-separation behavior of triblock copolymer melts. Comparison with diblock copolymer melts. *Macromolecules* **33**, 5124–5130 (2000).

25. Matsen, M. W. & Thompson, R. B. Equilibrium behavior of symmetric ABA triblock copolymer melts. *J. Chem. Phys.* **111**, 7139–7146 (1999).

26. Zhou, Y., Long, X., Xue, X., Qian, W. & Zhang, C. Morphologies and dynamics of linear ABC triblock copolymers with different block sequences. *RSC Adv.* **5**, 7661–7664 (2015).

27. Dormidontova, E. E. Micellization kinetics in block copolymer solutions: scaling model. *Macromolecules* **32**, 7630–7644 (1999).

28. Jiang, T., Wang, L., Lin, S., Lin, J. & Li, Y. Structural evolution of multicompartment micelles selfássembled from linear ABC triblock copolymer in selective solvents. *Langmuir* **27**, 6440–6448 (2011).

29. Schacher, F., Walther, A., Ruppel, M., Drechsler, M. & Müller, A. H. E. Multicompartment core micelles of triblock terpolymers in organic media. *Macromolecules* **42**, 3540–3548 (2009).

CHAPTER 5: SUMMARY OF RESULTS AND FUTURE DIRECTIONS

5.1 Summary of Major Results

The purpose of this dissertation was to design and synthesize a fatigue-resistant and energy-dissipative hydrogel from ABC and ABCBA block polymers. The design of the hydrogel required multiple steps and iterations to create and study the molecular structure which would result in the desired fatigue-resistant and energy-dissipative mechanical properties. The first step was to synthesize ABC polymers in the correct volume fractions to form the necessary sphere morphology, then use those polymers to create hydrogels that dissipated more energy than the SOS hydrogel without losing the fatigue-resistant properties. The following paragraphs detail the results of each step within the process of designing the SIOIS hydrogel.

Chapter 2 details the synthetic design and morphological characterization of SBO and SIO polymers with asymmetrical volume fractions to study the phase boundaries of the ABC sphere morphology. Using SAXS and rheology, we identified the experimental volume fractions for the sphere phase region which is one of the first published experimental attempts to define this region. Additionally, we discussed the challenges associated with synthesizing and characterizing polymers with the large molecular weights necessary for hydrogel formation. We found that these large molecular weights resulted in polymers which formed a liquid-like packing of spheres or cylinders rather than more periodic formations of these shapes. To our knowledge this is the first time the sphere phase region has been defined experimentally in ABC polymers. The formation of the sphere morphology was crucial to using these SIO polymers in the next steps of forming a fatigue-resistant and energy-dissipative hydrogel.

Chapter 3 compared the physical and mechanical properties of the Bailey Group's previously designed fatigue-resistant SOS hydrogel to the novel SIOIS hydrogel which was synthetically designed to be both resist fatigue and dissipate energy. Cyclic compression testing showed that the SIOIS hydrogel

dissipated 1.45x more energy than the SOS hydrogel at 80% strain but maintained the recovery rates and elasticity that were advantageous in the SOS hydrogel. Both gels observed minimal loss of mechanical properties even up to 80% compressive strain. Tensile testing of the hydrogels showed that the SIOIS hydrogel also had a larger average bulk toughness compared to the SOS hydrogel. The inserted PI block in the SIOIS hydrogel did provide a mechanism for energy dissipation as well as provided flexibility to the sphere-PEO junction to allow a better extension of the hydrogel resulting in a tougher gel.

Chapter 4 was a study of the molecular structure of the SIOIS hydrogel comparing the mechanical properties achieved through different processing methods (melt pressing vs solvent casting) and through different PS block molecular weights (10kDa vs 17kDa). Solvent cast samples of both PS molecular weights dissipated more energy than their melt pressed counterparts and had larger strains at break and overall bulk toughness. Ultimately, solvent casting was necessary to promote phase separation between the PS and PI blocks and make the PI block accessible as the energy dissipation mechanism. In the PS block study, during both compression and tensile testing, the solvent cast 10kDa SIOIS hydrogel ($SIOIS_{10}$) had a larger modulus than the solvent cast 17kDa SIOIS hydrogel ($SIOIS_{17}$). This decrease in the modulus in the $SIOIS_{17}$ gel resulted in a lower amount of energy dissipated during each compression cycle and a lower average bulk toughness during tensile testing. The low modulus in $SIOIS_{17}$ was a result of a lower crosslink density in the gel due to a larger percentage of coupled SIOIS chains looping within their own sphere rather than bridging to act as physical crosslinks in the hydrogel. This looping formation is likely a metastable state which is captured while chain exchange as part of the microphase separation process. For both studies, the self-assmebly of the sphere morphology, either through lack of separation in the spheres or slow chain exchange, had a dramatic effect on the mechanical properties of the hydrogel.

5.2 Recommendations for Future Studies

The broader motivation behind the formation of a fatigue-resistant and energy-dissipative hydrogel was to eventually use this material in biomedical applications that require cyclical mechanical loading and can be subject to fracture especially during extension. Some applications could include soft

tissue replacements such as a knee meniscus where fast recovery is essential and catastrophic tearing is a common problem[1] or transcatheter heart valves where longevity of use could be benefited from a material that doesn't tear easily but is still flexible.[2] It's also possible that a material that can dissipate energy without breaking could be useful in protective equipment such as helmets or child car seats. The SIOIS hydrogel presented here shows the capability of this design strategy to place a mechanism that dissipates energy through hydrophobic contact with the water at every tethered micelle crosslink. The full potential for this hydrogel network design has not yet been met, but instead the door has been opened to many research possibilities for better understanding how this design works and how to improve it.

5.2.1 Increasing the energy dissipated within the hydrogel

While the energy dissipation exhibited by the SIOIS hydrogel is a success in proving the use of this design strategy, any increase in the amount of energy that can be dissipated by the network will result in a gel that is tougher and can be used in applications where larger amounts of energy need to be dissipated. The total amount of energy dissipated is directly related to the balance of the change in enthalpy and the change in entropy when the hydrophobic B block enters the water matrix. Therefore, changing the components that determine the free energy terms will change the amount of energy dissipated or whether energy is dissipated at all. As shown in Equation 5.1 where k is Boltzmann's constant, T is temperature, χ is the polymer-solvent interaction parameter, and n_p and θ_s are the volume fractions of polymer and water respectively.[3] Therefore, one of the ways to change the amount of energy dissipated by the hydrogel network is to change the value of χ.

$$\Delta H_m = \mathrm{kT}\chi n_p \theta_s \qquad \textbf{Equation 5.1}$$

In the hydrogel being studied here, χ is a measure of the contact energy of mixing the B block of the polymer and water; therefore, changing χ can be done by changing hydrophobicity. This modification will allow us to better understand how hydrophobicity plays a role in the energy dissipation and other

mechanical properties of the hydrogel. There is likely some limit to the hydrophobicity of the B block. If the B block were so hydrophobic that the enthalpic penalty to stretch the polymer molecules into the water was more than the force to break the PEO bonds, the hydrogel would fracture bonds rather than stretch the B block into the water. In between these extremes, we hypothesize there will be some variation of the energy dissipation by the network.

Polybutadiene provides an ideal chemical structure to change the hydrophobicity of the B block without having to study an entirely new AB'C and AB'CB'A polymer phase behavior system. Unlike polyisoprene, 1,2-polybutadiene has a reactive terminal diene that can be modified after PS-PB-OH synthesis to change the hydrophobicity of the B block. For example, polyethylethylene (PEE) can be formed using the thermal degradation of p-toluenesulfonylhydrazide(TSH) to form diimide. The diimide then hydrogenates the double bond in 1,2 polybutadiene forming the more hydrophobic PEE. This reaction is done in the presence of tripropyl amine (TPA) to prevent acid formation.[4,5] It is expected that PEE will be more hydrophobic than PB. Alternately, through thiolene click reactions, the B block can be modified with 2-mercaptoethanol[6] and sodium 3-mercapto-1-propanesulfonate to produce two unique B blocks of decreased hydrophobicity relative to PB, including one block with an ionic interaction. In both cases, the presence of light with DMPA is used to create radicals which act as the initiator for the hydrothiolation of the polyalkene.

These modifications would allow study of the how the hydrophobic interactions, considered through the value of χ, contribute to the amount of energy that is dissipated. Because χ also has an influence on the polymer morphology, if polybutadiene as a B block does not form the desired CSS morphology, these modifications will still provide alternate B blocks which can be used to further explore (define) the ABC phase diagram without repeating exhaustive new polymer syntheses.

5.2.2 Increasing the strain at break and bulk toughness of the SIOIS polymer

As shown in chapter 3, the SIOIS hydrogels had a much larger bulk toughness than the SOS hydrogels largely due to a larger strain at break. We hypothesized that the rubbery polyisoprene block

provided flexibility to the PS-PEO junction where chain breakage is likely occurring in the SOS hydrogel. The increase in flexibility ultimately resulted in a larger strain at break for the SIOIS hydrogel. However, it is unclear if that increased strain at break is caused by the PI block entering the water matrix and elongating the chain distance between crosslinks or if the increased flexibility allowed better movement and elongation of the PEO chains. Therefore, if the B block is engaging as part of the chain between junctions, it is possible that by increasing the length of B block, we could also increase the strain at break and therefore the bulk toughness of the hydrogel. Additionally, if the B block is pulled farther into the water matrix, more energy would be dissipated due to more interactions between the B block polymer molecules and water as shown in Equation 5.1. In the SIOIS hydrogel investigated here, the PS and PI blocks had a volume fraction ratio of 3:1. Increasing the volume fraction of the polyisoprene block to have a PS:PI volume fraction ratio of 2:1 or 1:1 PS:PI would allow us to test if increasing the size of the PI block actually increases the strain at break of the hydrogel. The PS block would be kept as small as possible at 10kDa.

Changing the volume fractions ratios of the PS and PI blocks will change the phase behavior of the SIO polymer. However, the increase in the XN value with the larger PI block molecular weight could have the added benefit of promoting phase separation between the PS and PI blocks. The volume fraction boundaries for the C block in the computational sphere phase region do decrease as the PI volume fraction increases.[7] Therefore, increasing the volume fraction of the B block that could result in slightly smaller volume fractions of PEO being necessary for sphere formation and therefore similar or smaller total polymer molecular weights being required for sphere formation. This change of the B block size would have the added benefit of providing data for regions of the ABC phase diagram that have not been explored experimentally.

The microphase separation between the PS and PI blocks was a non-trivial roadblock to the energy dissipation of the SIOIS hydrogel that was ultimately solved by promoting phase separation through solvent casting. It is very possible that increasing the size of the B block would result in similar issues to the SIOIS17 hydrogel where even solvent casting was too fast of a process to allow equilibrium

phase separation. However, solvent casting is not a long-term solution to processing polymer on a large scale which could create similar issues to the SIOIS hydrogels presented here.

5.2.3 Mechanical and Molecular Characterization Techniques

While in this work we mainly discussed bulk toughness of a material, it would also be useful to measure the fracture resistance of the hydrogel. Fracture toughness is a measure of how the material resists crack growth within the network through energy dissipation. This is much more a measure of how the material responds directly at the crack tip compared to the bulk response measured by bulk toughness. A collaborator for the Bailey group, Rong Long, has extensive experience with fracture testing of soft materials and uses imaging to track particles during fracture.[8,9] Fracture testing would provide insight into how the energy dissipation mechanism is responding when faced with a defect by tracking how quickly the crack propagates and any directional change of the crack. Additionally, the SOS hydrogel appears to have a unique response to the fracture solely due to the tethered micelle network that is currently being investigated.[10] Comparison of the SOS and SIOIS hydrogel could give important insight into how the tethered micelle network and the energy dissipation mechanism in the SIOIS hydrogel are contributing to the mechanical properties of the hydrogel.

Additionally, to study how the B block hydrophobicity and size affect the hydrogel mechanical properties it would be useful to better understand the strain and stress conditions which result in the B block is entering the water matrix. We had hypothesized that the B block would only be engaged at large strains. However, in the cyclic tensile test, we never observed hysteresis between the loading and unloading curves that would suggest energy dissipation occurring and in compression tests we observed hysteresis throughout the entire strain. It would be useful to know how much of the B block is engaging with the water and how that changes as the strain changes in both compression testing and tensile testing. The fast recovery times and presence of water make many in-situ experiments, but some possible opportunities exist.[11] Rheo-optical FTIR would be a useful characterization because it can provide rapid study of molecular orientations.[12] Compression and tensile testing performed during Synchrotron SAXS

which would provide information about how the sphere sizes and sphere arrangements are changing.[13] Hydrogel network structure and swelling has been previously studied using ^{1}H Multiple Quantum NMR.[14,15] In-situ UV-VIS has been used to quantify hydrogel cross-linking density.[16] However, the sphere formation and the mechanism of B block entering the water are quite sensitive to hydrophobicity of the B block, so, any modification of the B block such as fluorotagging could affect the overall mechanical properties of the hydrogel.

5.2.4 Sphere formation mechanism in ABC and ABCBA block polymers in the melt

As expected, the formation of the sphere morphology proved to be crucial to the fatigue resistance and the energy dissipation of the SIOIS hydrogel. When the PS and PI block could not microphase separate in the melt, the PI was not accessible to be pulled into the water, and there was a severe decrease in the energy dissipated by the network. Additionally, when the rate of chain exchange within the spheres was too slow during formation of the $SIOIS_{17}$ hydrogel network, many SIOIS chains were looping within spheres instead of bridging across spheres which lowered the crosslink density of the network and decreased the modulus of the hydrogel. While solvent casting did help some of problems faced in the sphere microphase separation process, it is not a long-term solution for the polymer processing. Solvent casting is slow, not reliable for making large homogeneous samples, and has less than ideal sample to sample consistency. Further study of the formation of the ABC and ABCBA sphere morphology would be beneficial to understanding if these large molecular weight samples with 3 blocks can microphase separate in the melt and therefore be useful in larger scale mechanical applications.

The formation of spheres in AB and ABA polymer systems has been highly studied.[17–21] Some computational studies of chain exchange have been conducted but have mainly focused on polymers in solution. In the AB systems, researchers have an understanding of how chain exchange and chain diffusion[17,18] occurs between spheres to create a homogeneous sphere network and how morphologies diffuse through order-order transitions[19,20] and order-disorder transitions.[21] Similar studies have not been performed on ABC and ABCBA polymers in the melt to our knowledge. Even in AB block polymer

spheres, the diffusion of one chain from one sphere to another is limited due to the interaction barrier between the sphere forming block and the matrix block. This would likely be even more exasperated in the ABC and ABCBA block polymers which have additional interaction parameters to account for. Additionally, a kinetic study of the chain exchange of spheres would be useful for confirming our hypothesis that large molecular weights were the main cause of the polymer processing challenges we faced or if the presence of a third block is also slowing the chain exchange process and resulting in liquid-like morphologies with network defects such as looping chains.

5.3 Final Remarks

In conclusion, the insertion of a rubbery, hydrophobic B block directly into a known fatigue-resistant hydrogel network was a proficient strategy for designing a hydrogel that is both fatigue-resistant and energy-dissipative. As hypothesized, the forced mixing of a hydrophobic block with water is a promising and innovative energy dissipation mechanism. Finally, the unique self-assembly process of ABC and ABCBA polymers into a sphere morphology, especially at large, mechanically-relevant molecular weights provides many opportunities for further study.

5.4 References

1. Lewis, J. T., Fischenich, K. M., Haut Donahue, T. L. & Bailey, T. S. Nanostructure-Driven Replication of Soft Tissue Biomechanics in a Thermoplastic Elastomer Hydrogel. *ACS Biomater. Sci. Eng.* **4**, 3854–3863 (2018).

2. Bui, H. T. *et al.* Transcatheter Heart Valves: A Biomaterials Perspective. *Adv. Healthc. Mater.* **10**, (2021).

3. Hiemenz, P. C. & Lodge, T. P. *Polymer Chemistry*. (2007).

4. Santin, C. K., Jacobi, M. M. & Schuster, R. H. Influence of 1,2 units content on the hydrogenation of polydienes by TSH. *J. Appl. Polym. Sci. **119**,* 1195–1203 (2011) doi:10.1002/app.32775.

5. Hahn, S. F. An improved method for the diimide hydrogenation of butadiene and isoprene containing polymers. *J. Polym. Sci. Part A Polym. Chem.* **30**, 397–408 (1992).

6. Wu, W., Zeng, X., Li, H., Lai, X. & Yan, Z. Facile Synthesis of Polyhydroxylated Polybutadiene Derived from Hydroxyl-Terminated Polybutadiene via Thiol-Ene Click Reaction. *J. Macromol. Sci. Part A* **51**, 229–239 (2014).

7. Tyler, C. A., Qin, J., Bates, F. S. & Morse, D. C. SCFT study of nonfrustrated ABC triblock copolymer melts. *Macromolecules* **40**, 4654–4668 (2007).

8. Lu, Y., Qi, Y., Tenardi, M. & Long, R. Mixed-mode fracture in a soft elastomer. *Extrem. Mech. Lett.* **48**, 101380 (2021).

9. Li, C. *et al.* Effects of network structures on the fracture of hydrogel. *Extrem. Mech. Lett.* **49**, 101495 (2021).

10. May, A. W. Functional Nanostructured Ionic Liquid-based Block Copolymer Systems For Energy Applications. (2021).

11. Michler, G. H. In situ characterization of deformation processes in polymers. *J. Macromol. Sci. - Phys.* **40 B**, 277–296 (2001).

12. Radebe, N. W., Fengler, C., Klein, C. O., Figuli, R. & Wilhelm, M. Rheo-IR: A combined setup for correlating chemical changes via FTIR spectroscopy and rheological properties in a strain-controlled rheometer. *Cit. J. Rheol.* **65**, 681 (2021).

13. Habumugisha, J. C. *et al.* Stretch-induced structural evolution of pre-oriented isotactic polypropylene films: An in-situ synchrotron radiation SAXS/WAXS study. *Polymer.* **214**, (2021).

14. Saalwächter, K., Chassé, W. & Sommer, J. U. Structure and swelling of polymer networks: Insights from NMR. *Soft Matter* **9**, 6587–6593 (2013).

15. Zou, X. *et al.* Viscoelasticity and Structures in Chemically and Physically Dual-Cross-Linked Hydrogels: Insights from Rheology and Proton Multiple-Quantum NMR Spectroscopy. *Macromolecules* **50**, 9340−9352 (2017) doi:10.1021/acs.macromol.7b01854.

16. Kang, X., Yu, Y., Bao, Y., Cai, W. & Cui, S. Real time quantification of the chemical cross-link density of a hydrogel by in situ UV-vis spectroscopy. *Polym. Chem.* **6**, 4252 (2015).

17. Fleischer, G., Kärger, J. & Stühn, B. Chain diffusion in the melt of an asymmetric diblock copolymer in the disordered and ordered state. *Colloid Polym. Sci.* **275**, 807–813 (1997).

18. Yokoyama, H. & Kramer, E. J. Diffusion of triblock copolymers in a spherical domain structure. *Macromolecules* **33**, 954–959 (2000).

19. Ryu, C. Y. & Lodge, T. P. Thermodynamic stability and anisotropie fluctuations in the cylinder-to-sphere transition of a block copolymer. *Macromolecules* **32**, 7190–7201 (1999).

20. Kim, J. K. & Han, C. D. Phase Behavior and Phase Transitions in AB- and ABA-type Microphase-Separated Block Copolymers. *Adv Polym Sci* **231**, 77–145 (2009).

21. Dormidontova, E. E. & Lodge, T. P. The order-disorder transition and the disordered micelle regime in sphere-forming block copolymer melts. *Macromolecules* **34**, 9143–9155 (2001).

APPENDIX A: SUPPLEMENTARY INFORMATION FOR CHAPTER 2

A.1 Representative ^{1}H-NMR of PS-PI-PEO (SIO-4a)

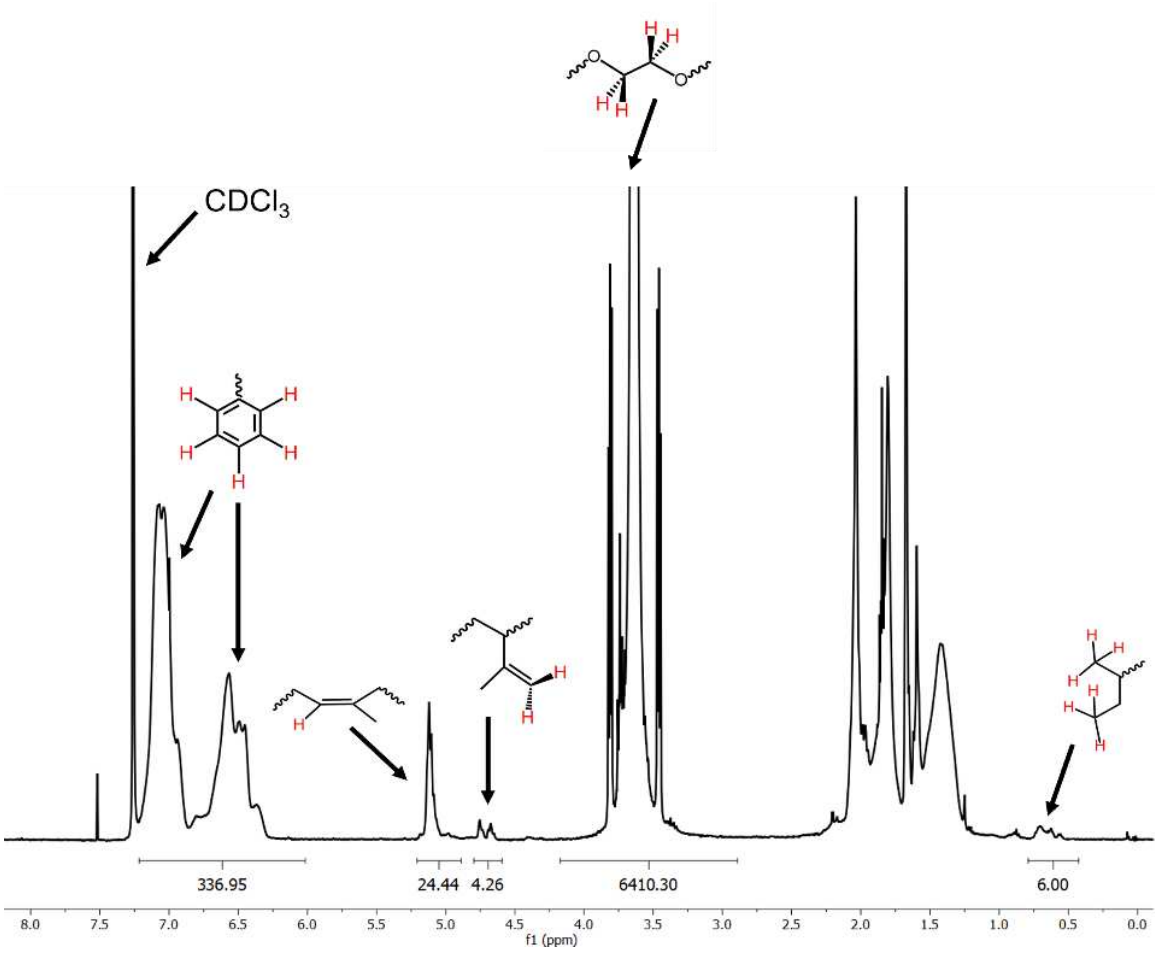

Figure A.8: Representative ^{1}H-NMR of SIO-4a using end group analysis normalized to the sec-butyl lithium initiator fragment to determine the molecular weight of each polymer block.

A.2 Representative GPC of PS-PI(SI-4) and PS-PI-PEO(SIO-4a)

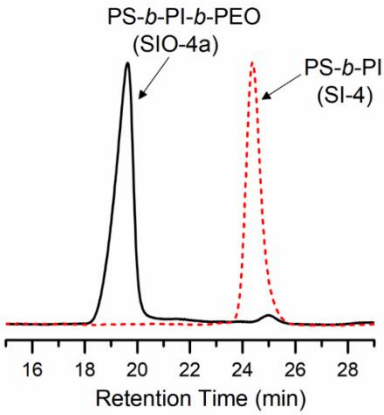

Figure A.2: Representative GPC of SIO-4a showing the PS-b-PI macroinitiator and the longer polymer chain PS-PI-PEO.

A.3-A.13 Molecular weights, SAXS Temperature Heating and Cooling Ramps, DMS Heating and Cooling, Frequency Sweeps for the SBO and SIO polymers synthesized

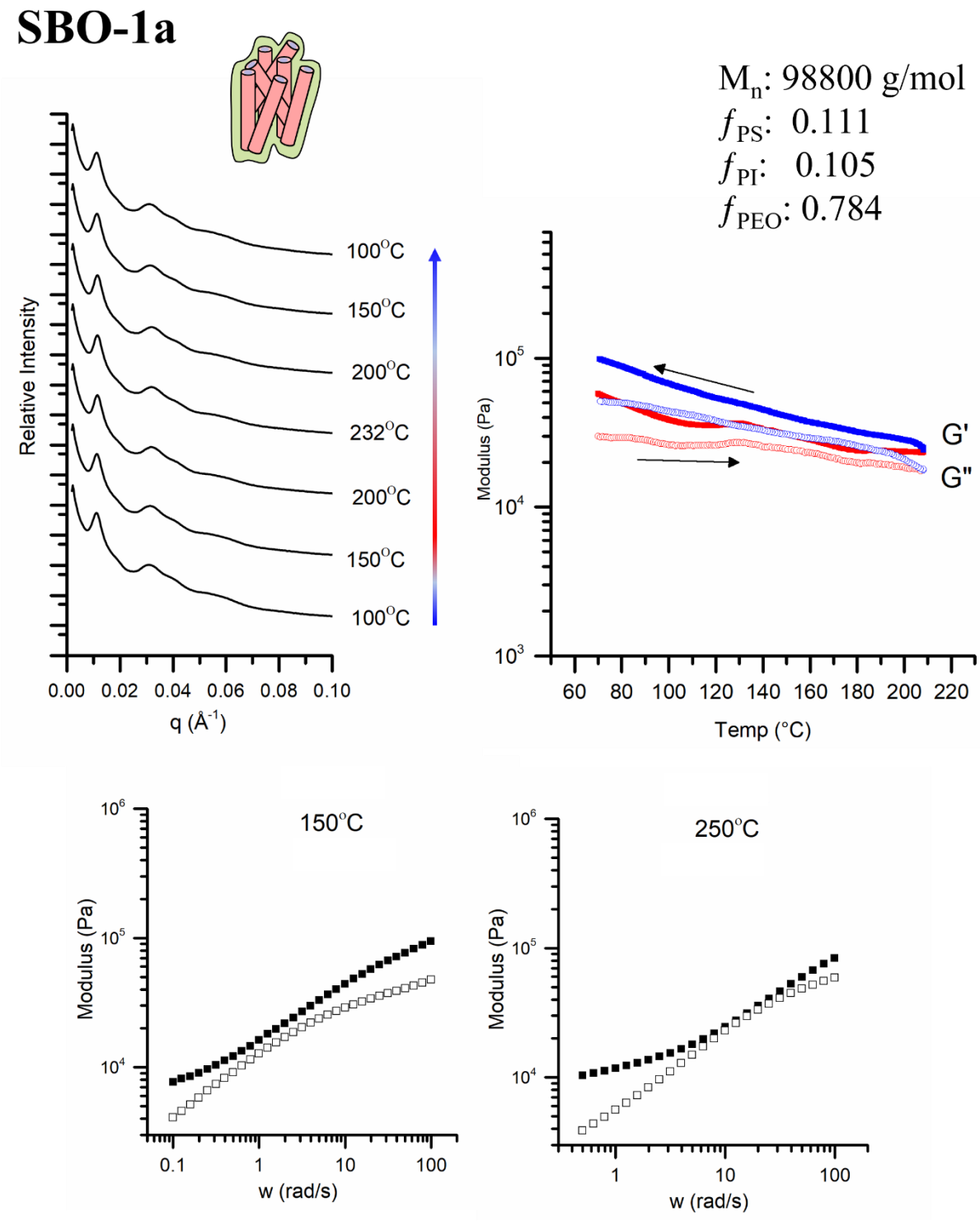

SBO-2a

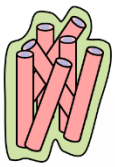

M_n: 119000 g/mol
f_{PS}: 0.110
f_{PI}: 0.051
f_{PEO}: 0.839

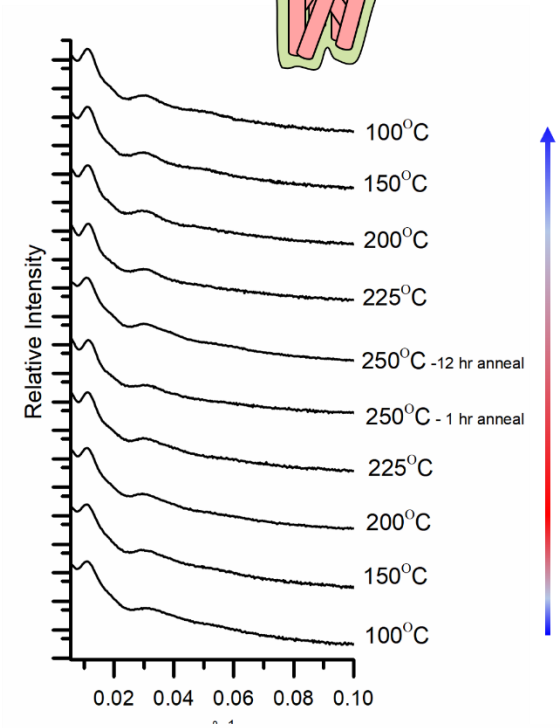

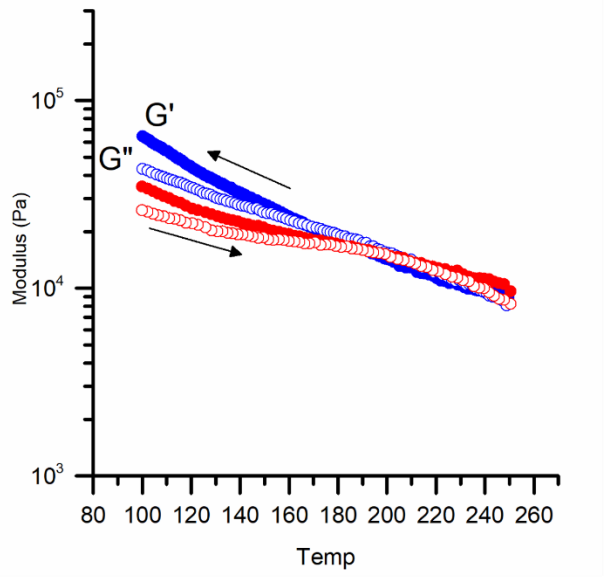

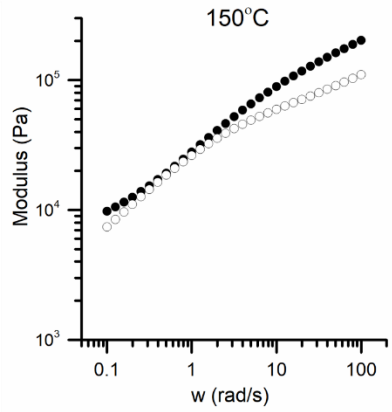

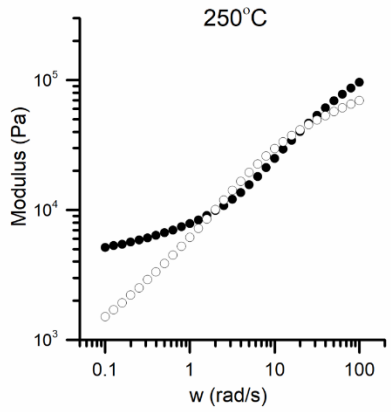

SBO-2b

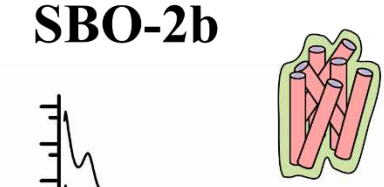

M_n: 150400 g/mol
f_{PS}: 0.87
f_{PI}: 0.047
f_{PEO}: 0.866

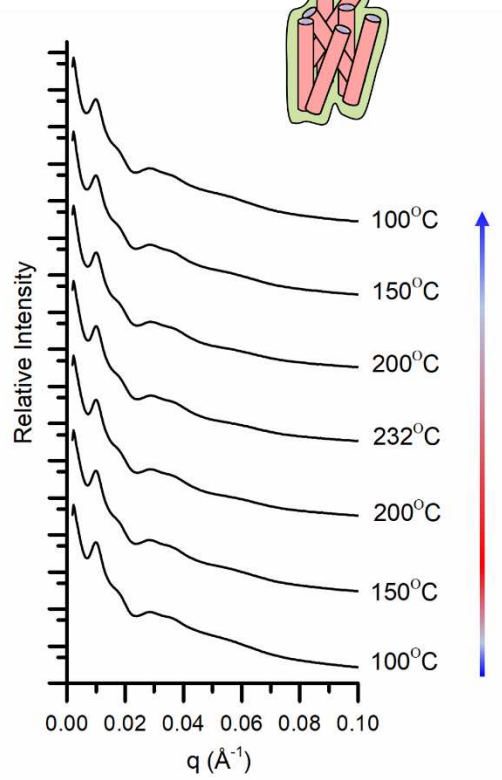

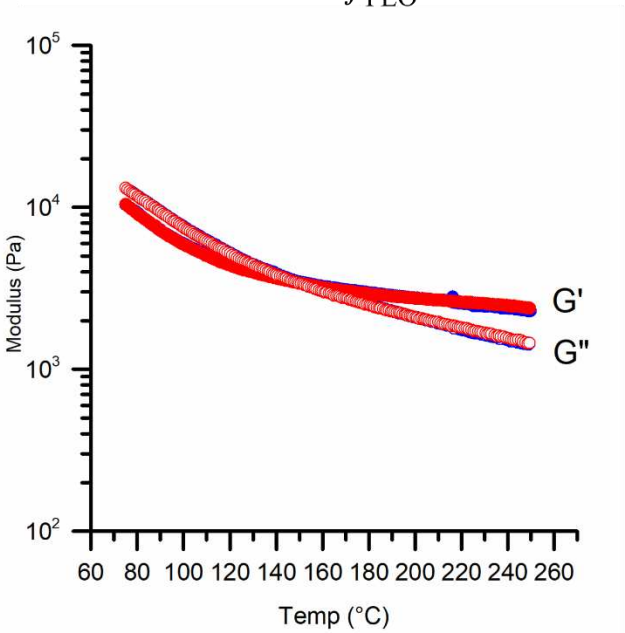

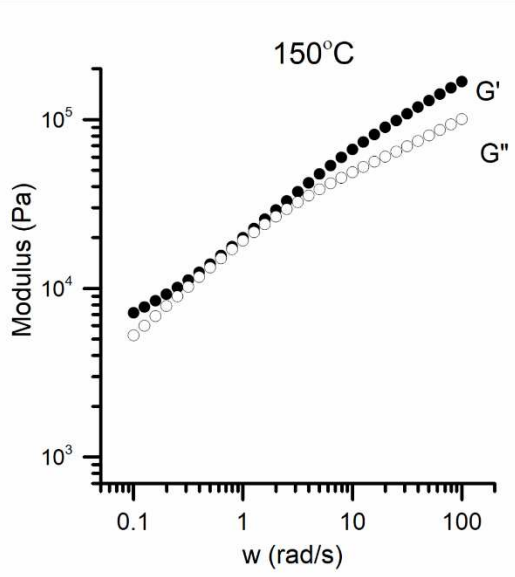

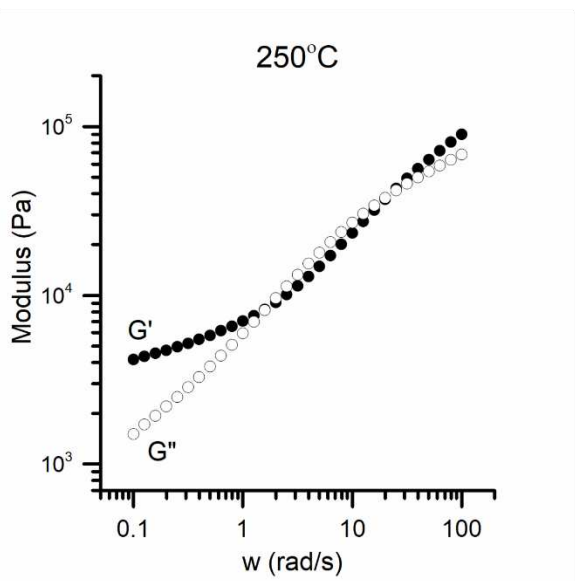

SIO-3a

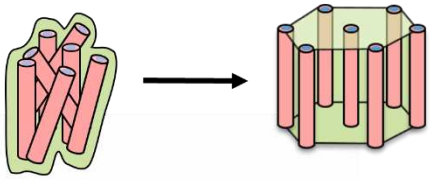

M_n: 53800 g/mol
f_{PS}: 0.166
f_{PI}: 0.139
f_{PEO}: 0.695

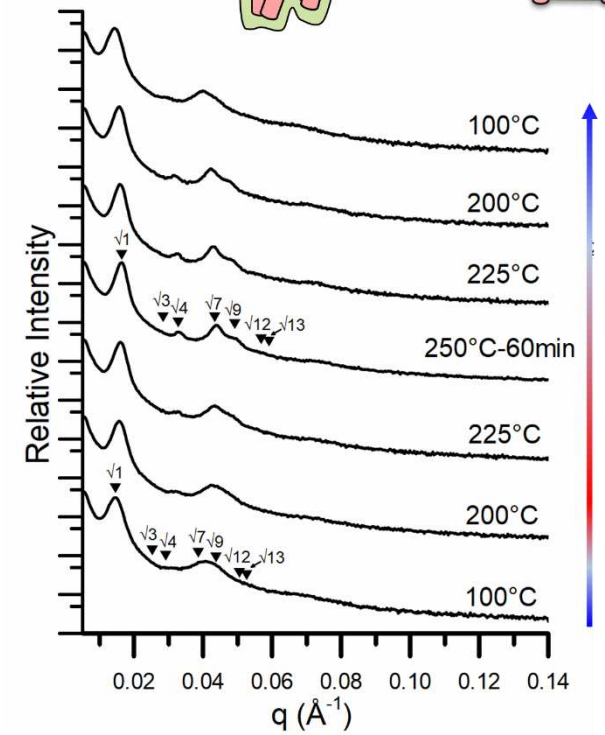

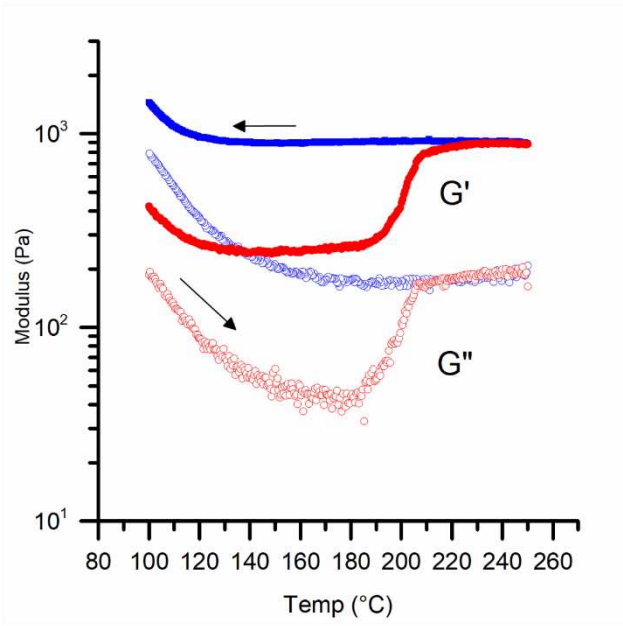

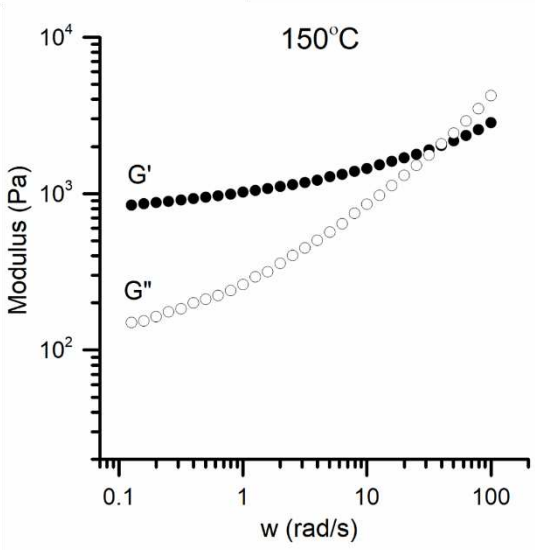

SIO-3b

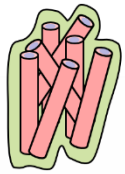

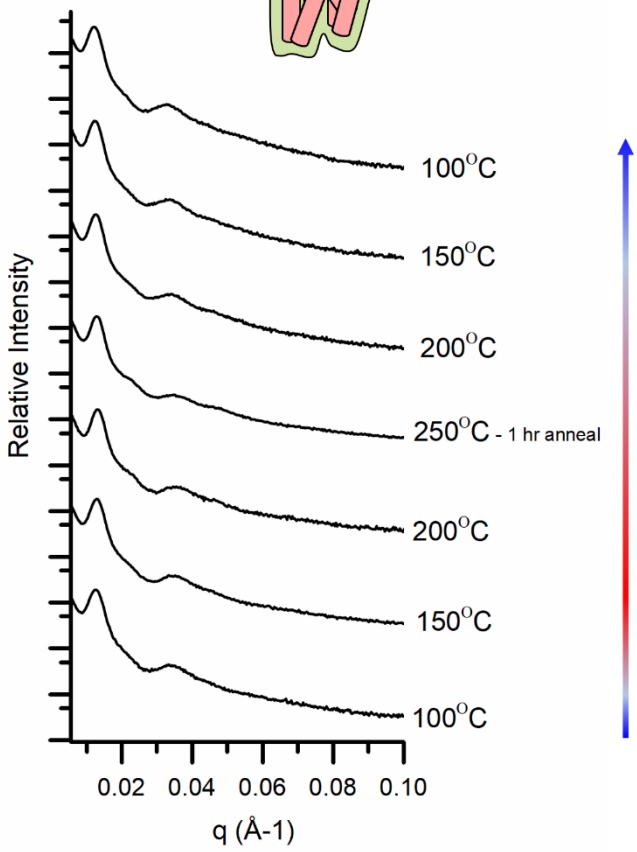

M_n: 99900 g/mol
f_{PS}: 0.091
f_{PI}: 0.029
f_{PEO}: 0.829

SIO-4a

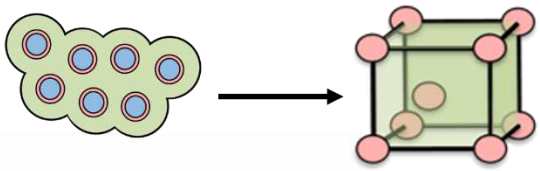

M_n: 86700 g/mol
f_{PS}: 0.096
f_{PI}: 0.030
f_{PEO}: 0.875

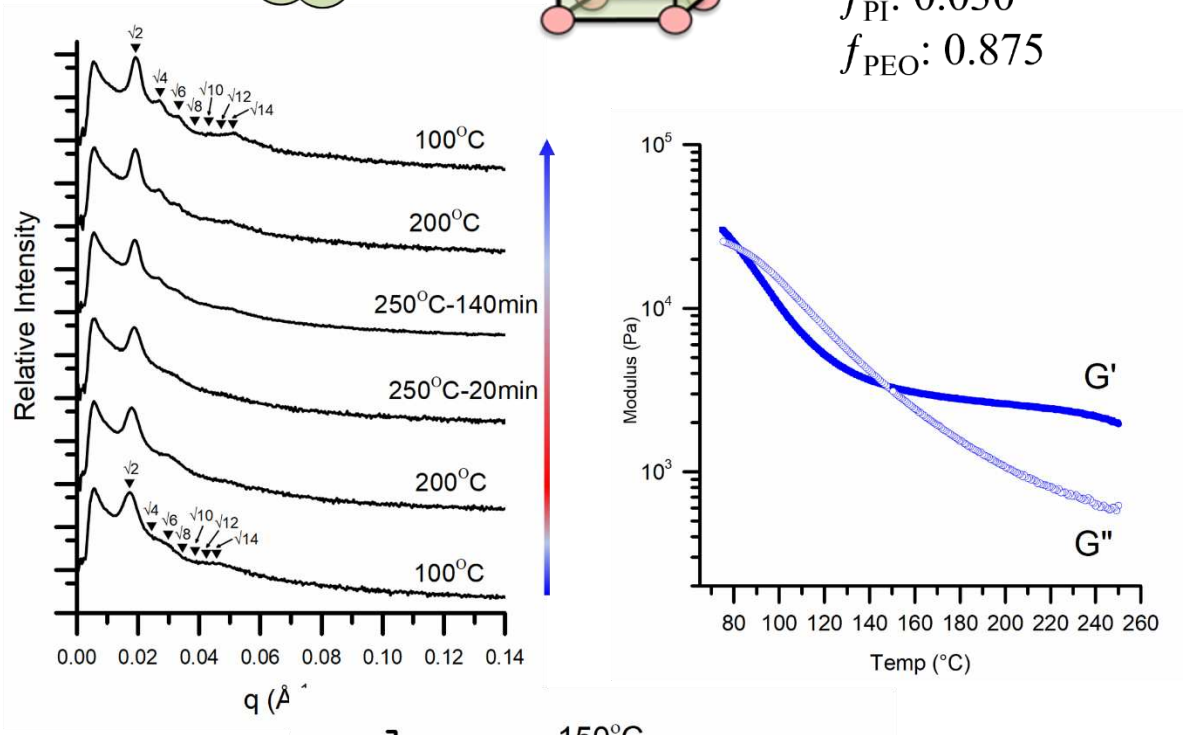

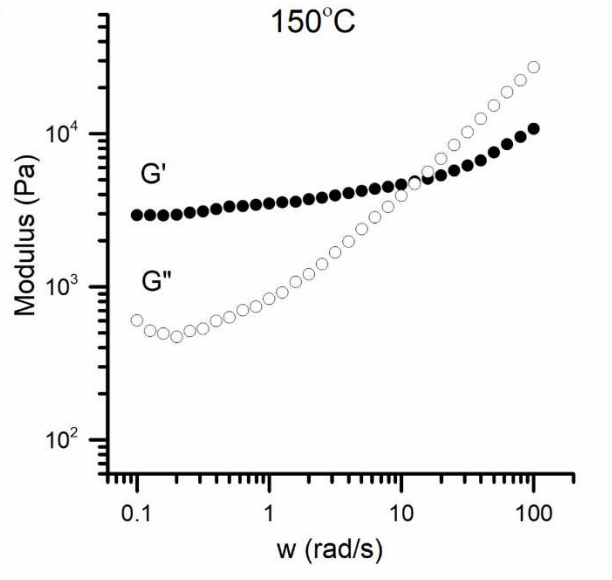

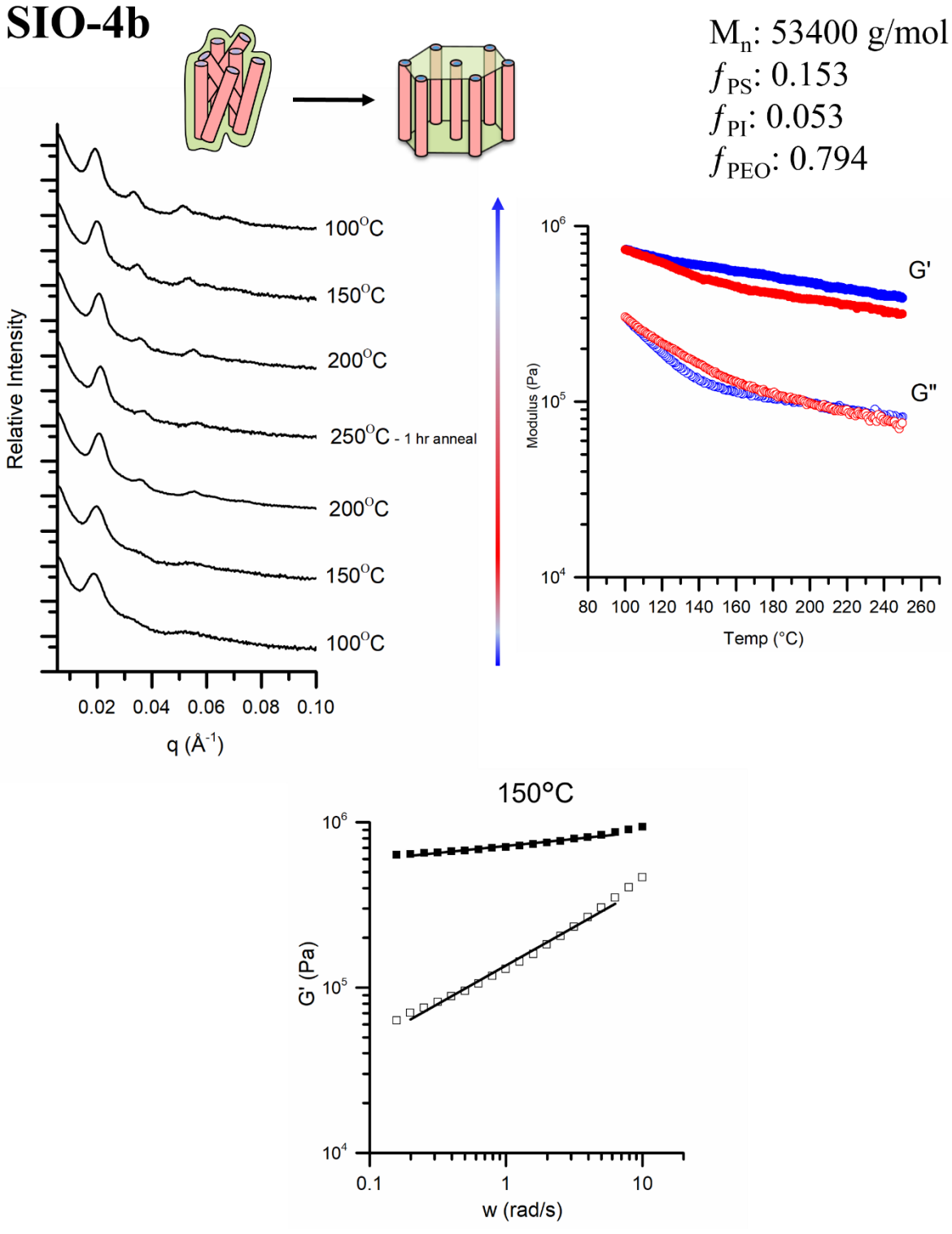
SIO-4b
M_n: 53400 g/mol
f_{PS}: 0.153
f_{PI}: 0.053
f_{PEO}: 0.794
100°C
150°C
200°C
250°C - 1 hr anneal
200°C
150°C
100°C
Relative Intensity
q (Å^{-1})
0.02 0.04 0.06 0.08 0.10
G'
G"
Modulus (Pa)
Temp (°C)
80 100 120 140 160 180 200 220 240 260
150°C
G' (Pa)
w (rad/s)
0.1 1 10

SIO-5a

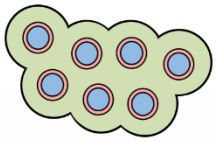

M_n: 115300 g/mol
f_{PS}: 0.096
f_{PI}: 0.031
f_{PEO}: 0.874

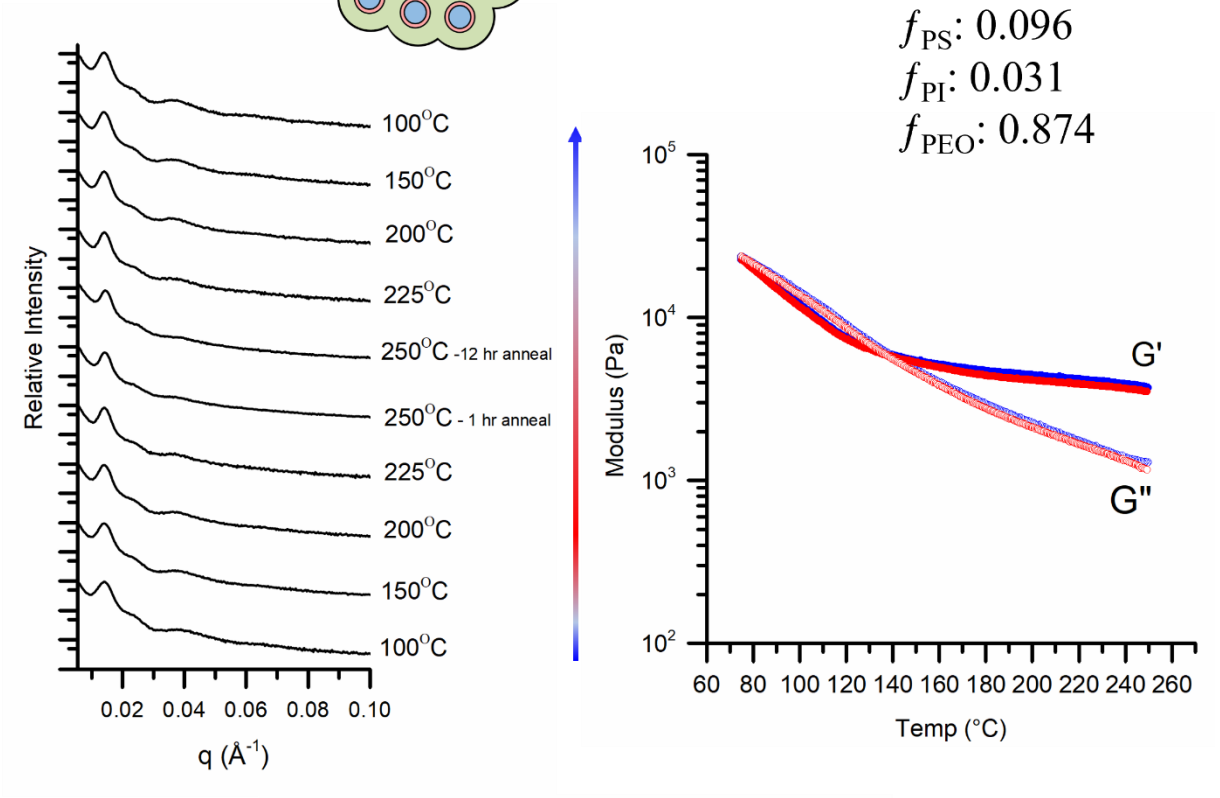

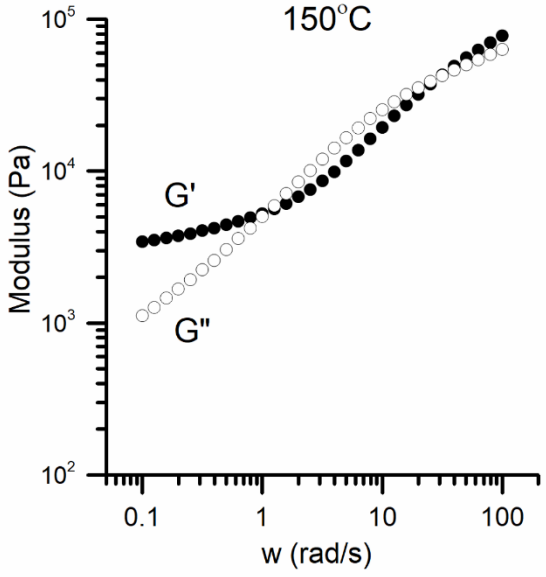

SIO-5b

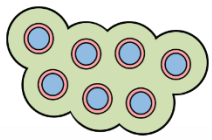

M_n: 128100 g/mol
f_{PS}: 0.086
f_{PI}: 0.029
f_{PEO}: 0.885

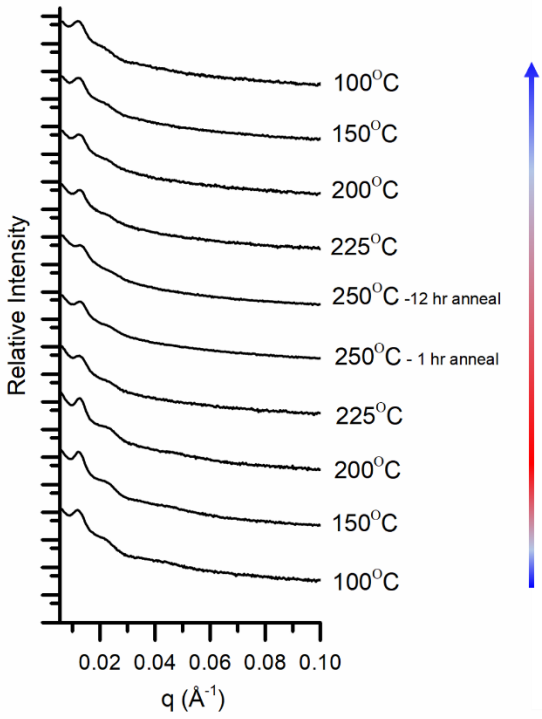

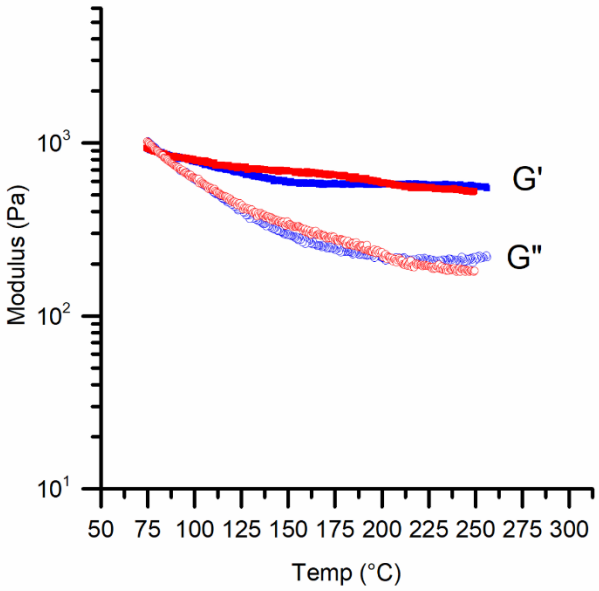

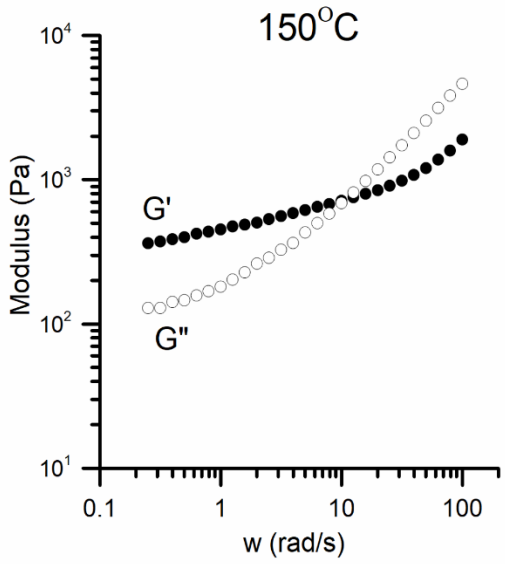

SIO-5c

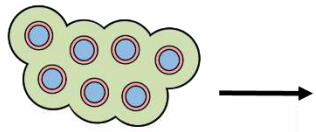

DISORDER

M_n: 196300 g/mol
f_{PS}: 0.057
f_{PI}: 0.019
f_{PEO}: 0.924

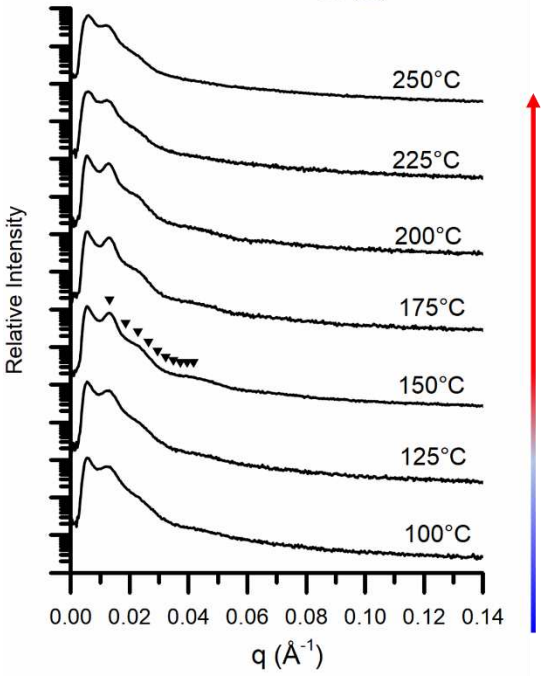

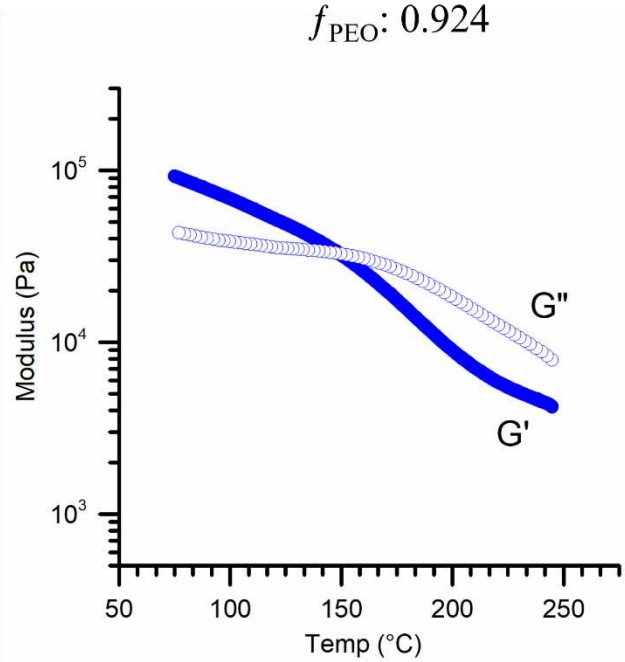

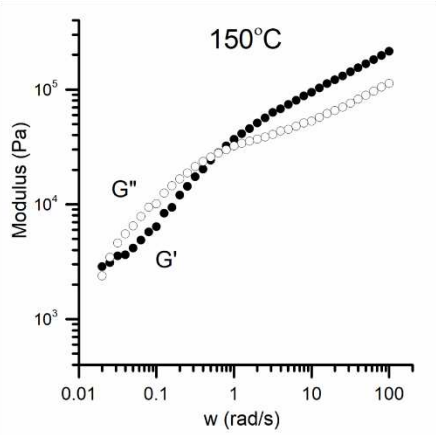

A.14 Change in SAXS principal scattering peak as temperature increases

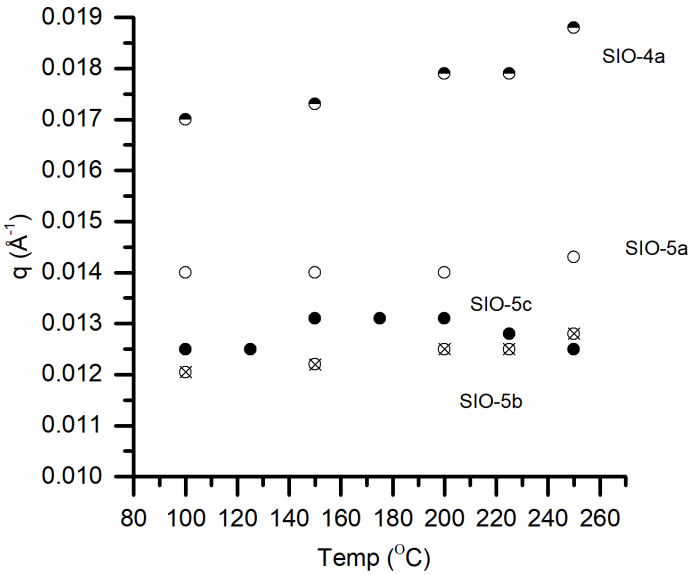

This graph shows the change in the SAXS principal scattering peak for the sphere-forming SIO polymer synthesized here: SIO-4a, SIO-5a, SIO-5b, and SIO-5c. The q* values for SIO-4a, SIO-5a, and SIO-5b increase as the temperature increases. Because q is inversely related to domain spacing in the morphology, an increase in q points to a decrease in domain spacing. This relationship between domain spacing and temperature is what is expected for the polymers as the chains have more energy to move through entanglements to limit interfacial contact between unlike blocks and minimize chain stretching. The decrease in q* value, and therefore increase in the lattice domain spacing, as the temperature increases for SIO-5c indicates the sample is moving toward disorder where the noticeable domains are moving apart and blocks are mixing with each other.

A.15 Domain spacing comparisons between Sphere samples and between Cylinder samples

The domain spacings in SIO-4a, SIO-5a, SIO-5b, and SIO-5c were calculated using the principal scattering peak of a SAXS scattering plot at 100°C after annealing above 250°C. As expected, the domain spacings for SIO-4a, SIO-5a, SIO-5b increase as the total molecular weight of the block polymer increases (A.10a). However, SIO-5c, the largest molecular weight polymer, has a smaller domain spacing than SIO-5b. This decreased distance between the spheres in SIO-5c further points to it being near the

order-disorder boundary.[1] The sphere size for SIO-4a is calculated at ~11.5nm using the domain spacing of a BCC lattice and the density and molecular weight of the SIO-4A polymer. The sphere sizes for SIO-5a, SIO-5b, and SIO-5c are not as accurately calculated because the spheres are not situated on a BCC lattice. The distance between cylinders for SIO-1a, SIO-2a, SIO-2b, SIO-3a, SIO-3b, and SIO-4b were calculated using the principal scattering peak of a given SAXS scattering plot at 100°C after annealing at 250°C (A.3-7,9). The domain spacings for these the cylinder samples increases with increasing molecular weight as expected.(A.14b) The size of the PS or PI block and the volume fraction ratio of PS:PI does not seem to influence this relationship.

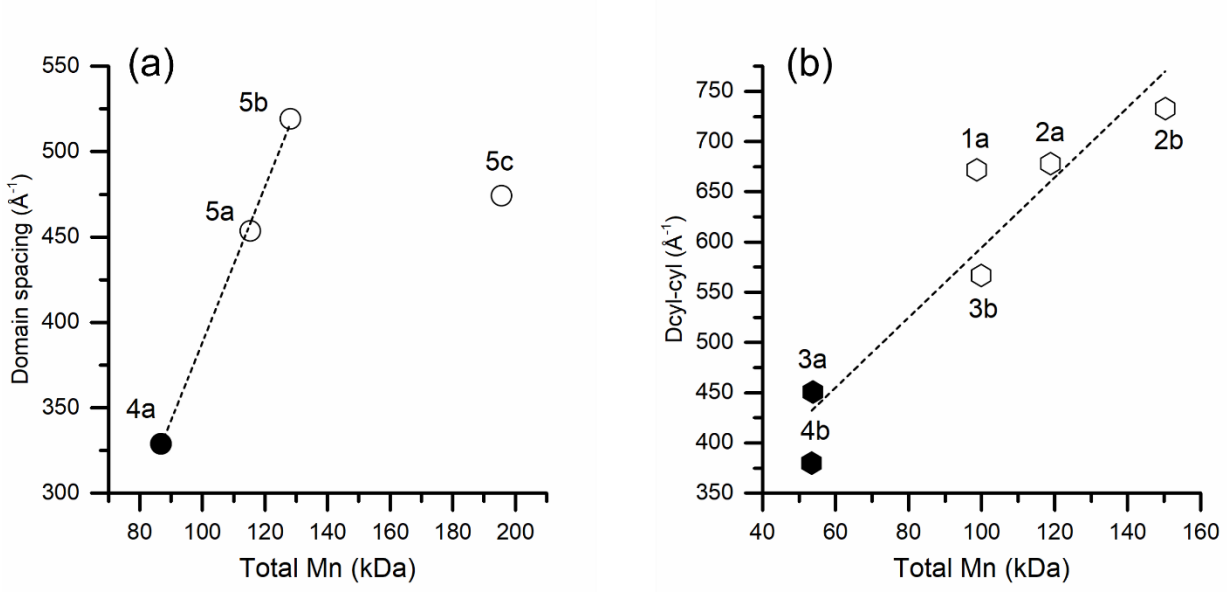

Figure A.14 (a) Plot of total Mn of the polymer vs the domain spacing as calculated from SAXS for all sphere-forming samples. Open circles denote an LLP morphology while the closed circle denotes a BCC morphology. (b) Plot of total Mn of the polymer vs the distance between cylinders for all cylinder forming samples. Closed hexagons denote an HPC morphology while open hexagons denote disordered cylinders.

A.16: Relationship between molecular weight and volume fraction

This graph is used to show the wide range of large molecular weights of the C block that are the result a small change in volume fraction which makes exploration of the sphere region of the ABC block polymer phase diagram difficult. The C block volume fractions for the sphere region are shown by the x. The potential molecular weights of the C block explored here, PEO, are shown on the y axis. The orange

curve shows the relationship between PEO volume fraction and PEO molecular weight for an SIO polymer that has a PS molecular weight of 10kDa and a PS to PI volume fraction ratio of 3:1.

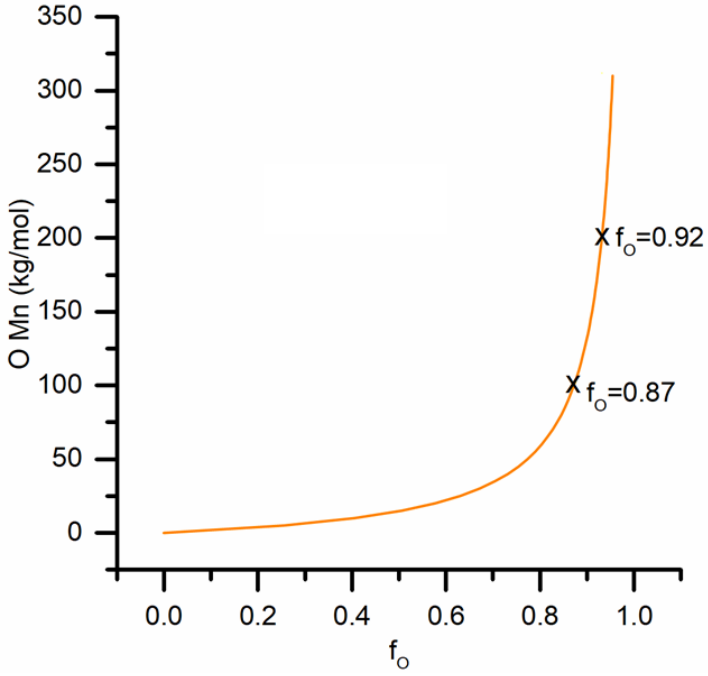

A.17: Table of Samples synthesized.

Manuscript ID	Lab Notebook ID
SB-1	ASK-1065
SBO-1a	ASK-1072
SB-2	ASK-1095
SBO-2a	ASK-1100
SBO-2b	ASK-1107
SI-3	ASK-1125
SIO-3a	ASK-1133
SIO-3b	ASK-1134
SI-4	ASK-1164
SIO-4a	ASK-1166
SIO-4b	ASK-2003
SI-5	ASK-1186
SIO-5a	ASK-1188
SIO-5b	ASK-1196
SIO-5c	ASK-1199

References

1. Hashimoto, T., Fujimura, M. & Kawai, H. Domain-Boundary Structure of Styrene-Isoprene Block Copolymer Films Cast from Solutions. 5. Molecular-Weight Dependence of Spherical Microdomains. *Macromolecules* **13**, 1660–1669 (1980).

APPENDIX B: SUPPLEMENTARY INFORMATION FOR CHAPTER 3

B.1 ^{1}H-NMR of PS-OH

All 1H-NMR was run and analyzed as described in Appendix D.

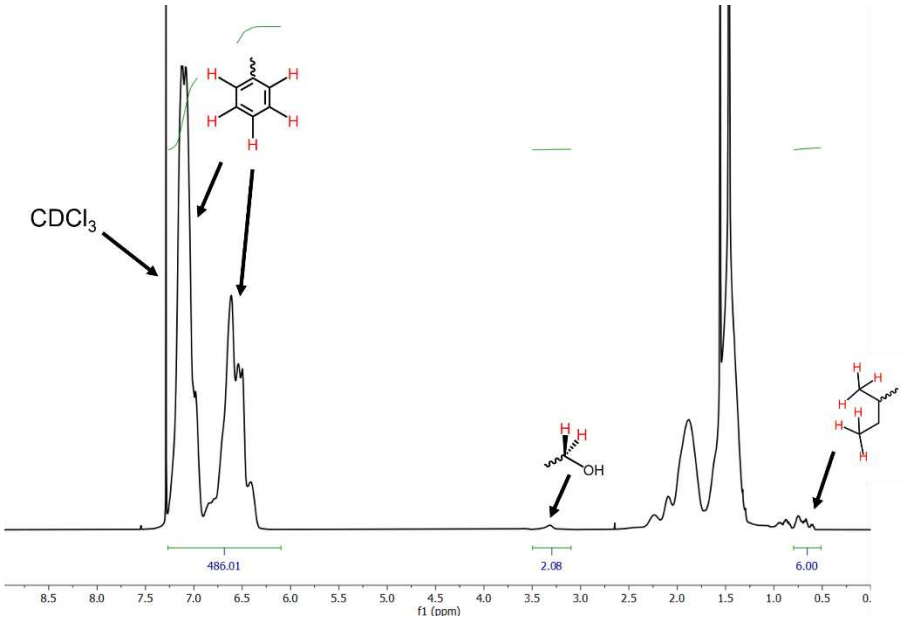

B.2 ^{1}H-NMR of PS-PEO-OH

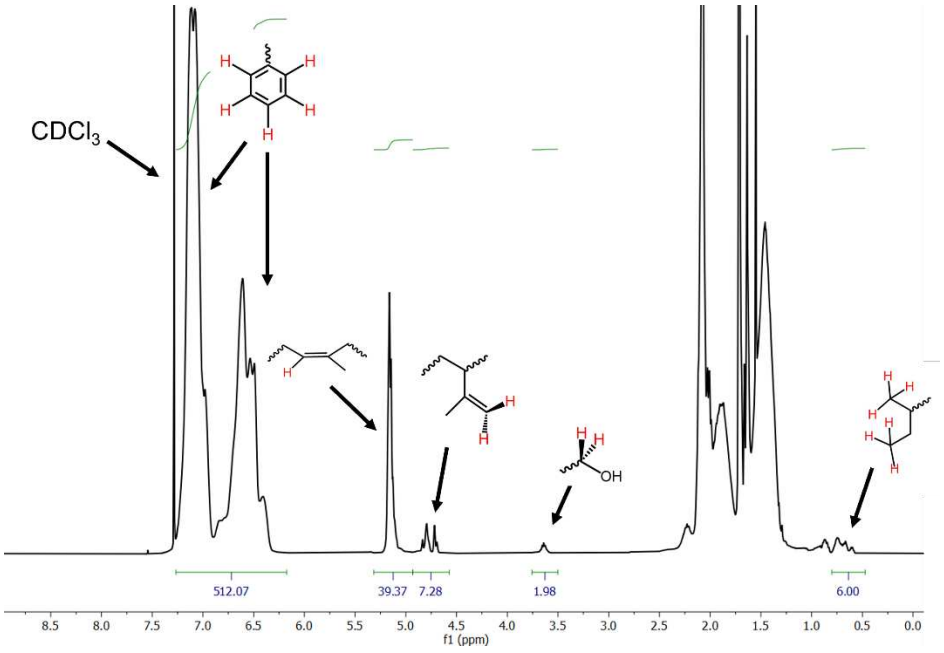

B.3 ^{1}H-NMR of PS-PI-OH

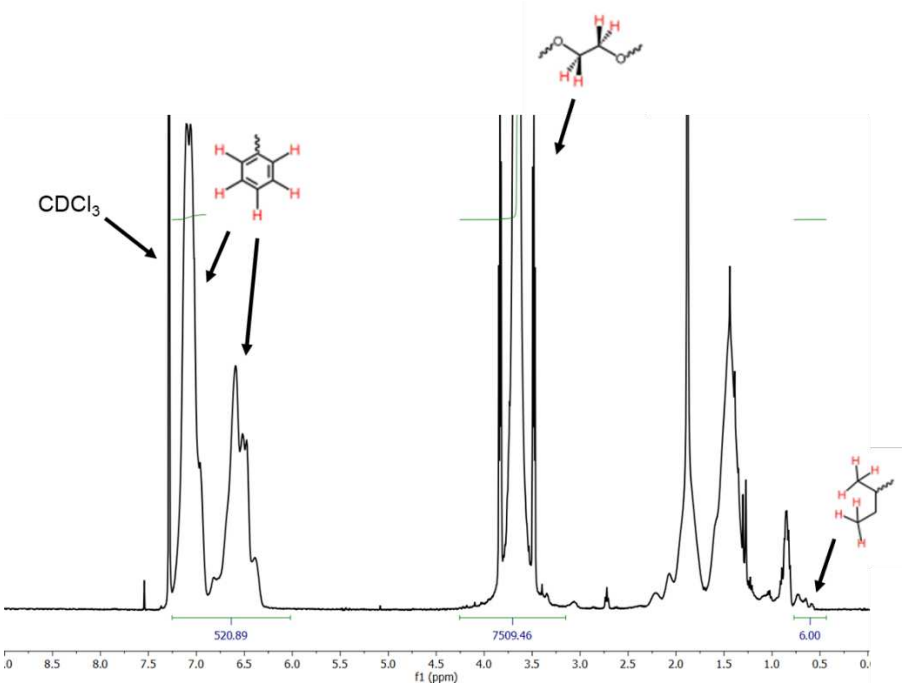

B.4 ^{1}H-NMR of PS-PI-PEO-OH

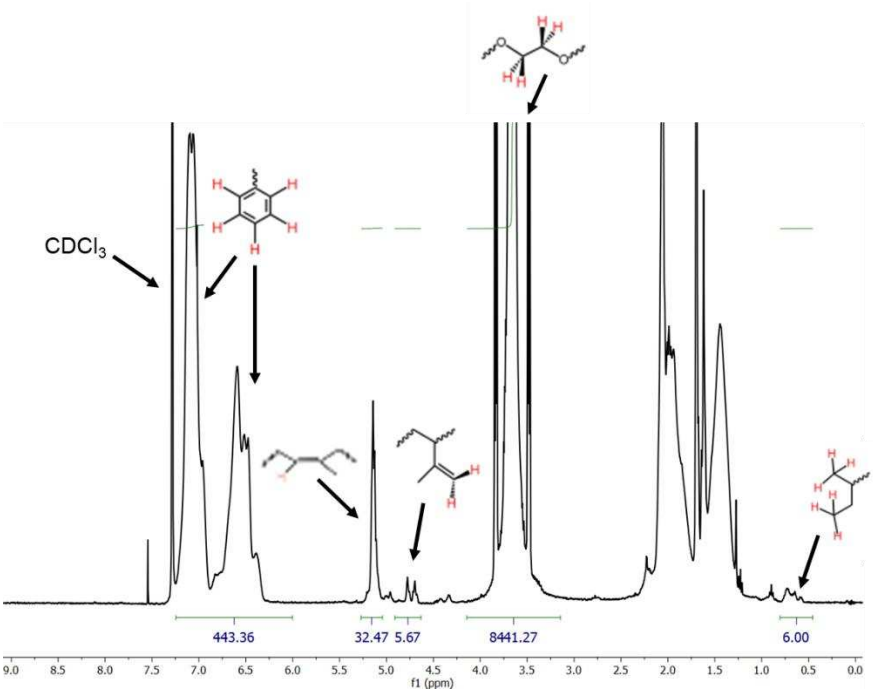

B.5 Preliminary Comparison of SIOIS and SOS samples to determine Swelling ratio and compressive modulus

Four blends of SO/SOS and four blends of SIO/SIOIS were freeze-dried from benzene with the correct weight fractions to form 0.25g polymer samples with four different mol fractions (10%, 30%, 37%, and 56%). The polymers were processed using the melt processing method. The swelling ratio (Q) was measured for each sample and plotted against the mol%. Exponential fits were calculated for the SOS blends and the SIOIS blends which are shown by the red lines. These equations were used to calculate the SOS mol% which would give similar swelling ratios for SOS and SIOIS. Once we moved to solvent-casting the polymers and found the swelling ratio of solvent-cast SIOIS to be slightly larger than SIOIS-melt, a slightly smaller SOS blend was ultimately used to ensure compressive modulus matching rather than exact swelling ratio matching.

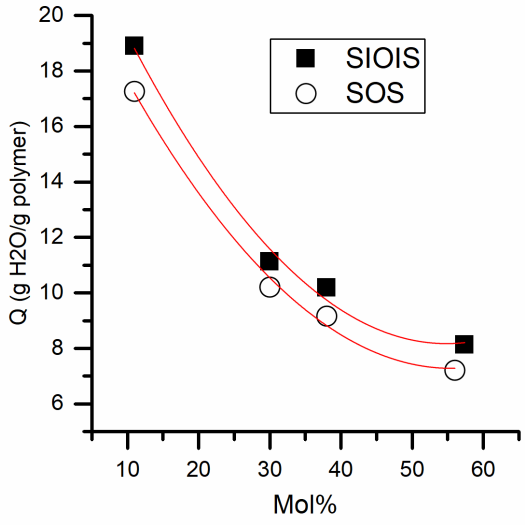

B.6 Melt Processing Method for SIOIS

Generalized depiction of the melt processing method used for the SIO/SIOIS and SO/SOS block

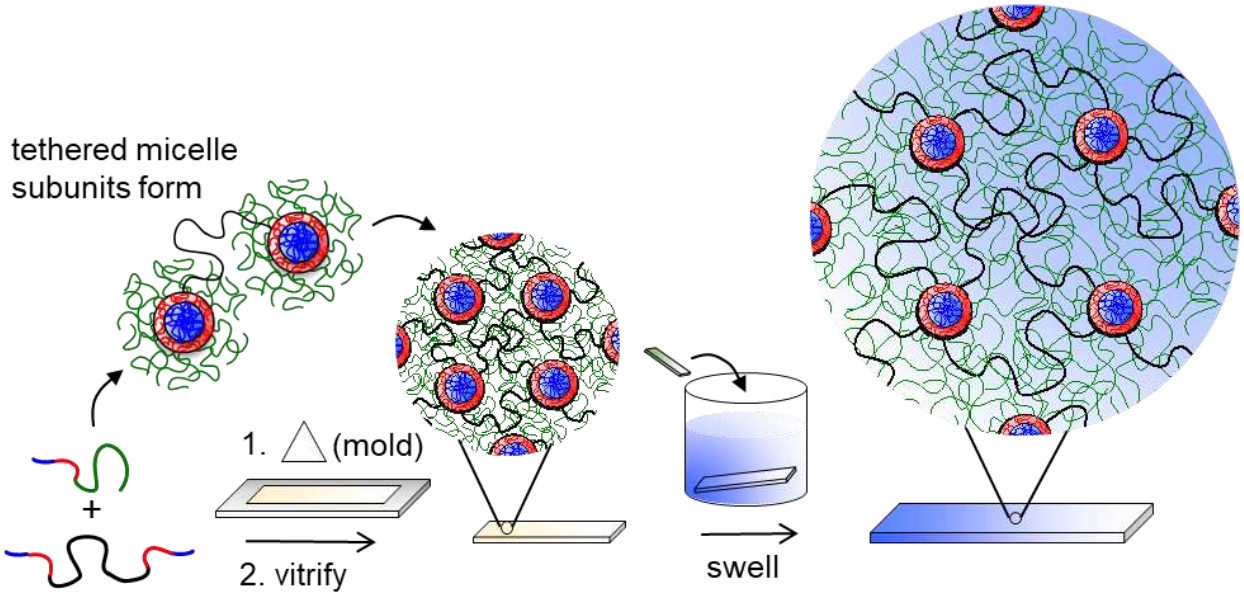

polymers. The process is the same for both, but the SIO/SIOIS polymer is shown here.

B.7 Compression cycles of samples used

A single compression cycle of each sample used in the average compression testing to 80% strain.

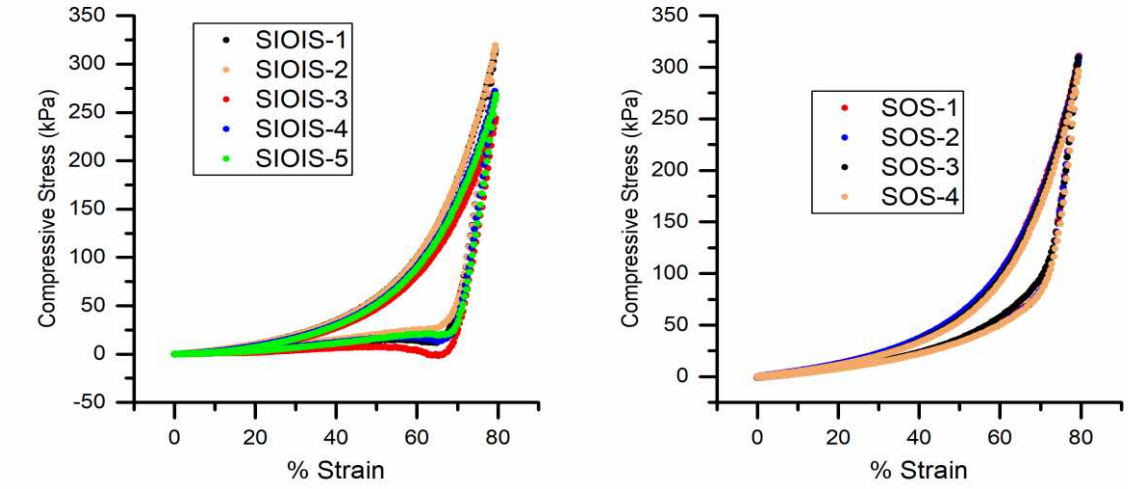

B.8 Frequency Sweep of SOS and SIOIS

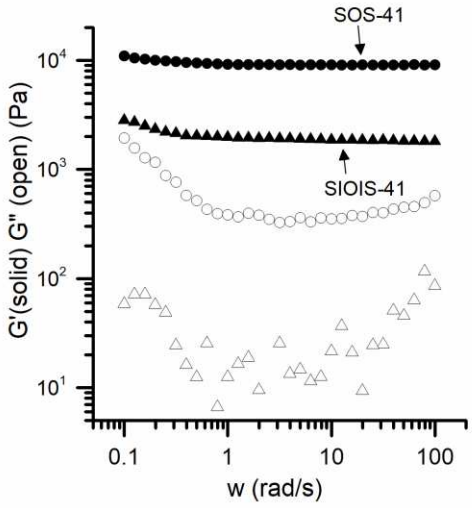

B.9 Table of Polymers used to make hydrogel

Manuscript ID	Lab Notebook ID
S-OH	ASK-2035
SO	ASK-2050
SOS	ASK-2160
SI-OH	ASK-1186
SIO	ASK-1188
SIOIS	ASK-2070

APPENDIX C: SUPPLEMENTARY INFORMATION FOR CHAPTER 4

C.1 Compression Stress-Strain Curves of Melt-Processed SIOIS$_{10}$, SIOIS$_{17}$ and SOS

Compression stress-strain curves for SOS(black), SIOIS10 (red), and SIOIS$_{17}$ (blue) hydrogels processed by melt-pressing.

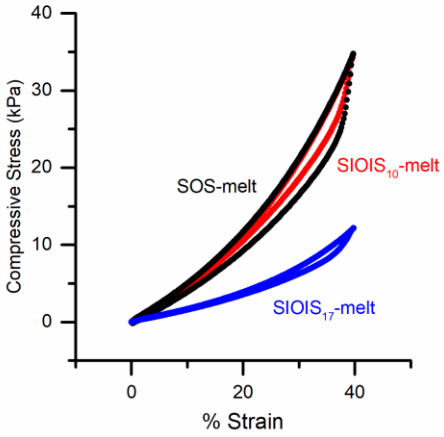

C.2 Qualitative comparison of SIOIS hydrogel made with 7700g/mol PS

We observed holes in the SIOIS hydrogel made with a small PS block. The polymer was very brittle and not able to be mechanically tested without falling apart.

C.3 ^{1}H-NMR of SI_{17}

All NMRs were run and analyzed as described in Appendix D. 1H-NMR for SI_{10} and SIO_{10} are shown in Appendix B.

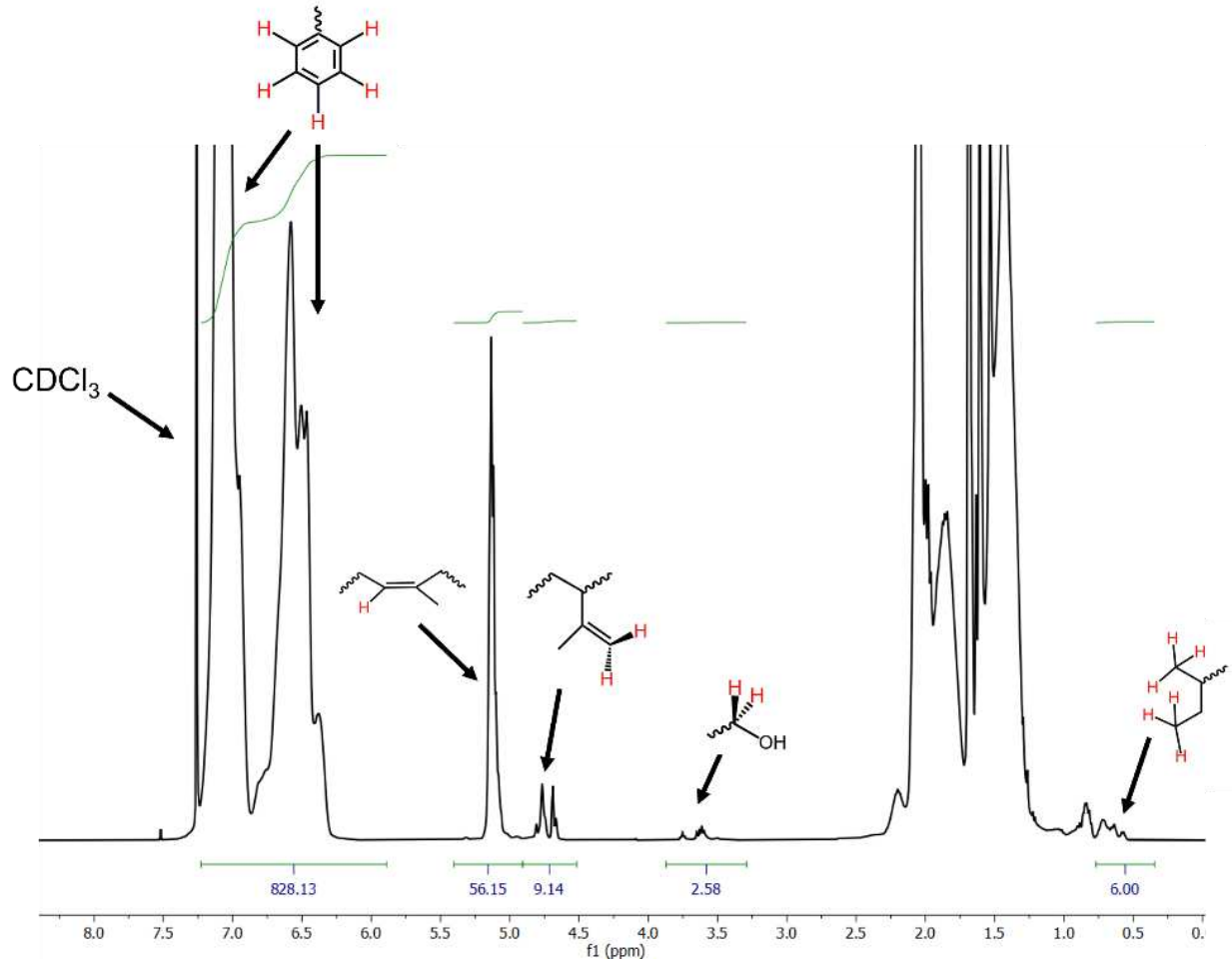

C.4 ^{1}H-NMR of SIO_{17}

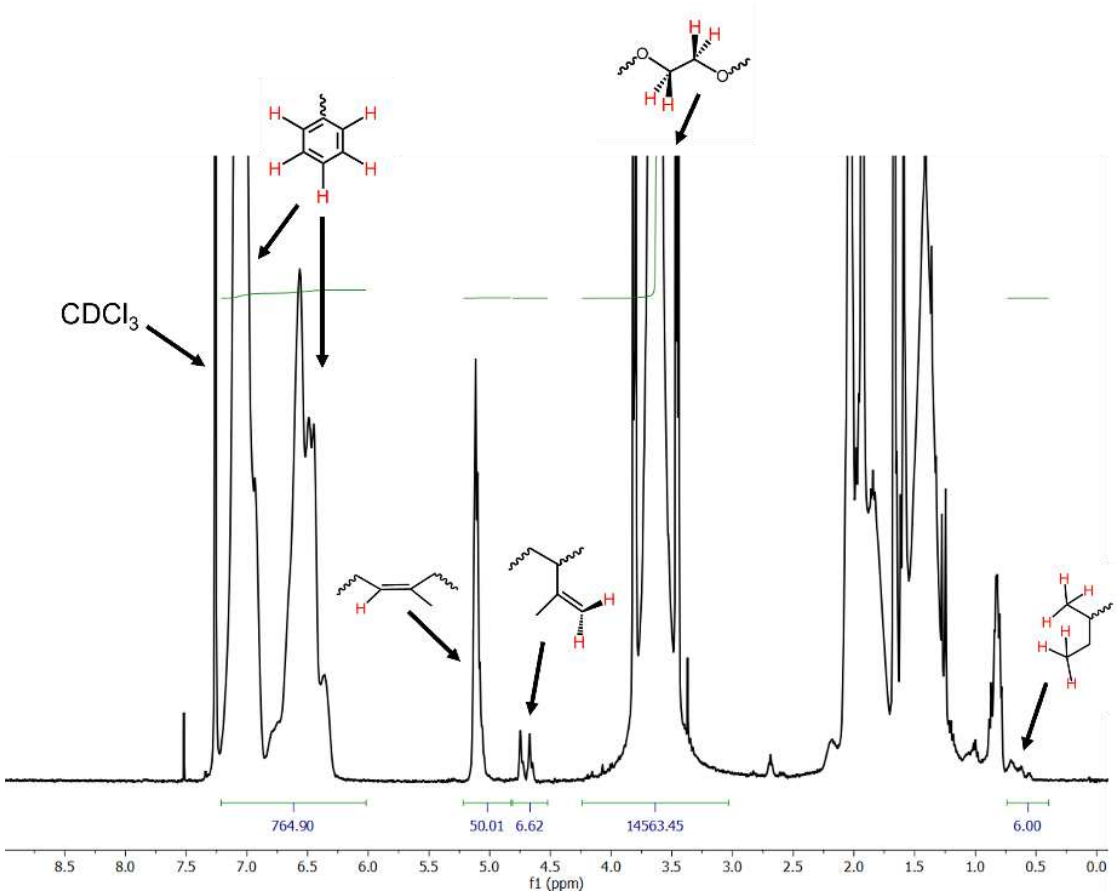

C.5 TGA of SI_{10} and SIO_{10}

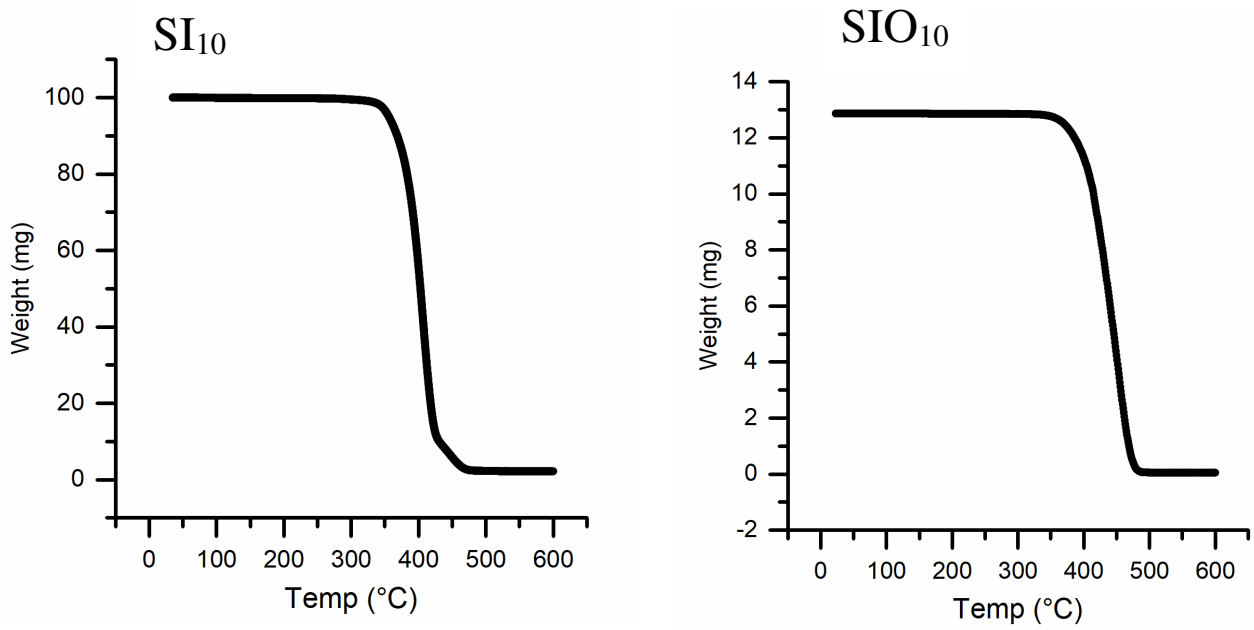

C.6 DSC of SIO_{10} and SIO_{17}

DSC data for SIO_{10} and SIO_{17}. The crystallization and glass transition of PEO is observed at ~70°C in both samples. The large presence of PEO covers what would be the glass transition of PS in that temperature region though it is possible that the drop observed from 70°C to 60°C during the cooling cycle in $SIOIS_{10}$ is the glass transition of PS. DSC of both SI samples had unusual changes in the baseline during the test that are likely the result of the polymer degrading before testing, therefore they are not included here.

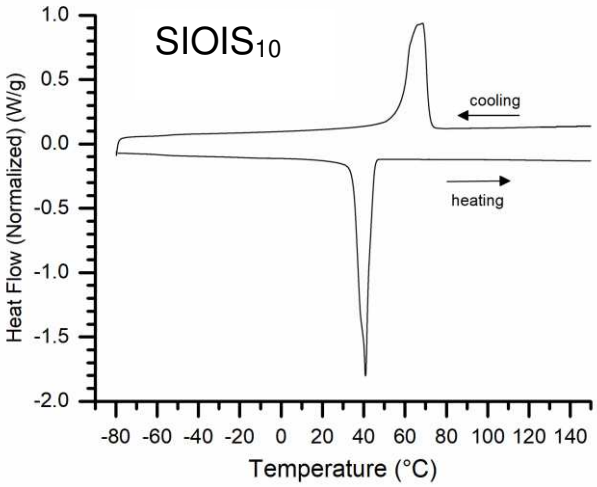

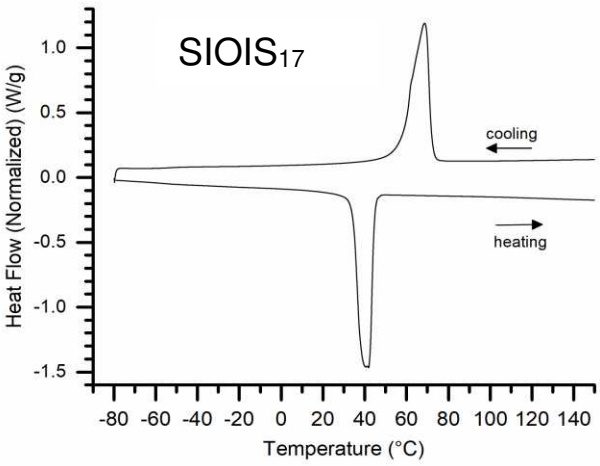

C.7 Compression Stress-Strain curves of Solvent-cast SOS Hydrogel

SOS was solvent cast from $CHCl_3$ in the same method as SIOIS, swollen in DI water, and subjected to compression testing. The solvent-cast SOS hydrogel performed significantly worse than the melt processed SOS hydrogel both in terms of overall compressive modulus of the hydrogel and the recovery of the sample between multiple cycles shown on the graph.

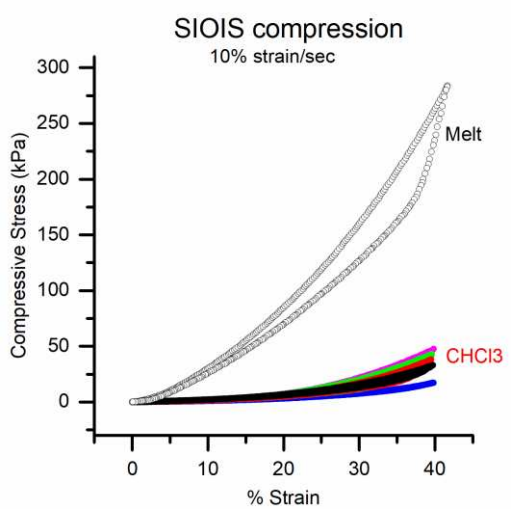

C.8 Description of Solvent-Casting Procedure

0.085-0.1g of polymer was weighed into a 5mL GPC vial with an inner diameter of X. A small stirbar was added to the sample vial and ~1mL of Chloroform was added to the sample via plastic transfer pipette. Care was taken to ensure all of the polymer sample was below the level of the solvent. The vial was capped and the polymer was dissolved using a stir plate and was placed on the vacuum pump for heating for short periods of time as necessary. Once the polymer was fully dissolved, the stir bar was removed from the solution and allowed as much solution to drip off as possible. The solution was viscous and bubbles were allowed to settle after stirring. The sample was then uncapped and placed in a vacuum holm at the edge so that it was not tilted. The cover was placed on the holm and clamped. A chem cap was placed in the holm cover but was not fully sealed. The holm was carefuly covered in foil and left to evaporate in a vacuum hood for ~7 days. After that time, the foil was removed from the holm to check in

the solvent had fully evaporated. If anything looked clear or shiny, there was still solvent in the sample. If the sample was not clear or shiny, it was removed from the holm and underwent a waft test to check for remaining solvent. If solvent still remained, the sample was placed back into the holm and left for another day before being checked again. If all solvent seemed to be gone, the vial was placed into the vacuum oven at room temperature and allowed the oven to completely evacuate (~2 hours). The sample was removed from the vial by either pulling out with tweezers or carefully breaking the glass by wrapping in paper towel, placing in a large weigh boat and lightly hitting with a large wrench. 3mL Teflon beakers had been previously used for sample preparation, but the bottom of the beakers was not flat which gave the samples unwanted bumps. Pictures below show the setup of the vacuum holm (a) and how the sample looks in the vial once dried (b).

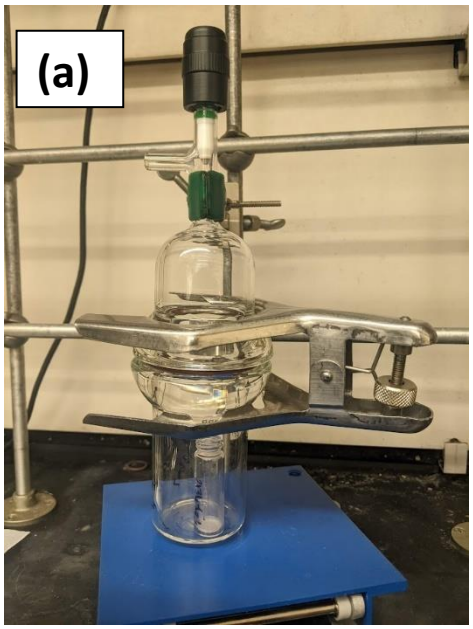

C.9 Toluene-D_8 NMR

1H-NMR with Toluene-d_8 as the solvent to show the absence of chloroform in the $SIOIS_{10}$ polymer after solvent casting out of chloroform. The chloroform peak in toluene-d_8 would be expected at 6.0ppm.

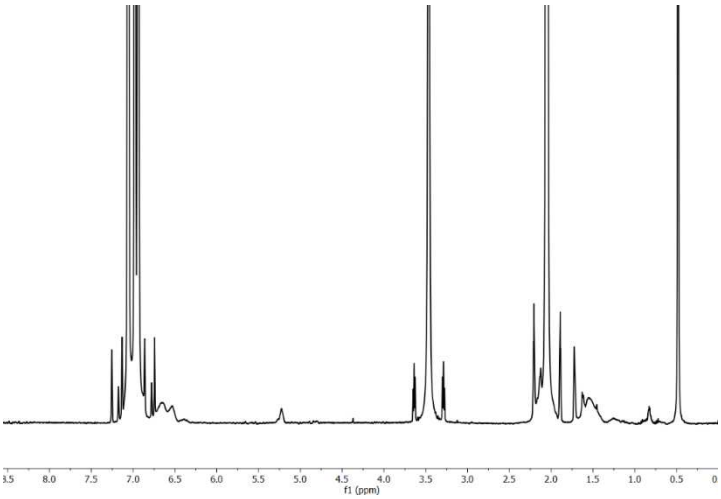

C.10 Qualitative comparison of solvent-casting methods for SIOIS10

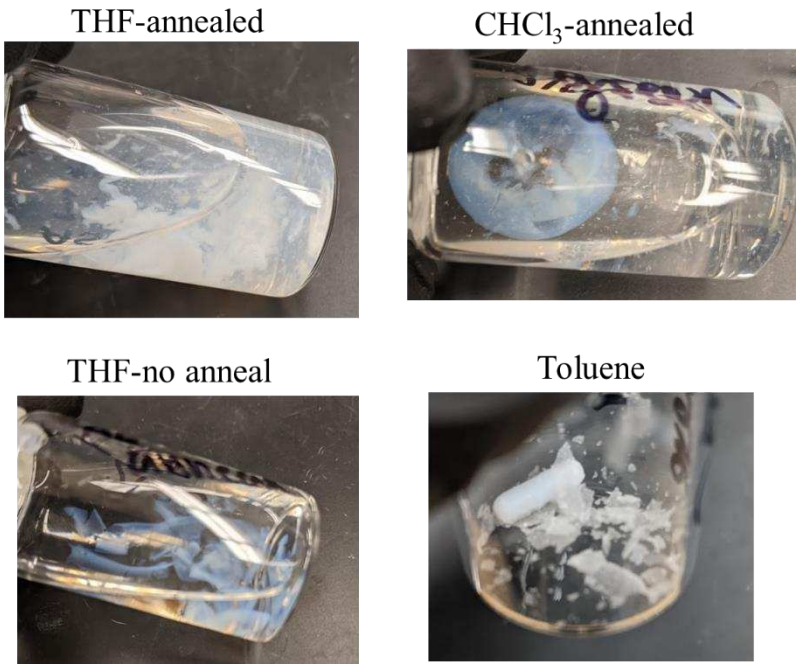

The $SIOIS_{10}$ hydrogel solvent-casting method was tested with THF, $CHCl_3$ and toluene. Additionally, samples cast with THF and $CHCl_3$ were annealed in a vacuum oven for 2-16 hours after casting according to previous success by Radlauer[1] and Qiao[2] with this method. However, other methods

of casting resulted in gels that fell apart after swelling (THF, THF annealed, $CHCl_3$ annealed) or never formed into a homeogeneous material that could be swollen (Toluene).

C.11 Table of polymers used in Chapter 4

Manuscript ID	Lab Notebook ID
S-OH	ASK-2035
SO	ASK-2050
SOS	ASK-2160
SI-OH	ASK-1186
SIO	ASK-1188
SIOIS	ASK-2070

References

1. Radlauer, M. R. *et al.* Morphological consequences of frustration in ABC triblock polymers. *Macromolecules* **50**, 446–458 (2017).
2. Qiao, Y. *et al.* Symmetric Poly(ethylene oxide- b -styrene- b -isoprene) Triblock Copolymers: Synthesis, Characterization, and Self-Assembly in Bulk and Thin Film. *Macromolecules* **47**, 6373–6381 (2014).

APPENDIX D: EXPLANATION OF MOLECULAR, MORPHOLOGICAL, AND MECHANICAL CHARACTERIZATION TECHNIQUES

D.1 Reaction Schemes for PS-PI, PS-PI-PEO, and PS-PI-PEO-PI-PS

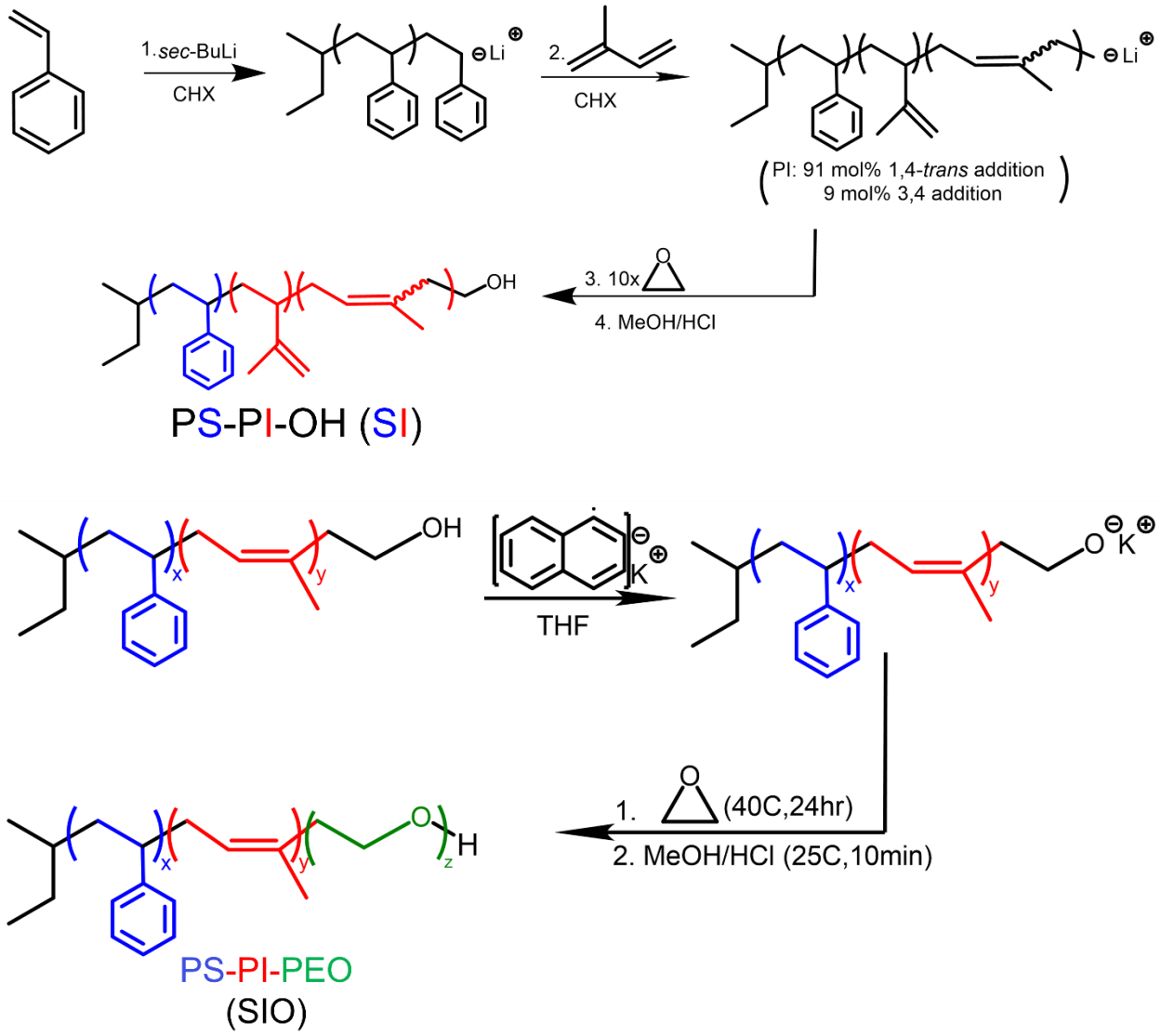

D.2 Representative NMR Analysis for PS-PB-PEO

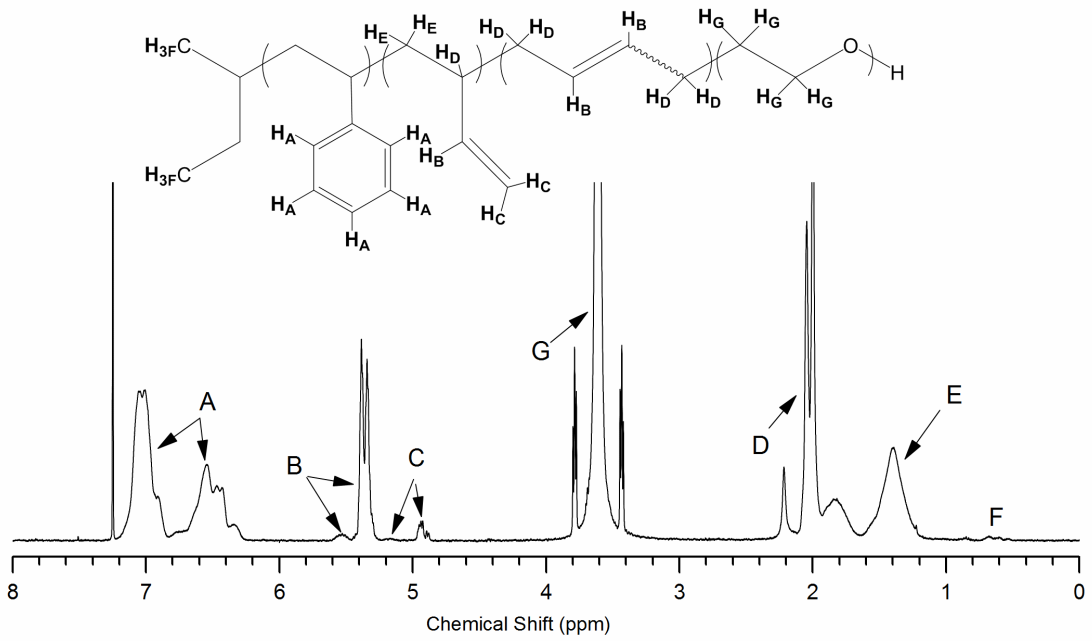

Our group uses end-group analysis from ^{1}H-NMR to calculate approximate molecular weights of each polymer synthesized. A representative ^{1}H-NMR for PS-PB-PEO is shown in FIGURE. The integration of each set of peaks is relative to the integration of the 6 methyl protons on the sec-butyllithium initiator fragment (normalize ∫F to 6).

Polystyrene M_n:

$$\frac{\int A}{5\ protons} = x\ repeat\ units\ PS \times \frac{104.15g}{mol}\ styrene = Mn\ PS$$

Polybutadiene M_n:

$$\frac{\int B}{2} - \frac{\int C}{4} = n\ repeat\ units\ \text{1,4-PB}$$

$$\frac{\int C}{2} = m\ repeat\ units\ \text{1,2-PB}$$

$$\%\ \text{1,2 PB} = \frac{m}{m+n}$$

$$\%\ \text{1,4 PB} = \frac{n}{m+n}$$

$$(m\ repeat\ units + n\ repeat\ units) \times \frac{54.09g}{mol} = Mn\ PB$$

Polyisoprene M_n:

For Polyisoprene, the NMR spectra is very similar (NMR found in Appendix A), but the slightly different chemical structure changes how many hydrogen atoms are calculated. These calculations for Mn Pb are similar to the calculations for Mn PI, but the number of repeat units is instead calculated by:

$$\frac{\int B}{1} = n\ repeat\ units\ \text{1,4-PI}$$

$$\frac{\int C}{2} = m\ repeat\ units\ \text{3,4-PB}$$

$$(m\ repeat\ units + n\ repeat\ units) \times \frac{68.12g}{mol} = Mn\ PB$$

Poly(ethylene oxide) M_n:

$$\frac{\int G}{4\ protons} = z\ repeat\ units\ PEO \times \frac{44g}{mol} ethylene\ oxide = Mn\ PEO$$

These M_n values can then be used to calculate the volume fraction of each block of the polymer chain in the following equation. The densities are taken for the polymers at 140°C from Fetters, et. al.[1]

Volume fraction calculation:

$$f_{PEO} = \frac{\frac{M_{n\,PEO}}{\rho_{PEO}}}{\frac{M_{n\,PB}}{\rho_{PB}} + \frac{M_{n\,PS}}{\rho_{PS}} + \frac{M_{n\,PEO}}{\rho_{PEO}}} \qquad \textbf{Equation D.1}$$

D.3 GPC

Gel permeation chromatography is a type of size exclusion chromatography which separates polymer chains by hydrodynamic volume. Our group uses this technique to confirm polymerization by comparing retention time of the polymer to its macroinitiator. Large macromolecules exit the column first. A unimodal peak and small distribution of retention times indicates a small polydispersity of molecular weights of the polymer chains as well as the complete conversion of all of the monomer used in the reaction.

A blend of ABC and ABCBA block copolymers will show a bimodal peak for the two different polymer lengths. The blend composition can be determined from the area of a Gaussian distribution fit to both peaks.

D.4 SAXS

Our group uses small angle X-ray scattering as the principal method to determine the bulk morphology of our block copolymers. Bulk copolymer morphologies consist of long-range ordering which can be characterized by nanometer-scale unit cell lattice constants and traditional crystallographic space groups. These space groups can be identified by a modification of X-ray diffraction. X-rays are elastically scattered off the crystal-like planes of an ordered block copolymer morphology. As seen by Bragg's Law Equation 3, these reflections are diffracted at very small angles because the distance between the crystal planes (*d*) in block copolymers is on the nanometer (vs. Angstrom) length scale.

$$n\lambda = 2d\sin\theta_B \qquad \textbf{Equation D.2}$$

The diffracted X-rays are detected in concentric rings around the transmitted rays. Because the scattered wave magnitude ($\frac{2\pi}{\lambda}$) is unchanged from the incident wave, the angle of scattering can then be represented as the change in momentum of the X-ray wave vector. This change is represented as q and is related to the scattering angle as seen in Equation 4.

$$q = \frac{4\pi}{\lambda}\sin(\theta_B) \qquad \textbf{Equation D.3}$$

The change in the wave vector can be correlated to the interplanar spacing (d_{hkl}) between a family of crystal planes (hkl) in the crystal lattice by combining equations 2 and 3 to produce Equation D.4.

$$q = \frac{2\pi}{d_{hkl}}$$ **Equation D.4**

Each block copolymer morphology corresponds to a known crystal structure. The crystal planes in a block copolymer morphology can be described by their Miller indices, their relationship to the interplanar spacing, and the lattice parameters of the crystal lattice unit cell (abc) as shown in Equation D.5.

$$\frac{1}{d_{hkl}^2} = \frac{h^2}{a^2} + \frac{k^2}{b^2} + \frac{l^2}{c^2}$$ **Equation D.5**

Comparison of different sets of crystal planes in a given crystal structure cancels out the unit cell dimensions for many cubic (a=b=c) morphologies such as the core-shell spheres on a body-centered cubic lattice which is the target for this hydrogel project. This characteristic of the cubic unit cell allows comparison of d spacings and q values in a polymer morphology without regard to the unit cell dimensions as seen in Equation D.6.

$$\frac{q_{h'k'l'}}{q_{hkl}} = \frac{d_{hkl}}{d_{h'k'l'}} = \frac{\sqrt{h'^2+k'^2+l'^2}}{\sqrt{h^2+k^2+l^2}}$$ **Equation D.6**

Crystal structures are assigned space groups which have their own symmetry elements. These symmetry elements determine what scattering angles (and, therefore, q values) are allowed for a given morphology. Crystallography tables give us an indication of which scattering peaks can occur for a certain structure and which are extinct.[23] Knowing which crystal planes scatterings are extinct then allows us to assign space groups (and ultimately morphologies) to the peaks that are seen in the scattering data. The allowed peaks are determined relative to the first (lowest q value) scattering peak observed referred to as the primary scattering peak (q*). For many morphologies, the primary scattering peak is for the 100

set of crystal planes represented by q_{100}, however, for the BCC morphology the primary scattering peak is the set of 110 peaks because the 100 peak is extinct. We can then use this q* as the q_{hkl} peak in equation 7 and calculate what q values other higher order peaks would be expected.

Rapid precipitation of polymer from solution often freezes the polymer in a non- or only partially phase separated phase. As temperature is increased, the intermolecular forces between the polymer chains become weaker, decreasing the polymer viscosity, and giving the chains enough kinetic energy to move past each other into the structure of lowest free energy. Because order or disorder of block copolymer systems is influenced by temperature ($\chi \propto \frac{1}{T}$), each sample is subjected to a temperature ramp to find the temperature range where the sample is ordered. The sample is then annealed at that temperature for at least an hour to allow time for the polymer chains to move into their segregated phases and to facilitate the development of longer range order.

D.5 Sphere size calculations

The principal scattering peak (q*) can be used to calculate the radii of the PS-PI spherical domain using the assumption that the spheres are situated in a body-centered cubic (bcc) lattice and that PI is formed an evenly spaced shell around the PS core. The first allowed reflection for the Im3m (bcc) space group correspondes to the 110 family of crystal planes. The d-spacing for this reflection is given as:

$$d_{110} = \frac{2\pi}{q_{110}} \qquad \textbf{Equation D.7}$$

where q_{110} is q*. This distance of d_{110} corresponds to one half of the crystal place face diagonal. Therefore, the unit cell lattice constant (a_{bcc}) is given by:

$$a_{bcc} = \sqrt{2} d_{110} \qquad \textbf{Equation D.8}$$

Next, we use the assumption that all of the PS-PI polymer is located within the spherical domains, the fact that the bcc lattice contains 2 complete spheres, and the known volume fraction of PS-PI as subtracted from the PEO volume fraction. The volume of the PS-PI sphere can be calculated by the equation:

$$V_{PS\text{-}PI} = \frac{(1-f_{PEO})\cdot a_{bcc}{}^3}{2} \qquad \textbf{Equation D.9}$$

By rearranging the equation for calculating the volume of a sphere, the radii of the PS-PI sphere in cm can be calculated using:

$$R_{PS\text{-}PI} = \left(\frac{3}{4\pi}\cdot\left(\frac{(1-f_{PEO})\cdot a_{bcc}{}^3}{2}\right)\right)^{1/3} \qquad \textbf{Equation D.10}$$

To then determine the radius of the separate PS and PI blocks, instead insert the volume fraction of PS for (1-f_{PEO}) into Equation D.10 to calculate R_{PS}. If we assume that the PI is forming a shell around the PS core that has an even thickness, we can calculate the radius of the PI using:

$$R_{PI} = R_{PS\text{-}PI} - R_{PI} \qquad \textbf{Equation D.11}$$

D.6 Rheology

Rheology is often used in conjunction with SAXS to verify polymer phase behavior. Morphologies often respond to shear strain differently at different temperatures. The storage or elastic moduli(G') and the loss or viscous moduli (G") for each sample are examined over a large temperature range to observe any changes in modulus, indicative of an order-disorder transition (ODT) in which phase separation is lost to a more energetically favorable mixing of the dissimilar blocks, or an order-order transition (OOT) in which one morphology transitions to another. The temperature of the transitions also informs us of the temperatures to be chosen for the SAXS temperature ramp to ensure a transition is not

missed. Frequency sweeps are also used to help determine differences in morphologies with similar SAXS spectra.

Before rheological testing, all samples are subjected to a strain sweep to ensure the frequency chosen for future tests falls into the linear viscoelastic region. Dynamic temperature ramps are completed at temperatures starting above the PEO melt temperature (~70°C) and ramp up to temperatures no higher than 250°C to ensure no polymer degradation occurs. Frequency sweeps are conducted over the frequency(ω) range of ω=100-0.1 at 150°C, 200°C, and 250°C. These separate temperatures can be used to construct the full range of frequencies using the principle of the time-temperature superposition. Typically, in the frequency sweeps, we would only observe plateauing of the G' modulus in samples which are forming spheres or hexagonally-packed cylinders which are aligned perpendicularly to the plates.[2] However, we observed plateauing in all samples with only a change in what temperature (and therefore frequency) the plateau occurred. Therefore, we could compare the when the plateau presented to point to the possiblity of a certain morphology. In the dynamic temperature ramp, we would expect to see the modulus change abruptly if the morphology changed or visualize a change in the ratio between G' and G".

D.7 Stress-strain curves for Compression and Tensile Testing

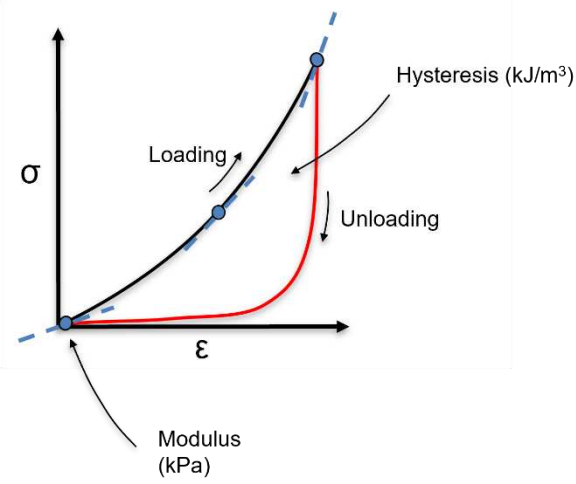

The strain(ε) is measured on the x-axis as the dependent variable denoting the change in length of the hydrogel during testing. The stress(σ) experienced by the hydrogel during that strain is expressed on the y-axis. The stress is the force exerted by the polymer over an certain area to resist being strained. The slope of the loading cycle in a stress-strain curve provides the modulus or stiffness of the material at a given strain. The area between the loading and unloading curves is the non-elastic response of the hydrogel, called the hysteresis, and is the measurement of energy dissipation (kJ/m^3) by the network.. Finally, the time between each cycle will also be tested to discover how long it takes for the strained B and C block chains to recover to their original conformational states. Mechanically, this corresponds to the wait time between mechanical loading cycles after which the subsequent mechanical loading curve traces the first. For an SOS hydrogel, the recovery time is less than a half a second. While these tests will give information about the B block, characterization (confirmation) of the hydrogel as "fatigue-resistant" will require the sample to be subject to tens of thousands of loading cycles without losing its mechanical properties.

Uniaxial tensile tests will also provide a measure of the ultimate strength of the material. Samples will be loaded at a given strain rate and strained until failure. The stress where this occurs quantifies the ultimate strength of the hydrogel and characterizes the material's ability to form a crack. Uniaxial tensile testing alone is not sufficient to characterize the fracture resistance of hydrogel materials. While a tensile test can provide maximum stress and strain at the material failure, these values can be highly influenced

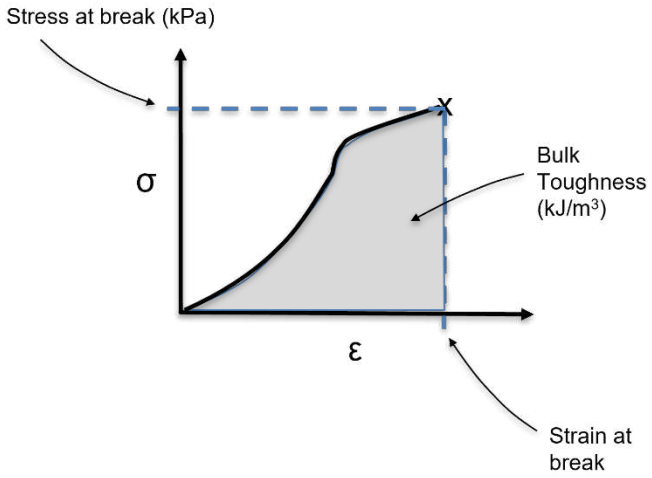

by small defects incurred as part of the material processing. The variability of defects between samples makes it difficult to distinguish the intrinsic fracture properties of the hydrogel from the processing defects using tensile testing. Instead, fracture testing will study crack growth.

References:

1. Fetters, L. J., Lohse, D. J., Richter, D., Witten, T. A. & Zirkel, A. Connection between Polymer Molecular Weight, Density, Chain Dimensions, and Melt Viscoelastic Properties. *Macromolecules* vol. 27 4639–4647 (1994)
2. Kossuth, M.B., Morse, D.C., Bates, F. S. Viscoelastic behavior of cubic phases in block copolymer melts. *J. Rheol. (N. Y. N. Y).* **43**, 167–194 (1999)